Atmospheric heterogeneities in ERS tandem SAR interferometry

Ramon Hanssen

DEOS Report
no 98.1

DEOS

Atmospheric heterogeneities in ERS tandem SAR interferometry

Atmospheric heterogeneities in ERS tandem SAR interferometry

Ramon Hanssen

Delft University Press / 1998

Published and distributed by:

Delft University Press
Mekelweg 4
2628 CD Delft
The Netherlands
Telephone: + 31 15 278 3254
Telefax: + 31 15 278 1661
E-mail: DUP@DUP.TUDelft.NL

ISBN 90-407-1774-5 / CIP

Printed in The Netherlands

Preface

As the first publications on repeat pass SAR interferometry showed phenomenal results for terrain mapping and deformation analysis, the first signs of the disturbing influence of the atmosphere were somewhat discouraging. The question, however, was if the observed effects were just coincidental artifacts, or whether they are apparent in many or maybe all interferometric observations. A closely related question is to identify the driving atmospheric mechanisms for the observed effects. Clearly, the analysis of a single interferogram is not sufficient to comment on these issues. For this reason, the underlying report tries to evaluate a large set of interferometric data, and assess the influence of atmospheric processes in it.

The realization of this report was only possible due to the contribution of different groups and individuals. I would like to thank Steve Coulson, Nick Walker and Andrea Abellini at the European Space Agency for the provision of the data and their support for this study. At the German Aerospace Research Establishment (DLR), Richard Bamler, Michael Eineder, Nico Adam, and Birgit Schättler contributed significantly to the work, and I would like to thank them for their kind hospitality and the use of their interferometric processing software. Servus. Gerhard Gesell at DLR provided some beautiful NOAA AVHRR color composites, which proved to be valuable reference material. The meteorological interpretation of the data was performed at, and in close collaboration with the Royal Netherlands Meteorological Institute (KNMI). Henk Benschop and Arnout Feijt were of great help in the collection and processing of the many meteorological data sources. I especially would like to thank Frans Debie and Sylvia Barlag, who spent many days looking at the interferograms, trying to figure out what could have caused those strange phase effects. Their professional meteorological knowledge formed a major contribution to this report. Herman Wessels is acknowledged for his assistance on the weather radar data. The final parts of this work were performed at Stanford University, in the group of Howard Zebker. His hospitality and our stimulating discussions are greatly appreciated. Falk Amelung gave some great comments on the draft. Finally, I would like to thank Roland Klees at Delft University of Technology for his support and critical comments.

The majority of the meteorological data was kindly provided by the Royal Netherlands Meteorological Institute in De Bilt, the Netherlands. The radiosonde profiles of Ukkel and Emden were made available by the European Center for Medium-Range Weather Forecasts (ECMWF), Meteorological Archival and Retrieval System (MARS). These data were acquired by Koninklijk Meteorologisch Instituut (KMI), Ukkel, Belgium, and Deutscher Wetter Dienst (DWD), Offenbach, Germany.

The amount of data analyzed for this study is enormous. A printed version of this report, including all the studied images of the interferometric processing (interferograms, coherence images, amplitude images), the spaceborne weather images from NOAA-AVHRR and METEOSAT, the plots of the radiosonde observations, and the plots of the different synoptic observations, would largely exceed the limits of a compact format. I have chosen to limit the amount of graphs for that reason, although the current version still includes many figures. This implicates that not all information referred to in the text can be verified by the report only. I wish to stimulate the interested reader to contact me for further information at `hanssen@geo.tudelft.nl`.

This report shows that atmospheric signal cannot be ignored while using ERS tandem interferometry for topographic mapping. However, the availability of more tandem interferograms for a given site enables (1) selection of pairs with most favourable weather conditions, and (2) the application of stacking techniques to suppress atmospheric influence on the final DEM.

Finally, I wish to express my confidence that the ERS tandem SAR database has an enormous potential for the study of atmospheric dynamics, water vapor distribution, and signal propagation. Using even coarse reference elevation models, interferometric SAR images can be used to study properties of the Earth's atmosphere at an unsurpassed precision and resolution level. I hope that this study can be a contribution to new developments in this field.

Ramon Hanssen,
Stanford, February 1998

Contents

List of Tables

List of Figures

Chapter 1

Introduction

1.1 Background

The ERS-1 and ERS-2 Tandem Mission, in which SAR pairs were acquired with an offset of one day, provided a unique dataset of SAR imagery which will be used in many years to come. The mission, in which ERS-2 followed 30 minutes behind ERS-1, in the same orbital plane, acquired about 110.000 SAR pairs over a period of nine months (August 1995 — April 1996) , covering nearly the total global land surface. Some 73% of the data has a perpendicular baseline between 50 and 300 m, 21% has a smaller baseline, and 6% a baseline between 300 and 600 m (Duchossois et al., 1996).

The baseline and interval characteristics ensure relatively good coherence values when an interferometric product is computed using the two SAR acquisitions, and provide good opportunities for deriving Digital Elevation Models (DEMs), or detecting deformations. Especially the possibility to make a nearly global DEM with one imaging system is unsurpassed at this time.

However, it has emerged that atmospheric variations, both in one scene and between the two SAR acquisitions, can lead to coherent phase artifacts in the interferograms, resulting in height offsets in the derived DEM.

The current study aims to provide a better insight in the driving mechanisms of the atmospheric influence on SAR interferometry, investigating the interferometric combination of 52 SAR images, each with its specific atmospheric characteristics.

1.2 Current state of affairs

Although the influence of the atmosphere on the propagation velocity of radio waves is already a long known fact, the first applications of repeat pass SAR interferometry did not reveal any signs of disturbance. This was mainly due to the fact that the images were acquired over areas were the phase effects were mainly caused by topography or deformation, which obscured the atmospheric signatures. Only after sound quantitative analyses with reference topography, or over areas without significant topography (Kooij et al., 1995), the residue phases were related with spatial variability in the atmosphere, influencing the propagation velocity of the radar signal, and hereby the observed interferometric phase.[1]

---

[1] A delay in the propagation velocity of the radar signal results in a phase shift in the interferogram. Since the effect of this phase shift on the derived DEM is dependent on the length of the perpendicular

Recent studies(Goldstein (1995); Massonnet and Feigl (1995); Tarayre and Massonnet (1996); Tarayre (1996); Hanssen and Feijt (1996); Hanssen and Usai (1997); Zebker et al. (1997); Dupont et al. (1997)) have shown that temporal and spatial variations of the refractive index of the propagation medium lead to phase variations in the derived interferograms.

Observations by Dupont et al. (1997) show phase variations with a low spatial frequency and an amplitude between 0.3 and 0.5 phase cycles in about 44 processed interferograms. In some interferograms, they observed localized phase variations with an amplitude of 1–3 phase cycles. Goldstein (1995) reports RMS phase variations of 0.1 phase cycles over the whole image, probably caused by turbulent mixing of water vapor and air, and maximum (peak-to-peak) variation of 1 phase cycle. Up to three phase cycles localized phase shift is observed by Tarayre and Massonnet (1996) corresponding with cumulus clouds, while Hanssen and Usai (1997) report wave effects with a wavelength of 1.5–2 km and an amplitude of 0.25 cycles, and localized phase shifts of up to 5 phase cycles. Zebker et al. (1997) analyzed L-band and C-band data from SIR-C, and found RMS values between 0.04 and 0.16 phase cycles for L-band, which would convert to 0.17 and 0.68 phase cycles RMS for C-band.

The refractive index $n(\vec{x}, t)$ is a function of time and space, and is being determined by mainly three components: pressure, temperature and water vapor. Therefore, in order to know $n(\vec{x}, t)$ we need to know the behavior of all three spatial components and exactly at the times of the SAR acquisitions. These requirements can not be met using current meteorological observations which lack in either temporal or in spatial resolution. However, even if image covering corrections for atmospheric delay seem unlikely at the time, it is necessary to achieve some better insights into the nature of the atmospheric mechanisms that cause the observed delays.

1.3 Goals of the study

This study analyzes the phase artifacts in a series of 26 interferograms and evaluates them using additional meteorological data. The main objectives are:

- to give a quantitative analysis of the observed atmospheric phase artifacts in terms of spatial scale and magnitude, and to make a classification of the effects,
- to compare these artifacts with appropriate meteorological information, and assess the atmospheric phenomena causing the artifacts,
- to investigate if, how, and which meteorological information can serve as a "warning flag" for the prediction of atmospherically induced artifacts in SAR interferograms,
- to give a first estimate of the number of artifact-free or artifact-low tandem pairs in the ESA Tandem archive (constrained by the chosen test areas), and
- to provide a brief summary of the contemporary theoretical understanding of phase artifacts induced by atmospheric heterogeneities.

---

baseline between the satellites, it is not useful to express the atmospheric errors in terms of meters height error. Therefore this report will denote the phase shift φ in angular terms (radians or cycles), or as an effective one-way delay $\Delta\rho$ in meters, using $\Delta\rho = \frac{\lambda}{4\pi}\varphi$ where λ is the wavelength of the SAR (0.0566 m).

1.4 Methodology

Since the interferometric phase over coherent areas is mainly influenced by topography, deformation between the SAR acquisitions, and atmospheric delay, it is important to use SAR images over an area where either an accurate digital elevation model is available, or where there simply is minimal topography. The selected test sites in the Netherlands fulfill both requirements. Furthermore, a dense network of meteorological observation stations is available, providing a vast amount of significant meteorological data.

A set of *26 ERS SAR tandem pairs*, covering relatively flat areas centered around the Dutch provinces Groningen and Flevoland, is processed to phase unwrapped and geocoded interferograms.[2] *Meteorological data*, consisting of surface (synoptic) measurements, weather radar, radiosondes, and satellite imagery are used for the analysis of these interferograms. For each interferogram the type, extent and magnitude of local phase biases are evaluated. The hypothesis that this bias is of atmospheric origin is tested using meteorological data.

The project can be separated into two parts. The first part consists of the interferometric processing. The set of SLC (Single Look Complex) SAR data is processed to form geocoded, phase-unwrapped interferograms. The second part comprises the meteorological evaluation. Based on the acquisition dates and times, a set of meteorological data is composed, which enables the comparison and analysis with the observed phase artifacts in the interferograms. Finally, conclusions on the driving atmospheric mechanisms are presented.

1.5 Outline of this report

The report can be separated in a review part (chapter 2), a descriptive part (chapter 3 and 4), and a data analysis part (chapter 5). Based on existing literature, a brief résumé of the current status of the theoretical understanding of phase artifacts induced by the atmosphere is given in chapter 2. It describes the basic principles of SAR interferometry and radio wave propagation, and discusses some relevant atmospheric parameters.

Chapter 3 covers the interferometric database used in this specific study. It is described which interferometric processing steps are applied, and the necessary post-processing to obtain interpretable phase information. For this interpretation, a number of meteorological data sources are used. A description of these data, the instrumentation, and the obtained atmospheric parameters is the main topic in chapter 4.

The main analysis of the set of interferograms is performed in chapter 5. For every interferogram, the observed effects are discussed in both a descriptive and a quantitative way. Following this description, key points of the interpretation are described. It is tried to explain all observed effects from a meteorological point of view, and to define the driving mechanisms for the phase observations. Finally, some short conclusions on the discussed interferogram are drawn. The chapter concludes with a discussion, in which the results of the analyses are merged and evaluated statistically.

Finally, in chapter 6 the main conclusions and recommendations of the study are given on the type and magnitude of the phase anomalies and the feasibility of using meteorological

---

[2] Since one specific tandem acquisition was made during an extensive meteorological experiment (CLARA–Clouds and Radiation) in the western part of the Netherlands, which acquired a wealth of meteorological data, these data have also been evaluated.

data for estimating atmospheric disturbance.

1.5.1 How to read this report

While preparing this report, I found out that this work is perhaps not only interesting for scientists in the field of SAR interferometry. Apart from being a mere nuisance for applications of SAR interferometry in the generation of digital elevation models or differential deformation maps, the atmospheric signal observed in the SAR interferograms provides insights in the spatial distribution of water vapor, with an unsurpassed resolution level starting from 20×20 meters and a relative accuracy level of 1.8 mm signal delay. Therefore, this work might be of interest to meteorologists or, e.g., scientists working in the field of tropospheric modelling for high accuracy GPS applications.

The main purpose of this work is, however, the assessment of the atmospheric influence for ERS tandem SAR interferometry. Therefore, the used unit in the quantitative analyses is mostly radian or phase cycle. This can be easily transformed to millimeters water vapor delay in slant range using

$$1 \text{ rad} \approx 4.6 \text{ mm}, \quad \text{and} \quad 1 \text{ cycle} \approx 28 \text{ mm},$$

in which an accuracy level of 0.4 rad, or 1.8 mm, can be easily obtained. Mapping the slant range delay to the zenith direction, the values are 4.8 mm and 30 mm for radian and phase cycle respectively.

In the discussion of the interferograms, it was necessary to refer to a number of cities, regions, and meteorological stations in the Netherlands. To guide the reader unfamiliar with Dutch topography, schematic maps and short descriptions of the different regions are included at the beginning of the sections in chapter 5. Although the use of site specific names is avoided as much as possible, the reader is referred to those maps for assistance.

Chapter 2

Theoretical review

This chapter gives an introduction to some relevant topics considering SAR interferometry and the way it may be influenced by the atmosphere. The chapter starts with a brief review of the important equations governing the SAR interferometric configuration, and the way a localized atmospheric anomaly will affect it. The second section covers some aspects of radio wave propagation. It describes the importance of the refractive index and how a radio range error originates in the neutral atmosphere and in the ionosphere. Section 2.3 discusses some relevant physical characteristics of the troposphere and ionosphere, and lists some often used humidity measures. Finally, section 2.4 focuses on the specific consequences of atmospheric signal propagation for SAR interferometry. In this context, some important atmospheric phenomena are discussed in some more detail.

key words: SAR interferometry, atmosphere, radio range error, refractive index

2.1 SAR interferometry and atmospheric phase delay

Repeat pass SAR interferometry has been demonstrated by Li and Goldstein (1990) using Seasat SAR images. First applications for the generation of elevation models using ERS were performed by Zebker et al. (1994), whereas first accurate surface deformation maps were shown by Massonnet et al. (1993). Speculations on phase variations from atmospheric origin were published by Massonnet and Feigl (1995) and Massonnet et al. (1995).

The following paragraphs review the basic equations of repeat pass SAR interferometry, and describe how an atmospheric inhomogeneity will influence the observed interferometric phase.

2.1.1 Repeat pass SAR interferometry

The standard interferometric repeat pass configuration is shown in figure 2.1. At the positions 1 and 2 a phase measurement is made for a specific resolution cell. If the baseline B between the two antennas is divided into a perpendicular component $B^{\perp}$ and a parallel component $B^{\|}$, these phase measurements can be written as

$$\psi_1 = \frac{4\pi}{\lambda} R_1, \quad \text{and} \tag{2.1}$$

$$\psi_2 = \frac{4\pi}{\lambda} (R_1 + B^{\|}), \tag{2.2}$$

where R_1 is the slant range, measured by the time delay of that resolution cell, and λ is the wavelength of the signal. The far field approximation is used, implicating that the look angle θ is considered equal for sensor 1 and 2. No surface deformation terms are included in these equations.

The interferometric phase φ of the resolution cell is found by multiplying the complex value of image 1 with the conjugated complex value of image 2, which yields a phase difference

$$\varphi = \psi_1 - \psi_2 = -\frac{4\pi}{\lambda} B^{||}. \tag{2.3}$$

A value for $B^{||}$ can be found using the geometric relationship

$$B^{||} = B \sin(\theta - \alpha), \tag{2.4}$$

where α is the orientation of the baseline with length B.

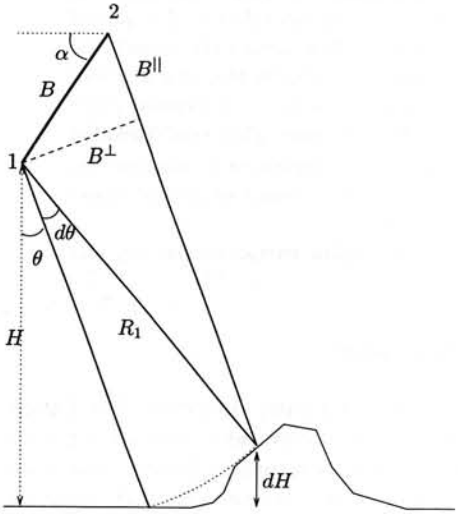

Figure 2.1 *Interferometric configuration*

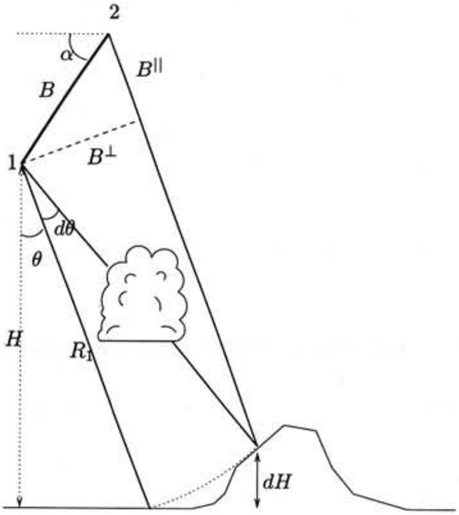

Figure 2.2 *A localized inhomogeneity*

The relationship with the topographic height is found using the height H of sensor 1 above a reference surface, i.e. the WGS84 ellipsoid. This sensor height is given by $H = R_1 \cos\theta$. The slant range R_1, however, cannot be used to uniquely determine the position of the resolution cell on Earth, see figure 2.1. Therefore, the change in look angle $d\theta$ connected with the topographic height dH needs to be determined from the interferometric measurement, using $dH = -R_1 \sin\theta d\theta$.

A change in look angle $d\theta$ yields a slight difference in the parallel baseline $dB^{||}$,

$$dB^{||} = B \cos(\theta - \alpha) d\theta, \tag{2.5}$$

which is consequently related to the observed change $d\varphi$ in the interferometric phase:

$$d\varphi = -\frac{4\pi}{\lambda} dB^{||}. \tag{2.6}$$

Using these equations, the relation between $d\varphi$, which is the measured phase difference between the reference phase and the observed phase of the resolution cell, and the topographic height dH, which is the height difference between a reference ellipsoidal height and the height of the resolution cell, can be written as

$$dH = \frac{\lambda}{4\pi}\frac{R_1 \sin\theta}{B\cos(\theta-\alpha)}d\varphi = \frac{\lambda}{4\pi}\frac{R_1 \sin\theta}{B^{\perp}}d\varphi. \tag{2.7}$$

The topographic height is therefore inversely proportional to the perpendicular baseline $B^{\perp}$. Note that when the parallel baseline is positive, as sketched in figure 2.1, a positive change in interferometric phase yields a positive topographic height (i.e. a hill instead of a valley). If the parallel baseline is negative, equation (2.7) will change in

$$dH = -\frac{\lambda}{4\pi}\frac{R_1 \sin\theta}{B^{\perp}}d\varphi, \tag{2.8}$$

and a positive phase results in a negative height.

2.1.2 The influence of an atmospheric inhomogeneity

The slant ranges in equation (2.1) and (2.2) are determined using the travel time τ of the signal and the velocity of light c, with

$$R = \tau c/2. \tag{2.9}$$

However, since the true velocity v of the radio waves in the atmosphere is slower than the velocity of light in vacuum c, an additional atmospheric delay term needs to be added, which can be translated to an (imaginary) excess distance ΔR_e:

$$\psi_1 = \frac{4\pi}{\lambda}(R_1 + \Delta R_{e,1}), \quad \text{and} \tag{2.10}$$

$$\psi_2 = \frac{4\pi}{\lambda}(R_1 + B^{\|} + \Delta R_{e,2}). \tag{2.11}$$

Typical values for the excess distance are 2.5—3 meters. In the interferometric phase, cf. equation (2.3), this results in

$$\varphi = \frac{4\pi}{\lambda}(-B^{\|} + \Delta R_{e,1} - \Delta R_{e,2}). \tag{2.12}$$

Assuming that the atmospheric delay is homogeneous for the whole SAR scene, the consequence of these excess distances is limited to a biased interferometric phase. As noted before, the main interferometric observable is a phase *change* ($d\varphi$), and therefore the atmospherically induced bias is eliminated.

However, the assumption of a homogeneous atmosphere is not valid for most of the areas in the world, were mixing processes cause localized temperature and humidity gradients, hereby inducing local differences in signal delay.

Figure 2.2 shows the same configuration as figure 2.1 with a localized atmospheric inhomogeneity at the time of the first SAR acquisition. It is assumed that the inhomogeneity is characterized by an increase in refractive index. This results in a slower propagation velocity, or an increase in the excess distance $\Delta R_{e,1}$, with respect to the reference phase. Using equation (2.7) and (2.12), the interferometric phase can now be described by

$$d\varphi = \frac{4\pi}{\lambda}\left(\frac{B^{\perp}}{R_1 \sin\theta}dH + d\Delta R_{e,1} - d\Delta R_{e,2}\right). \tag{2.13}$$

In the example of figure 2.2, $d\Delta R_{e,2} = 0$, and therefore a localized signal delay at the first SAR acquisition will result in a positive phase change in the interferogram. A similar effect during the second SAR acquisition would cause a negative phase change. In contrary to the phase sign resulting from topographic height, atmospheric phase signs are *independent* of the parallel baseline[1].

Equation (2.13) clearly shows that the influence of localized signal delays on the interferometric phase is not related to the perpendicular baseline, in contrary to topographic height. Note that for a single-pass interferometer, the atmospherically induced delay (and the spatial delay variations) is equal for both receiving antennas, and is eliminated when differencing the two phase images.

In the approach used in this study, the value for dH in equation (2.13) is obtained from an a priori reference elevation model. Therefore, the first term in the brackets is known, and the topographic phase can be subtracted from the total phase, leaving

$$d\varphi = \frac{4\pi}{\lambda}\left(d\Delta R_{e,1} - d\Delta R_{e,2}\right), \tag{2.14}$$

which is referred to as the *differential interferogram* in the sequel. This simple equation describes the response of the interferometric phase φ on a signal delay $\Delta R_{e,i}$, for image i. It shows that, due to the relative character of the observations, it is only possible to measure spatial *variations* in signal delay. This is the reason why this study focuses on atmospheric *heterogeneities*, and not on the total atmospheric delay.[2]

From equation (2.13) it directly follows how atmospheric heterogeneities translate into DEM errors, if the two right terms of the equation would not be included in the model. An error in the DEM height ε_{dH} is related to a localized atmospheric delay $d\Delta R_e$ by

$$\begin{aligned} \varepsilon_{dH} &= \pm\frac{R_1 \sin\theta}{B^{\perp}} d\Delta R_e && (2.15)\\ &\approx \pm\frac{330000}{B^{\perp}} d\Delta R_e && (2.16) \end{aligned}$$

where the sign is positive for a localized delay in the first acquisition, and negative for a localized delay during the second acquisition. Note that an increase in $B^{\perp}$ linearly suppresses the DEM errors caused by the atmospheric delays.

2.2 Radio wave propagation

The influence of the atmosphere on electromagnetic waves in the *microwave* band (1 GHz–30 GHz) can manifest itself in two forms (Hall et al., 1996), if we limit ourselves to Earth–

---

[1] Note that for negative parallel baselines, the absolute phase image might need to be reversed. This causes also the atmospheric signs to be reversed, which should be accounted for in the interpretation.

[2] It has to be noted that for areas with significant topography the vertical changes in atmospheric variability cannot be neglected anymore, as reported by, e.g., Delacourt et al. (1997), since changes in the vertical profile between the two acquisition dates result in a differential phase in the interferogram. These topographically induced atmospheric influences can, however, be neglected in the current study.

space configurations. First, there are the *clear air* effects of atmospheric gases and their associated refractive index changes, like signal delay, ray bending, absorption, reflection, and tropospheric scattering. Secondly, there are the effects of *liquid and solid particles* (clouds, precipitation, aerosols), like attenuation, cross polarization and scattering.

For the application of ERS tandem SAR interferometry, we will discuss signal delay in both forms: the clear air effects and the particle effects. In the following paragraphs, the clear air effects are considered. Particle effects are treated in the discussion on clouds and rain, later in this chapter.

2.2.1 The refractive index

For radio signals propagating through the atmosphere, the velocity and ray curvature is affected by variations in the refractive index n along the path. The refractive index is only slightly higher than the vacuum value ($n = 1$), and therefore often the scaled-up *refractivity*, N, is used, where $N = (n-1)10^6$. In the following paragraphs, the refractive index or the refractivity is expressed for the neutral atmosphere and the ionosphere. Since the neutral atmosphere cannot be modeled as a clear gas only for the purposes of this study, also the influence of clouds and precipitation is investigated

2.2.1.1 Neutral atmosphere

For radio frequencies up to 30 GHz in the troposphere, the refractivity N can be written as (Smith and Weintraub, 1953)

$$N = k_1 \frac{P_d}{T} + k_2 \frac{e}{T} + k_3 \frac{e}{T^2}, \tag{2.17}$$

where P_d is the partial pressure of dry air in mbar, e is the partial pressure of water vapor in mbar, and T is the absolute temperature in degrees Kelvin. The constants k_1, k_2, and k_3 have been first determined by Smith and Weintraub (1953). [$k_1 = 77.6$ K mb^{-1}, $k_2 = 71.6$ K mb^{-1}, and $k_3 = 3.75 \cdot 10^5$ K^2 mb^{-1}]. These constants are considered to be accurate to 0.5 % of N. The first term at the right hand side of equation (2.17) is often labeled as the "dry" delay, the two other terms as the "wet" delay. Assuming that the total atmospheric pressure $P = P_d + e$, and using the ideal gas law, an equivalent expression is obtained:

$$N = k_1 \frac{P}{T} + k_2' \frac{e}{T} + k_3 \frac{e}{T^2}. \tag{2.18}$$

In this expression, the first term at the right hand side is labeled the "hydrostatic" delay. The second term k_2' is defined as:

$$k_2' = k_2 - \frac{R_d}{R_v} k_1, \tag{2.19}$$

with $R_d = 287.053$ J K^{-1} kg^{-1}, and $R_v = 461$ J K^{-1} kg^{-1}. At saturation, the partial pressure of water vapor is typically less than 2.5% of the total atmospheric pressure, as given by the Clausius-Clapeyron equation, see section 2.3.3. For a temperature $T = 20°$C this equation yields the saturated partial water vapor pressure $e_s = 23.7$ mbar. A standard total atmospheric pressure $P = 1013$ mbar would now give the following components for equation (2.18): $N = 268.3 - 0.5 + 103.5 = 371$, or $(72\% - 0.1\% + 28\%)$. Using the total atmospheric pressure in the first term at the right hand side we can estimate the one-way range delay in zenith direction using a simple barometric measurement, as described in section 2.2.2.

2.2.1.2 Ionosphere

The refractive index of the ionosphere can in first order be expressed by (Jakowski et al., 1992):

$$n = 1 - \frac{40.28}{f^2} \cdot EC, \tag{2.20}$$

where EC is the content of free electrons per cubic meter, and f is the frequency of the signal. Note the dispersive (frequency dependent) character of the ionospheric refractive index, as opposed to the non-dispersive neutral atmosphere.

2.2.2 The radio range error

The difference between the measured radio range R_e and the true slant range R_0 is called the radio range error ΔR_e, with

$$R_e = R_0 + \Delta R_e. \tag{2.21}$$

This error consists of a "bending" error and a propagation delay (Bean and Dutton, 1986). The *bending error* is the difference between the curved length of the ray path called the geometric range R_g and the true slant range R_0, denoted by ΔR_g. The *propagation delay* is the discrepancy between the velocity of propagation in vacuum and the lowered velocity of propagation in the refractive medium.

The geometric range R_g under a zenith angle θ, which is a function of height h, is given by:

$$R_g = \int_0^H \frac{1}{\cos\theta} dh, \tag{2.22}$$

and the measured radio range (including the delay *and* the bending effects) is given by

$$R_e = \int_0^H \frac{n}{\cos\theta} dh. \tag{2.23}$$

The total radio range error in (2.21) is therefore given by

$$\Delta R_e = \int_0^H \frac{n}{\cos\theta} dh - R_0, \tag{2.24}$$

or using the refractivity $N = (n-1) \times 10^6$

$$\begin{aligned} \Delta R_e &= 10^{-6} \int_0^H \frac{N}{\cos\theta} dh + (\int_0^H \frac{1}{\cos\theta} dh - R_0), \quad \text{or} \\ \Delta R_e &= \Delta R_N + \Delta R_g, \end{aligned} \tag{2.25}$$

where ΔR_N is the refractivity error (the propagation delay) and ΔR_g is the ray bending effect. Bean and Dutton (1986) have shown that even for extreme refractivities, the ratio

$\Delta R_g/\Delta R_e$ approaches zero for zenith angles less than 87°. Therefore, for the ERS look angle around 23°, the radio range error can be considered as a function of only the first integral in (2.25):

$$\Delta R_e = 10^{-6} \int_0^H \frac{N}{\cos\theta} dh. \tag{2.26}$$

The omission of factor 10^{-6} and the integral over dh gives

$$\Delta R_e \quad [\text{in mm}] = \frac{N}{\cos\theta} \quad [\text{per km}], \tag{2.27}$$

where the factor N can be used as an approximation for the one-way path delay in mm, per km of signal path.

2.2.2.1 Neutral atmosphere

Using equation (2.18) in (2.26), we find

$$\Delta R_e = \frac{10^{-6}}{\cos\theta} \left(k_1 R_d \int_0^H \rho dh + \int_0^H (k_2' \frac{e}{T} + k_3 \frac{e}{T^2}) dh \right). \tag{2.28}$$

The first term in the brackets is only dependent of the total density, and can be integrated assuming hydrostatic equilibrium. As the total surface pressure P_s can be written as

$$P_s = g_m \int_0^\infty \rho(z) dz, \tag{2.29}$$

where g_m is the approximate local gravity at the centroid of the atmospheric column (Saastamoinen, 1972), given by

$$g_m = 9.784 \cdot (1 - 0.0026 \cos 2\varphi - 0.00028 z_0) \quad [\text{m/s}^2], \tag{2.30}$$

dependent of surface height z_0 and latitude φ. Using this quantity, we can write the first term of (2.28) as the zenith ($\theta = 0$) hydrostatic delay (ZHD):

$$\Delta R_{e,\text{ZHD}} = k_1 \cdot 10^{-6} \cdot \frac{R_d}{g_m} P_s. \tag{2.31}$$

Using these parameters, and a surface pressure P_s measured with an accuracy of 0.4 mbar or better, this delay can be predicted with an accuracy of 1 mm or better (Bevis et al., 1996). For the test sites used in this study, $\Delta R_{e,\text{ZHD}} = 2.275 \cdot 10^{-3} P_s$.

The second term, the *wet path delay*, is dependent on the water vapor density and the temperature along the ray path. Without the term for the look angle, the *zenith wet delay* (ZWD) is

$$\Delta R_{e,\text{ZWD}} = 10^{-6} \int_0^H (k_2' \frac{e}{T} + k_3 \frac{e}{T^2}) d\hbar. \tag{2.32}$$

This expression can directly be used for computing $\Delta R_{e,\text{ZWD}}$ from radiosonde observations (Bevis et al., 1996). Related useful parameters in this context are the vertically integrated water vapor and the precipitable water (PW), which is defined as the height of an equivalent column of liquid water. Davis et al. (1985) introduced a *mean temperature*, defined as

$$\int_0^H \frac{e}{T} dh = T_m \int_0^H \frac{e}{T^2} dh, \tag{2.33}$$

which is approximated by Bevis et al. (1994) using the surface temperature T_s (Kelvin):

$$T_m = 0.72 T_s + 70.2. \tag{2.34}$$

Using the ideal gas law, the mean temperature T_m and equation (2.32), we find the zenith wet delay

$$\Delta R_{e,\mathrm{ZWD}} = 10^{-6} R_v (k_2' + k_3/T_m) \int_0^H \rho_v dh, \tag{2.35}$$

where R_v is the specific gas constant for water vapor (461 J K^{-1} kg^{-1}) and ρ_v the density of water vapor. The integrated water vapor is the integral at the right term of this equation. The precipitable water can be found by dividing the integrated water vapor by the density of (liquid) water ρ_w. This establishes the relation between the zenith wet delay and the precipitable water:

$$\begin{aligned} \Delta R_{e,\mathrm{ZWD}} &= 10^{-6} \rho_w R_v (k_2' + k_3/T_m) \cdot \frac{1}{\rho_w} \int_0^H \rho_v dh & (2.36) \\ &= \Pi^{-1} \mathrm{PW}, & (2.37) \end{aligned}$$

where Π is a dimensionless quantity (Askne and Nordius, 1987). Following Bevis et al. (1992), $\Pi \approx 0.15$, but varies up to 10% due to changes in T_m, dependent on the location and the weather.[3] Using equation (2.36), either estimates of PW from numerical weather models, or measurements from water vapor radiometers can be used to determine the zenith wet delay.

Note that the water vapor density along the ray path is difficult to measure by traditional meteorological surface measurements, since there is little correlation between the water vapor density at the ground with that at higher altitudes, or at other positions horizontally (Reber and Swope, 1972).

2.2.2.2 Ionosphere

Inserting (2.20) in (2.26), and assuming no ray bending effects we find

$$\Delta R_e = \int_0^H \frac{(n-1)}{\cos\theta} dh = -40.28 \int_0^H \frac{EC}{f^2 \cos\theta} dh. \tag{2.38}$$

Note that an increase in the number of free electrons per m^2 causes an advance of the signal: the signal travels faster than c. The integration of the *free electron density* EC along the ray path represents the *total electron content* TEC, per m^2. Therefore we can express (2.38) as

$$\Delta R_e = \frac{-40.28}{f^2 \cos\theta} TEC. \tag{2.39}$$

---

[3] Use the k_1, k_2, and k_3 coefficients in Pa

The range error for the ERS SAR frequency can now be approximated by

$$\Delta R_e = -0.015 \cdot 10^{-16} \cdot TEC, \tag{2.40}$$

with TEC values vary between 0 at night to $20 \cdot 10^{16}$ m^{-2} at the minimum of the solar cycle to $100 \cdot 10^{16}$ m^{-2} at the maximum of the solar cycle, which corresponds to maximum delays of -30 cm and -1.5 m respectively.

2.3 Atmospheric structure

The main characteristics of the neutral atmosphere and the ionosphere are described in paragraphs 2.3.1 and 2.3.4 respectively. For the neutral atmosphere, a *standard atmosphere* describes the function of temperature and pressure with height. This model can be used to estimate the total radio range delay, and is described in paragraph 2.3.2. Since the main source of spatial variability of the refractive index is formed by heterogeneities in the moisture content, standard humidity measures need to be interpreted and converted to the partial water vapor pressure to solve equation 2.32 in section 2.2.2. An overview of different humidity measures and their conversions is given in paragraph 2.3.3.

2.3.1 The neutral atmosphere

The troposphere is the main region of the atmosphere, were masses of different kinds of air are very well mixed together, while the temperature decreases with altitude. Air is heated from the Earth surface, and the motions of the troposphere mix the heat energy. When parcels of air that are saturated with water vapor are moved into colder regions by the mixing, clouds are formed.

In the stratosphere, masses of air are still relatively well mixed, but the temperature increases with altitude. The gases are heated from below as well as from above. An ozone layer at approximately 50 km height causes the warming of the stratosphere with increasing height.

2.3.2 Standard atmosphere

The "1976 U.S. Standard Atmosphere" was developed as an engineering reference for the atmospheric state as a function of height (Stull, 1995). It describes the behavior of temperature and pressure in an idealized, dry, steady state atmosphere. The temperature equations are

$$\begin{array}{rcllrl} T &=& 288 + \alpha H & \text{for} & H < 11 & \text{km} \\ T &=& 216.5 & \text{for} & 11 \leq H \leq 20 & \text{km} \\ T &=& 216.5 + \beta(H-20) & \text{for} & 20 < H < 32 & \text{km} \end{array} \tag{2.41}$$

with $\alpha = -6.5$ (K/km), $\beta = 1$ (K/km), and H the geopotential height. The geopotential height is defined to compensate for the decrease in gravitational attraction with the geometric height z, as

$$H = R_e z / (R_e + z) \tag{2.42}$$

where $R_e = 6356.766$ km is the mean Earth radius. Note that (2.41) uses the geopotential height in km.

Similar equations can be given for the standard atmosphere pressure P (in mbar):

$$\begin{array}{rcllr} P & = & 1013.25(288.15/T)^{-5.255877} & \text{for} \quad H < 11 \text{ km} & \\ P & = & 226.32\exp(-0.1568(H-11)) & \text{for} \quad 11 \leq H \leq 20 \text{ km} & (2.43) \\ P & = & 54.749(216.65/T)^{-4.16319} & \text{for} \quad 20 < H < 32 \text{ km} & \end{array}$$

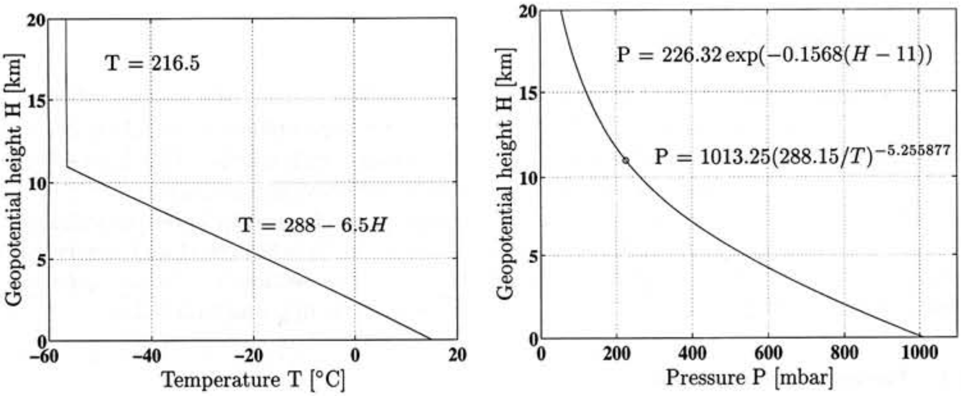

Figure 2.3 *The profiles of temperature and pressure in the 1976 U.S. Standard Atmosphere*

2.3.3 Humidity measures

A relationship which plays an important role in the definition of humidity is the *equation of state* for an ideal gas which has a meteorological form:

$$P_d = \rho_d R_d T, \tag{2.44}$$

where R_d is the *specific gas constant*, which is 287.053 J K^{-1} kg^{-1} for dry air, P_d is the pressure of the dry gas, ρ_d its density, and T the temperature in °K. Equation (2.44) is also known as the ideal gas law.

This equation of state can be used to calculate the *partial water vapor pressure* e as a function of the *absolute humidity* or vapor density ρ_v and the absolute temperature T, since vapor behaves as an ideal gas in terrestrial conditions:

$$e = \rho_v R_v T, \tag{2.45}$$

where R_v is the specific gas constant for water vapor, which is 461 J K^{-1} kg^{-1}. The ratio of the gas constants R_d/R_v is therefore 0.622, often represented by ϵ.

The absolute humidity ρ_v is an objective measure for the amount of water vapor (in grams of equivalent liquid water) per cubic meter air. There is an upper limit for the amount of water vapor that a parcel of air can absorb. An additional input of water vapor would lead to condensation into clouds (ice crystals or water droplets), fog, dew, etc. This maximal value, the saturation point or dew point, is dependent of the temperature. Warm air can absorb more water vapor than cold air: it has a higher saturation point, cf. table 2.1. The saturation partial water vapor pressure e_s at temperature T is described by the

Air temp [°C]	Absolute humidity [grams/m^3]
0	4.8
10	9.4
20	17.3
30	30.4

Table 2.1 *The relation between the air temperature and amount of liquid water a cubic meter air can absorb.*

Clausius-Clapeyron equation (Stull, 1995):

$$e_s = e_0 \exp\left(\frac{L}{R_v}(\frac{1}{T_o} - \frac{1}{T})\right), \tag{2.46}$$

where $e_0 = 6.11$ mbar, $T_0 = 273$ °K, and L is the latent heat. Over a flat water surface, $L = 2.5 \cdot 10^6$ J kg^{-1}, which is the latent heat of vaporization. In this case, cloud droplets are being formed. Over a flat ice surface, $L = 2.83 \cdot 10^6$ J kg^{-1}, which is the latent heat of deposition, when ice crystals are being formed. For a temperature of 20 °C, $e_s = 23.7$ mbar, roughly 2.3 percent of the average total atmospheric pressure of 1013 mbar. Note that e_s does not depend on the pressure.

The *relative humidity* RH is the ratio of the amount of water vapor in the air compared to the saturation amount of water vapor at that temperature: $RH = (e/e_s) \cdot 100\%$ For all practical purposes the relative humidity in water clouds is 100 percent. The partial pressure of water vapor e can be computed from the relative humidity RH and the temperature T, using equation (2.46):

$$e = \frac{RH}{100} e_s(T). \tag{2.47}$$

The humidity *mixing ratio* r is the ratio between the mass of water vapor and the mass of dry air:

$$r = \frac{m_v}{m_d} = \frac{\epsilon \cdot e}{P_d} \tag{2.48}$$

The ratio between the mass of water vapor and the *total* pressure is called the *specific humidity*:

$$q = \frac{m_v}{m_d + m_v} = \frac{\epsilon \cdot e}{P_d + e} \tag{2.49}$$

As an example, for typical low tropospheric conditions, $q = 10$ g kg^{-1}, and $P_d + e = 1000$ mbar, so the partial pressure of water vapor $e = 16$ mbar.

The *precipitable water content* is the total amount of water vapor in a vertical column of the atmosphere, if it would all condense, see also section 2.2.2.

2.3.4 The ionosphere

The ionosphere can be characterized by the ability of external sources to "knock-off" electrons from atoms, hereby creating *free* electrons which are not bound to their remaining ions. These external sources are mainly the solar ultraviolet and Röntgen radiation and energetic electrons of solar and magnetospheric origin. The number of (free) electrons is represented by the *electron density*, in electrons per m^3.

Although the electron density is temporally and spatially variable, the ionosphere is often treated as a spherical shell between 60 and 600 km height with a *constant* electron density in height for a certain time t. Radio signals traversing through the ionosphere are dispersively delayed along their paths by interactions with the free electrons. A dispersive delay means that the signal delay is frequency dependent, which is the key for, e.g., GPS or radar altimetry (dual-frequency) to estimate the ionospheric (or plasma) delay.

Physically, the ionospheric delay is a path integral through the ionospheric electron density. This integral therefore has the dimension electrons per m^2, and is commonly known as the Total Electron Content or TEC. If the path integral is taken in the zenith direction it is also known as the Vertical TEC (VTEC). To achieve favorable quantities, one TEC unit (TECU) is defined as:

$$1\mathrm{TECU} = 10^{16}\frac{\mathrm{electrons}}{\mathrm{m}^2} \tag{2.50}$$

The delay of a radio wave, propagating through the ionosphere, is different for the phase and the group velocity. Phase delay depends on electron content and affects carrier signals. Group delay depends on dispersion in the ionosphere as well, and affects signal modulation, i.e. the codes on GPS signals. The phase and group delays are of the same magnitude but opposite sign.

Two-hourly maps of the Vertical TEC for Europe are shown in figure 2.4, using dual frequency GPS observations collected by the IGS[4] network, provided by the DLR Remote Sensing Ground Station Neustrelitz. In this figure, apart from the normal diurnal variation, an ionospheric storm is visible as well (Ho et al., 1998).

Ionospheric gravity waves occur, e.g., when a sudden disturbance in ion density (e.g., a solar eclipse, waves over a mountain edge, heavy thunderstorms, earthquakes or rocket launches) triggers an expanding wave front. These wave normally have enormous wavelengths (hundreds of kilometers), and have gravity as restoring force. Cheng and Huang (1992) reported waves with a wavelength between 160 and 435 km after the eruption of Mount Pinatubo in 1991.

The ionosphere can be divided in a number of layers, which have different characteristics. The D-layer (80–100 km) receives only a minor part of the solar radiation, since most of the energy has been absorbed by higher ionospheric layers, and is therefore only weakly ionized. After sunset, this layer disappears completely. The E-layer (100–140 km) has little more ionization, but mostly fades into the F1-layer at night. The F1 and F2 layers, are located at 140–200, and 200–400 km respectively. Traveling Ionospheric Disturbances (TIDs) occur mainly in the F-layers. Large scale TIDs have wavelengths of 100–1000 km, and medium scale TIDs have wavelengths of approximately 100 km (Afraimovich et al., 1992).

---

[4] International GPS Service for Geodynamics

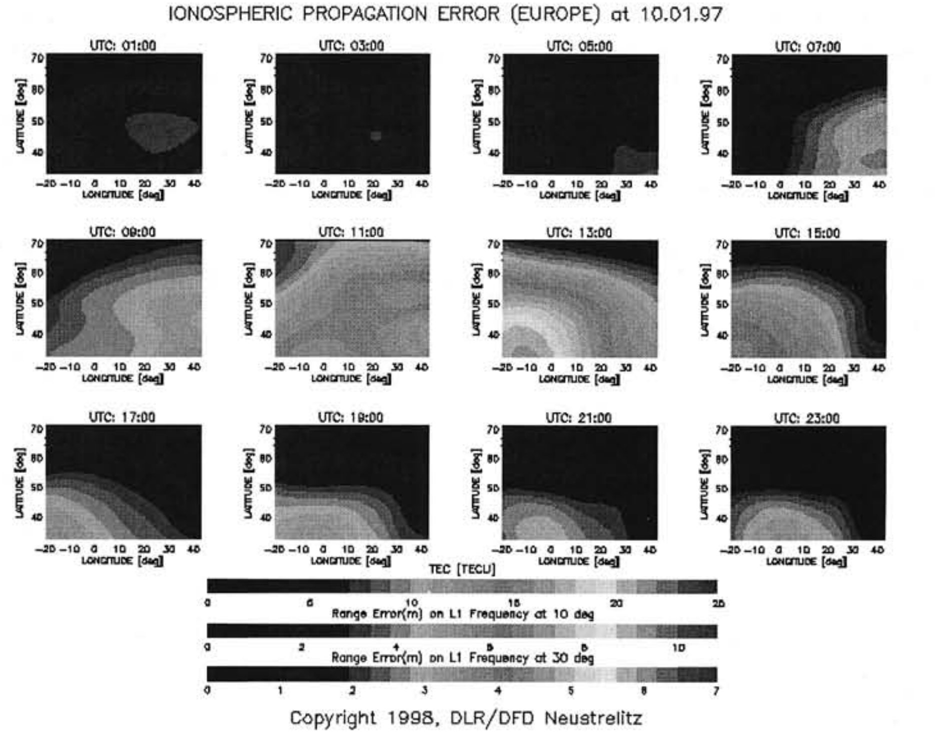

Figure 2.4 *Ionospheric map for 10 January 1997, (DLR Neustrelitz). The subimages show the two-hourly change in TEC from 1:00 UTC to 23:00 UTC. The daily variation can be observed as well as an ionospheric storm over south Spain and Morocco. The lower two colorbars give the range error for the two GPS frequencies, L_1 and L_2, showing the dispersive nature of the ionosphere.*

2.4 Signal propagation characteristics for SAR interferometry

Range errors described in literature are often described as a single ray, one way, zenith delay in meters. To assess their influence on SAR interferometry, some specific characteristics of the interferometric configuration need to be considered. A three step model is proposed to translate range errors to atmospheric errors in SAR interferograms:

Step 1 The zenith range error for a single ray, one way delay $\Delta R_e^z(x, y, t_1)$ at horizontal position (x, y) and time t_1, is mapped to an incidented, two way phase delay $\psi_1(x, y)$. A simple mapping function $1/\cos\theta$, where θ is the SAR look angle, and multiplication factor two yield[5]

$$\psi_1(x, y) = 2 \times \frac{1}{\cos\theta} \frac{2\pi}{\lambda} \Delta R_e^z(x, y, t_1). \tag{2.51}$$

---

[5] More sophisticated mapping functions such as described in (Niell, 1996) differ from $1/\cos\theta$ up to 1–1.5%.

Step 2 The two way single ray delay is extended to a multiple rays delay field, covering the full SAR scene. Due to the wrappedness of the phase, only the gradients $\partial/\partial x$ and $\partial/\partial y$ can be found. In x-direction this can be written as

$$\frac{\partial\psi_1(x,y)}{\partial x}=\frac{4\pi}{\lambda\cos\theta}\frac{\partial\Delta R_e^z(x,y,t_1)}{\partial x} \tag{2.52}$$

Step 3 The multiple ray, two way incidented delay of the first acquisition is differenced with that of the second acquisition. With $\varphi=\psi_1-\psi_2$, this results in

$$\frac{\partial\varphi(x,y)}{\partial x}=\frac{4\pi}{\lambda\cos\theta}\left(\frac{\partial\Delta R_e^z(x,y,t_1)}{\partial x}-\frac{\partial\Delta R_e^z(x,y,t_2)}{\partial x}\right). \tag{2.53}$$

From equation (2.53) it follows that the total vertical delay $\Delta R_e^z(x,y,t)$ is eliminated, and a double-difference observable is obtained: the difference between two horizontal gradient fields.

Note that there is an inherent conflict in this representation. The mapping function assumes a horizontally layered isotropic atmosphere, whereas the main interferometric observable is in fact the horizontal variation! Unless a detailed 3D refractivity field is available at the SAR acquisitions, there is no solution for this problem. It will, therefore, cause a horizontal shift of the phase artifacts with respect to the location of the physical atmospheric anomalies. This shift Δx can be estimated using the average expected height H of the physical anomaly by:

$$\Delta x=H\tan\theta\approx 0.4\cdot H. \tag{2.54}$$

In the following paragraphs some selected topics will be discussed, which can be of direct influence in SAR interferograms. Paragraph 2.4.1 reviews some results regarding horizontal gradients in tropospheric delay, and paragraphs 2.4.3 and 2.4.4 describes earlier findings on delay caused by rain and frontal zones respectively. Paragraph 2.4.5 describes some basic ideas of turbulence theory and how radially averaged spectra can be used to get an indication of the spectral characteristics of the observed differential interferograms. Finally, paragraph 2.4.6 and 2.4.7 address the ionospheric effects, first by giving a rule of thumb to assess the influence of the ionosphere, and second to distinguish between tropospheric and ionospheric effects.

2.4.1 Horizontal tropospheric delay gradients

Radiometer observations carried out by Alber et al. (1997) over a 43 km horizontal baseline give an indication of the horizontal gradient of the wet delay for a continental test site. A maximal wet zenith delay difference of 60 mm was observed. Davis et al. (1991) reported similar wet delay gradients for a coastal site: 0.1–1 N-units per km, cf. equation 2.27. Alber et al. (1997) observed pressure gradients of 1 mbar using plain barometric observations, which would correspond to a zenith dry delay gradient of approximately 3 mm. In their experiments, the maximum wet delay gradients were approximately 20 times larger than those from dry gradients.

2.4.2 The influence of clouds

Hall et al. (1996) have listed the liquid water content of clouds, see table 2.2. The maximum of the liquid water content is found at about 2 km above the cloud base. The liquid water content, W, can be related to the dielectric refractivity using the Clausius-Mossotti equation, (Solheim et al., 1997):

$$N_{\text{cloud}} = \frac{3}{2}\frac{W}{\rho_w}\frac{\varepsilon_0 - 1}{\varepsilon_0 + 2}, \tag{2.55}$$

where ε_0 is the permittivity of water and ρ_w is the density of liquid water. This relation is independent of the shape of the cloud droplet (Born and Wolf, 1980). Although the permittivity of water is a weak function of temperature, it is possible to approximate equation (2.55) to within 1% (Solheim et al., 1997) as:

$$N_{\text{cloud}} = 1.45W. \tag{2.56}$$

Since the value of N_{cloud} reflects the difference with the vacuum refractive index, equation (2.27) can be used to determine the additional delay $\Delta R_{e,\text{cloud}}$ caused by the liquid water in clouds:

$$\Delta R_{e,\text{cloud}} \quad [\text{in mm}] = \frac{1.45}{\cos\theta} W \quad [\text{per km}]. \tag{2.57}$$

Note that cloud droplet refractivity is in fact *dispersive*. However, since the dispersive part of the refractivity is much smaller than the non-dispersive part it can be ignored for C-band frequencies.

Type of cloud	Liquid water content [g/m^3]	Zenith delay [mm/km]
Stratiform clouds	0.05–0.25	0.1–0.4
Small cumulus clouds	0.5	0.7
Cumulus congestus and cumulonimbus	0.5–2.0	0.7–3
Ice clouds	< 0.1	< 0.1

Table 2.2 *Liquid water content in clouds, after Hall et al. (1996) and Bean and Dutton (1986)*

Table 2.2 shows the zenith delay for the four mentioned cloud groups. For repeat pass SAR interferometry, stratiform clouds and ice clouds do not cause large phase disturbances, due to their large horizontal extent and small additional delay. However, especially the cumulus type of clouds can result in significant additional phase delay, as they have a relatively limited horizontal size combined with a large vertical height and liquid water content.

2.4.3 The influence of rain

Rain characteristics can be divided into two types (Goldhirsch and Rowland, 1982): stratiform rain (non-convective), and thunderstorm (convective). Stratiform rains are generally widespread (hundreds of kilometers) and have rain rates of less then 20 mm/hr. This type of rain is assumed to fall from near the 0°C isotherm. This implies rain fall paths of 4–5 km in summertime (for latitudes of 15–45° north). Convective rain cells have a horizontal extent in the order of kilometers and many of these cells can occur embedded in a thunderstorm. In this type of rain, drops are often carried in a supercooled state to several km above the 0° isotherm. The rain fall path can be up to 10 km.

Rogers and Olsen (1975) have published curves which express the relationship between the range error through rain as a function of the rain rate in mm/hr, see figure 2.5, based on experimental results. From these curves it follows that for a 5 km nadir rain path and a 100 mm/hr rain (thunderstorm), the range error for a two way path is 5 cm. For a stratiform type of rain with 10 mm/hr (moderate rain) over a 5 km path, the two-way range error is 1 cm (Goldhirsch and Rowland, 1982). Since the convective rains are much more localized, they will cause larger gradients and will be more prominently visible in the interferograms. The results from Rogers and Olsen (1975) were obtained at 6 GHz, but are expected to deviate little for the 5.3 GHz frequency of the ERS SAR.

The correspondence between the size (diameter) of the rain cells and the rain rate is studied by Edgar et al. (1973), and Nathanson (1969), and the results are shown in figure 2.6. It is found that rainfall diameters of 20 km and larger have rainfall rates of 10–15 mm/hr or less. Larger rain rates are confined within smaller diameters. Crane (1996) gives an extended overview of the statistics and structure of rain.

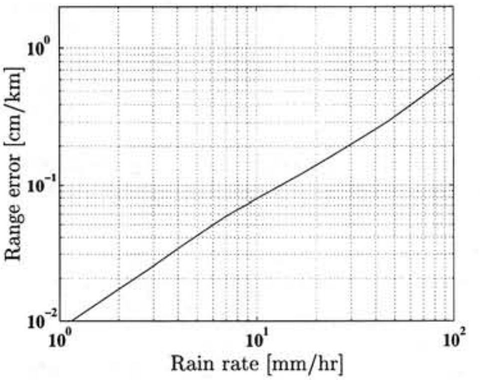

Figure 2.5 *One way range error per km through uniform rain. Curves are adapted from Rogers and Olsen (1975) (Goldhirsch and Rowland (1982))*

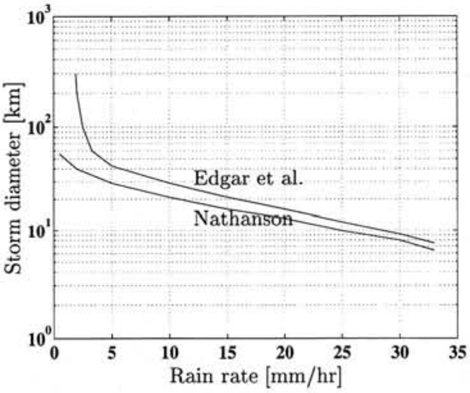

Figure 2.6 *Storm diameter versus rainfall rate, according to Edgar et al. (1973) (the upper profile), and Nathanson (1969) (the lower profile)*

2.4.4 The influence of frontal zones

High and low pressure centers (highs and lows) cause circulation patterns of the surrounding air masses. Highs are characterized by downward motion (*subsidence*) aloft, and horizontal spreading air (*divergence*) near the surface. Winds are mostly light, and cloud development is impeded. Fronts are usually associated with lows, and two fronts per low are most common, a cold front and a warm front(Stull, 1995).

Fronts mark the boundaries between air masses. Important attributes are (Stull, 1995):

- strong horizontal temperature, moisture and wind gradients,

- strong vertical shear of the horizontal wind,
- relative minimum of pressure, and
- clouds and precipitation.

Along a cold front there are narrow bands of cumuliform clouds, with possible thunderstorms (Cb's) and scattered showers. The winds are stronger and gusty, and the pressure reaches a relative minimum. On the northern hemisphere, wind shifts and advects colder air from the north. As this cold air advects over the warmer ground, it becomes unstable, convective, and very turbulent. Warm fronts are more spatially extended. The leading edge of the front is formed by cirrostratus clouds, followed by altostratus, stratus, and possibly nimbostratus clouds which form a rain band.

A simulation of the effect of a cold front on the interferometric phase can be performed using the distribution of the refractivity around an idealized cold front, as described in Bean and Dutton (1986). The cold front is shown in figure 2.7, where the fat line indicates the cold front, and the isopleths are lines of equal refractivity N. The one-way zenith delay caused by the lower half of the cross section is shown in figure 2.8, just over the simulated interferometric phase, assuming a second image with horizontal homogeneous layers, and a look angle of 23 degrees. For distances within 100 km, the front results in at most one cycle phase variation, with a phase "hump" just over the surface front.

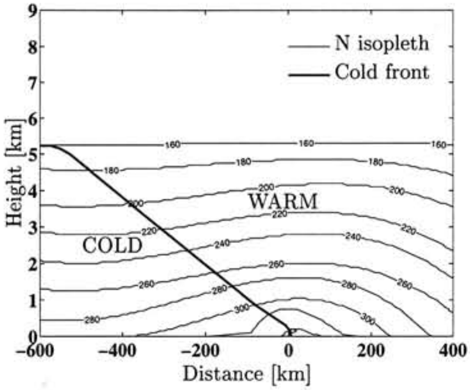

Figure 2.7 *Refractivity isopleths over an idealized cold front. The diagonal line indicates the position of the front.*

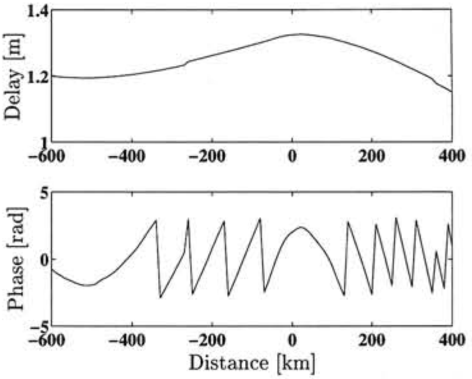

Figure 2.8 *One way zenith delay, and its result on the two-way incidented interferometric phase, caused by the cold front.*

2.4.5 Turbulence measures

Atmospheric turbulence causes refractive index fluctuations, causing phase fluctuations in SAR interferograms. The effects of turbulence can be modeled in terms of Kolmogorov theory.

In the Kolmogorov theory the dynamics of refractive index fluctuations are used to predict the properties of phase distortions introduced into a wave propagating through turbulence.

Kolmogorovs theory of turbulence predicts that refractive index fluctuations can only come about in a specific way - that is, they have well defined statistics which are weighted only by a single parameter - the strength of turbulence (C_N^2).

The *turbulence structure function* for a 3-D refractivity field, is defined as (Treuhaft and Lanyi, 1987)(Ruf and Beus, 1997):

$$D_N(s) = \mathrm{E}\{(N(\vec{x}) - N(\vec{x}+\vec{s}))^2\} \tag{2.58}$$

where $N(\vec{x})$ is the refractivity at $\vec{x}$, s is the magnitude of the separation between the points and E denotes the expectation over all realizations of the random function $N(\vec{x})$. While the separation s lies within the inner and outer limits of isotropic turbulence, Kolmogorov turbulence theory predicts (Tatarski, 1961);

$$D_N(s) = C_N^2 s^{2/3}, \tag{2.59}$$

where C_N^2 is the structure constant.

When measuring the integrated refractivity along a vertical path through the atmosphere, the separation s can only be determined in the horizontal plane. Using the range error $\Delta R_e = 10^{-6}\int_0^H N dh$ as main observable, a turbulence structure function can be defined for the (horizontal) range error field as for the 3-D refractivity field:

$$D_{\Delta R_e}(s) = \mathrm{E}\{(\Delta R_e(\vec{x}) - \Delta R_e(\vec{x}+\vec{s}))^2\} \tag{2.60}$$

For separations s within the inner and outer scales of isotropic turbulence, Kolmogorov theory predicts the relationship (Tatarski, 1961):

$$D_{\Delta R_e}(s) = C_{\Delta R_e} s^{5/3}. \tag{2.61}$$

According to Ruf and Beus (1997) the factor 5/3 decreases to 0 as s reaches the outer scale of turbulence. An estimate of the power law dependence can be found using a log/log linear regression of $D_{\Delta R_e}(s)$ versus s:

$$\log(D_{\Delta R_e}(s)) = \beta \log(s) + \log(C_{\Delta R_e}). \tag{2.62}$$

where β should approach 5/3 for regions of turbulence.

2.4.5.1 Relation between the structure function and the radial averaged spectrum

Following the derivation of Tatarski (1961), the spatial structure function can be defined as

$$\begin{aligned} D_f(r) &= \mathrm{E}\{(f(x+r) - f(x))^2\} && (2.63)\\ &= \mathrm{E}\{(f(x+r)^2\} + \mathrm{E}\{(f(x)^2\} - 2\mathrm{E}\{f(x+r)f(x)\} && (2.64)\end{aligned}$$

If $R_f(r)$ is the autocorrelation function, we can write 2.63 as

$$D_f(r) = 2(R_f(0) - R_f(r)). \tag{2.65}$$

As long as $R_f(\infty) = 0$, this means that $D_f(\infty) = 2R_f(0)$, and we can describe the autocorrelation function in terms of the structure function

$$R_f(r) = \frac{1}{2}D_f(\infty) - \frac{1}{2}D_f(r). \tag{2.66}$$

According to the Wiener-Khinchine theorem, the spectral density $S(\omega)$ is the Fourier transform of the autocorrelation function, and therefore

$$R_f(r) = \int_{-\infty}^{\infty} e^{i\omega r} S(\omega) d\omega = \int_{-\infty}^{\infty} \cos(\omega r) S(\omega) d\omega. \tag{2.67}$$

Substituting 2.67 in 2.66, we find

$$\begin{aligned} D_f(r) &= -2R_f(r) + D_f(\infty) = -2R_f(r) + 2R_f(0) && (2.68) \\ &= 2\int_{-\infty}^{\infty} (1 - \cos\omega r) S(\omega) d\omega. && (2.69) \end{aligned}$$

For a spectral density function $S(\omega) = A|\omega|^{-(p+1)}$, with $A > 0$, and $0 < p < 2$, we find the structure function using 2.68:

$$\begin{aligned} D_f(r) &= 2A \int_{-\infty}^{\infty} (1 - \cos\omega r)|\omega|^{-(p+1)} d\omega && (2.70) \\ &= \frac{2A\pi}{\sin\frac{\pi p}{2}\Gamma(1+p)} r^p. && (2.71) \end{aligned}$$

In other words, the structure function $D_f(r) = c^2 r^p$, with $0 < p < 2$, corresponds to the spectral density function

$$S(\omega) = \frac{\Gamma(1+p)}{2\pi} \sin\frac{\pi p}{2} c^2 |\omega|^{-(p+1)} \tag{2.72}$$

An observed spectral density with a $-5/3$ power law will therefore correspond to a structure function $D_f(r) = c^2 r^{2/3}$.

2.4.6 Ionospheric influence

Using equation (2.39), step 2 of the model yields

$$\frac{\partial\psi_1(x,y)}{\partial x} = \frac{4\pi}{\lambda\cos\theta} \frac{-40.28}{f^2} \frac{\partial TEC(x,y,t_1)}{\partial x}. \tag{2.73}$$

Using TEC units of $10^{16}\mathrm{m}^2$, this is

$$\frac{\partial\psi_1(x,y)}{\partial x} = -0.55 \frac{\partial TEC(x,y,t_1)}{\partial x} \cdot 2\pi. \tag{2.74}$$

This means that a horizontal change of 1 TECU over one SAR scene results in a phase ramp of -0.55 cycle. In the interferometric phase, step 3, the difference of two phase observations is taken, hereby largely eliminating daily variation. Note that the sign of the factor is negative, i.e. an increase in TEC results in a phase advance.

Following equation (2.74), if ionospheric effects have an observable influence in a single SAR scene, the dominant wavelength should be less than 100 km, to distinguish them from orbit errors, while the amplitude should be more than 0.36 TEC, to get a signal of 0.2 phase cycles.

The only natural phenomena that could possibly cause such effects are small scale Traveling Ionospheric Disturbances (TIDs), with a wavelength of tens of km (Spoelstra, 1997). These TIDs are wave effects, mostly propagating from polar regions to regions with lower latitudes.

2.4.7 Distinguishing between ionospheric and tropospheric effects

The difference between ionospheric and tropospheric effects on SAR interferometry is based on two characteristics: the sign of the delay and the shape of the feature. From equation 2.39, it follows that increase in the ionospheric electron content results in a decrease of the observed range, or a *phase advance*. An area of increased partial water vapor pressure, see equation 2.28, results in an increase in the observed range, or a *phase delay*. However, there are two complications:

1. one has to know during which of the two SAR images the effect occurred: a phase *advance* in the first image gives the same result as a phase *delay* in the second one, and
2. one has to distinguish which area in the interferogram can be regarded as reference area, where the phase is relatively undisturbed: a localized area with *reduced* water vapor density yields a localized relative *advance* of the phase.

The first complication can be solved only when using more than two SAR images. The different interferometric combinations of images enables the unambiguous identification of the image containing the errors, as long as other error sources such as temporal decorrelation allow for such an evaluation. Since for this study only single interferometric pairs were used, it is not possible to distinguish between phase delay and advance based on only interferometric data.

The second complication, however, is much harder to circumvent. Just as localized areas with an increased water vapor content occur frequently, in a relative sense also areas with a lesser amount of water vapor occur. This can be clearly observed in, e.g., Meteosat water vapor channel imagery. Therefore, without any additional information it is not possible to uniquely identify ionospheric effects in interferograms based on the phase sign of the feature.

The remaining possibility for identification is based on the shape and characteristics of the feature. The main difficulty in this respect is the limited knowledge about the spatial characteristics of the ionosphere within ranges of less than 100 km. Although different devices using dual-frequencies have observed the ionosphere, their results have either been only one-dimensional integrated profiles (as is, e.g., possible with GPS), or large scale interpolated ionospheric maps, which do not have the spatial resolution needed for InSAR.

Based on these evaluations, it is difficult to uniquely identify ionospheric effects in SAR interferograms at present, unless strong support from additional sources is available. It should be noted however, that further research in this field, using, e.g., dual frequency SAR interferometry, could be extremely valuable for its ionospheric imaging capacities.

Chapter 3

Interferometric Database

This chapter describes the interferometric database analyzed in this study. The choice of suitable test sites is discussed using a set of selection criteria, and the coding conventions used in chapter 5 are listed. The second section briefly describes the used procedure in the interferometric processing and the post processing, such as a posteriori multilooking, extraction of the reference elevation model, orbit errors, and masking.

key words: interferometric processing, selection criteria, DEM

3.1 Test site locations

The repeat pass interferometric phase can be considered as a juxtaposition of several physical signals, such as topography, deformation in slant range direction, propagation delays, orbital configuration, surface penetration, changes in the dielectric properties of the surface, and noise due to different kinds of decorrelation. In order to investigate one specific signal one has to carefully remove the influence of all the others.

For this study the main focus is on the influence of atmospheric effects or propagation delay differences. In order to eliminate or minimize the effects of other signals, test sites were chosen with near optimal conditions. Since topography in the Netherlands is limited and very well known, test sites in this area are either free of topographic phase or it can be easily corrected for. In order to minimize the effect of temporal decorrelation and possible deformations between the image acquisitions, ERS tandem imagery was used only. More than one test site was chosen, in order to analyze an amount of interferograms which is enough to cover a full seasonal cycle. The use of different test sites also provides possibilities to discern between coastal and more inland areas. Interferometric phase changes due to the orbital configuration were minimized using precise a posteriori orbit information.

Now, the remaining interferometric phase consists of atmospheric propagation heterogeneities and surface interaction. It is observed that phase signatures due to surface interaction are mostly of limited spatial extent, and often strongly correlated with differences in land use, which can be detected in the SAR backscatter imagery. Therefore, for the majority of interferometric phase signal, it can be concluded that only the atmosphere is being observed.

Figure 3.1 shows the location of the test sites and SAR frames. The frames are coded as described in table 3.1. The dots at the map indicate the positions of the meteorological

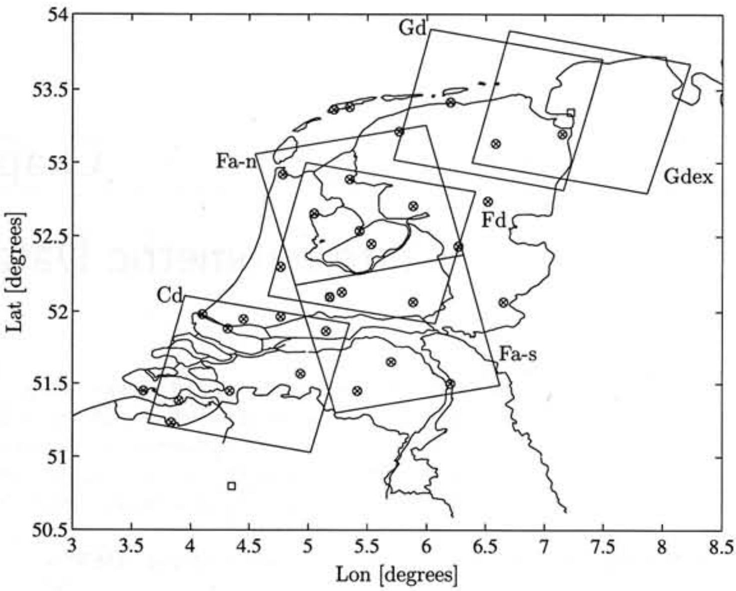

Figure 3.1 *Location of the test sites, SAR acquisitions and meteorological stations. The circles indicate synoptic stations, the squares are radiosonde locations.*

stations, whose information was used in the interpretation of the interferograms. The large amount of available meteorological observations was in fact another reason for this particular choice of test locations in the Netherlands.

Code	Full name
gd	Groningen descending
gdex	Groningen descending, adjacent track
fd	Flevoland descending
fa-n	Flevoland ascending north
fa-s	Flevoland ascending south
cd	CLARA (Delft) descending

Table 3.1 *Codes used for the different test sites. The CLARA interferogram was acquired during the CLouds And RAdiation meteorological experiment.*

3.1.1 List of interferograms

The 26 interferograms analyzed in this study are categorized according to their location. The database with SAR-SLC input data, and interferometric combination, is listed in table 3.2. The list shows the identification code, dates of acquisition, orbit number, the SAR processing and archiving facility, and the estimates for the parallel baseline and the perpendicular baseline. Track and frame numbers are shown at the top of each location. The position of the interferograms is shown in figure 3.1.

No.	ID	Date	ERS-1	PAF	ERS-2	PAF	$B^{\parallel}$	$B^{\perp}$
Groningen descending, track 380 frame 2529								
1	Gd-1	15/16-07-95	20909	D	1236	I	3	-27
2	Gd-2	19/20-08-95	21410	D	1737	D	37	81
3	Gd-3	02/03-12-95	22913	D	3240	D	17	44
4	Gd-4	16/17-03-96	24416	I	4743	I	16	-18
5	Gd-5	20/21-04-96	24917	D	5244	D	34	67
6	Gd-6	25/26-05-96	25418	I	5745	I	52	99
7	Gd-7	03/04-08-96	26420	UK	6747	I	46	103
Flevoland descending, track 151 frame 2547								
8	Fd-1	03/04-08-95	21181	D	1508	D	32	58
9	Fd-2	07/08-09-95	21682	D	2009	D	30	37
10	Fd-3	12/13-10-95	22183	D	2510	D	-127	-324
11	Fd-4	16/17-11-95	22684	D	3011	D	259	531
12	Fd-5	21/22-12-95	23185	D	3512	D	62	173
13	Fd-6	04/05-04-96	24688	I	5015	D	26	59
14	Fd-7	13/14-06-96	25690	UK	6017	D	45	77
Flevoland ascending south, track 29 frame 1035								
15	Fa-s1	29/30-08-95	21560	D	1887	D	-31	-80
16	Fa-s2	03/04-10-95	22061	D	2388	D	146	393
17	Fa-s3	26/27-03-96	24566	D	4893	D	-21	-33
18	Fa-s4	30-04/01-05-96	25067	UK	5394	UK	-31	-59
19	Fa-s5	04/05-06-96	25568	UK	5895	I	-35	-89
Flevoland ascending north, rack 29 frame 1053								
20	Fa-n1	29/30-08-95	21560	D	1887	D	-30	-79
21	Fa-n2	03/04-10-95	22061	D	2388	D	144	385
22	Fa-n3	26/27-03-96	24566	D	4893	D	-21	-32
23	Fa-n4	30-04/01-05-96	25067	UK	5394	UK	-30	-57
24	Fa-n5	04/05-06-96	25568	UK	5895	I	-34	-88
CLARA (Delft) descending, track 423 frame 2565								
25	Cd-1	23/24-04-96	24960	UK	5287	UK	38	78
Groningen adjacent descending, track 108 frame 2529								
26	Gdex-2	26/27-02-96	24144	D	4471	D	-15	-31

Table 3.2 *A listing of the interferograms of this study. The interferograms have been coded, in the second column. The fourth and sixth column give the orbit numbers for ERS-1 and ERS-2 respectively, the fifth and seventh column indicate the Processing and Archiving Facility, responsible for the SAR-SLC processing (**D**: German, **I**: Italian, and **UK**: the United Kingdom). The last two columns give an estimation for the parallel baseline and the perpendicular baseline in meters.*

3.2 Processing of the interferograms

The interferometric processing was performed using DLRs GENESIS system (Schwäbisch and Geudtner, 1995; Schwäbisch, 1995; Eineder and Adam, 1997). First, the two full single look complex (SLC) ERS SAR images are coregistered and the corresponding regions are determined. Spectral filtering is applied to reduce the effect of baseline induced noise. After fast resampling of the second image, complex multiplication is performed to obtain the phase interferogram. Precise orbit information was used from DLR-GFZ and in some cases DEOS. Based on the orbit state vectors, a reference interferogram based on the WGS84 ellipsoid is subtracted, which yields the "flattened" interferogram.

In first instance, a multilook level corresponding to 2 resolution cells in range, and 10 in azimuth direction was chosen. Coherence images were calculated and used for further analysis. Phase unwrapping was performed using either the minimal cost flow (Costantini, 1996) algorithm implementation at DFD-DLR, or the method of Ghiglia and Romero (1994). The first method resulted in an almost perfect unwrapped interferogram, although some areas which were isolated by water had 2π jumps. These, however, were easily recognized and mostly corrected for afterward. The second method did not have the 2π jumps (except for some islands), but had a limited amount of unwrapping "pits" caused by unconnected residues. When necessary, these pits were corrected for manually.

3.2.1 A posteriori multilook

To reduce data size and facilitate storage capacities, the interferograms are subsampled by a factor 4 in range and azimuth direction. The pixels in the images now roughly correspond to a ground area of 160 × 160 meters. Since it is expected that atmospheric signal below this pixel size is not strong enough to be distinguished in the interferograms, this appeared to be a practically useful choice.

3.2.2 Reference elevation model

The standard elevation model *TopHoogteMD* (Topografische Dienst Nederland and Meetkundige Dienst Rijkswaterstaat, 1997) was used to correct for the topographically induced phase variation. This was necessary only for those situations which had significant topography in combination with a rather large baseline. The TopHoogteMD DEM consists of heights with respect to the local NAP[1] reference surface, which are close to orthometric heights with respect to the geoid. The used coordinate system is the local RD[2] system, which is transformed to WGS84 coordinates for this study.

Depending on the analysis, two methods were followed. In the first, the orbit information of the spacecraft was used to calculate a synthetic interferogram from the reference DEM. This synthetic interferogram was compared with the observed interferogram, and registered using a maximum correlation method. Subtraction of the synthetic interferogram from the observed interferogram yielded the differential interferogram. The differential interferogram is still in the slant-range azimuth coordinate system, but reveals no more topographic phase variation. In the second method, the observed interferogram was geocoded to the WGS84 latitude-longitude system. In this reference system, the reference

---

[1] Normaal Amsterdams Peil

[2] Rijksdriehoeksmeting

DEM can be easily subtracted, yielding a geocoded differential interferogram.

After the elimination of the topographic phase, only differential signal remains in the interferograms. Since the time interval between the SAR acquisitions was only 24 hours, it is not expected that significant deformations occurred in between, and therefore the only phase signal should be of atmospheric nature.

3.2.3 Orbit errors

The orbit accuracy of the used precise orbits is still not sufficient, and causes especially for small perpendicular baselines long wavelength disturbances in the interferograms. These disturbances are eliminated using the reference interferogram, and minimizing the overall error. Note that the use of tie-points in interferograms which have strong atmospheric artifacts can be a problem. Atmospheric phase gradients which are unaccounted for will result in tilts in the derived height model. Using a great number of tie-points will help minimizing this problem, although large scale atmospheric disturbances, e.g., those connected to frontal zones, will still cause remaining tilts.

3.2.4 Masking

Water areas and severely decorrelated areas (sometimes forests) are masked using coherence measures. For some interferograms, additional manual masking or de-masking is applied to optimize the interpretation of the phase information.

Chapter 4

Meteorological Database

This chapter briefly covers some important aspects of the meteorological information used for the interferogram analysis. In the first section, the different scales in atmospheric dynamics are briefly reviewed, followed by spatial and temporal scales in the observation networks used in this study. The second section gives an overview of the data sources and instrumentation used to interpret the series of interferograms in chapter 5. The two last sections provide some information on the feasibility of using contemporary meteorological models for the purpose of ERS SAR interferometry, and the code system used for automatic exchange of meteorological information.
key words: scales, observations, instrumentation, models, codification.

4.1 Scales

Both atmospheric phenomena and consequently observation networks cover a large bandwidth in spatial and temporal scales, reaching from microturbulence to global atmospheric phenomena, and from sub-seconds for microscale turbulent mixing to centuries for climatic change. The following sections describe the most important features of both atmospheric and observation scales. The subdivision in scale groups is important to assess which processes are influencing the spatial and temporal characteristics of SAR interferograms.

4.1.1 Scales in atmospheric phenomena

Much of the activity of the atmosphere can be arranged in a small number of temporal and spatial scales. Table 4.1, adjusted from McIlveen (1995), lists a number of weather-related atmospheric disturbances with its respective scale characteristics. The bold-faced part of the table represents the phenomena which can be observed using tandem ERS SAR interferometry.

Convection ranges from small cumulus to big showers, *Mesoscale systems* consists of shower patterns, sea breezes, etc., *Synoptic scale systems* are extratropical and tropical cyclones etc., and *Hemispheric scale systems* are, e.g., long waves in tropospheric flow. Only the first three processes have spatial scales within the range of full scene range of ERS SAR interferograms.

spatial range [m]	Disturbance	temporal range [sec]
10^{-3}—10^{3}	**Turbulence**	10^{-1} — 10^{3}
10^{1}—10^{3}	**Convection**	10^{2} — 10^{4}
10^{3}—10^{5}	**Mesoscale systems**	10^{3} — 10^{5}
10^{5}—10^{7}	Synoptic scale systems	10^{4} — 10^{5}
$> 10^{7}$	Hemispheric scale	10^{6} — 10^{7}
$> 10^{7}$	Seasonal	10^{7} — 10^{9}
$> 10^{7}$	Climatic	$> 10^{9}$

Table 4.1 *Temporal and spatial scales in atmospheric dynamic processes (McIlveen (1995)). The bold faced disturbances are in the range of SAR interferometric observation.*

4.1.2 Observation scales

Like the different spatial and temporal scales in the atmospheric phenomena, the network of observations can also be developed into several scales (McIlveen, 1995). Actually, specific scales of atmospheric phenomena are referred to using observation network scales.

4.1.2.1 Surface network

The network of surface stations (operating manually or automatically) that are making *synoptic* (simultaneous) observations is also called the *synoptic network*. This synoptic network is able to define cyclones, anti-cyclones and their smaller scale frontal systems, which are therefore defined as *synoptic scale* weather phenomena. The synoptic scale network, however, fails to observe sub-synoptic scale systems such as shower clouds and the quite substantial clusters they sometimes form. Yet, the Netherlands can be regarded as a relatively well equipped country, with a number of 32 surface stations within an area of 200 × 300 km.

Regarding the temporal scales of the synoptic network, hourly observations of wind, temperature, humidity, pressure, visibility and cloud and weather types are made at each station of the network, just before the hour (in UTC). The precipitation totals, the manual gauge readings, are performed at 9:00 and 21:00 Local Time (LT), to reveal the systematic differences between day and night.

The weather radar network is also a part of the surface network. Weather radars can give a more specific overview of all substantial precipitation within range, although the field of view decreases with increasing range. The resolution is approximately 2 km at a distance of 100 km from the instrument.

4.1.2.2 Upper air network

Radiosondes provide observations of wind, temperature, relative humidity and pressure. From the De Bilt station, every 6 hours a sonde is released, which climbs with approximately 5 m/s to heights of 20–30 km. Temperature, humidity and pressure is sent by radio to the ground station, wind speed and direction are obtained by automatic tracking of the sonde by triangulation techniques.

4.1.2.3 Satellite network

Meteorological satellites make use of existing radiation emitted or reflected from the atmosphere. One or more wavelength bands are being observed by radiometers, usually in the visible and infra-red range. Visible range imagery reveals the reflectance of sunlight on clouds. Therefore, it cannot be used at night. Infra-red sensing measures the terrestrial radiation emitted by the Earth's surface and atmosphere. The choice of the wavelength in the infra-red band determines the ease with which the clear air can be penetrated, and therefore, the elevation from which the emission originates. Horizontal resolutions for satellite imagery start from a few kilometers, and temporal sampling is dependent on the orbital configuration and the scanning rates of the instruments.

4.2 Data sources

This section describes the used data and instruments for the current study. The characteristics of the different instruments are summarized, and the resulting meteorological parameters are discussed.

4.2.1 Meteorological satellites

Satellite weather imagery provides different types of information. From observations in the visual channel, cloud types and coverage can be determined. Using infrared (IR) imagery, the heights of cloud tops can be studied, as well as temperature gradients between ocean and land. Water vapor imagery gives information on the integrated water vapor in the atmosphere. For all channels, a series of images provides information on wind speeds at different height levels. In this study, two spaceborne instruments are used: AVHRR and Meteosat.

4.2.1.1 AVHRR

The NOAA Advanced Very High Resolution Radiometer (AVHRR) has a spatial resolution of 1.1×1.1 km at nadir. It uses a whiskbroom scanner covering a ground swath of approximately 2000 km. The NOAA satellites are in a nearly polar, sun-synchronous orbit with a revolution time of approximately 100 minutes. The combination of two operational satellites with this wide ground swath allows a coverage of some 6–8 times per 24 hours. There are five channels:

- 0.58 – 0.68 micron,
- 0.73 – 1.1 micron,
- 3.6 – 3.9 micron,
- 10.3 – 11.3 micron, and
- 11.5 – 12.5 micron.

A combination of channels, assigning a different color to each channel, can help the visualization and interpretation of the data. For this study, a combination of channel 1, 2, and 4 is used. The cold cirrus clouds are shown in white, while the warmer medium and lower level clouds have more yellowish colors. AVHRR imagery can be used to get an overview of the general atmospheric situation, the position of frontal zones, and the type of cloud cover.

4.2.1.2 Meteosat

Meteosat imagery is obtained with a temporal sampling of 1 acquisition per half hour for each channel, according to a predefined scheme—e.g., no visual observations during nighttime—and with a spatial resolution of 5×5 km at nadir. For the latitude of the Netherlands, the spatial resolution is 5×9 km. Meteosat uses three channels:

- 0.5 - 0.9 micron (visual channel),
- 5.7 - 7.1 micron (water vapor channel), and
- 10.5 - 12.5 micron (infrared channel).

Meteosat is a geostationary satellite (35800 km height) located above the Greenwich meridian, and uses a spin scan radiometer to return images in the visible, infrared, as well as the water vapor band. The satellite records either the *normal visual*, *infrared* and *water vapor* combination, or only the so called *double visual* combination. The resolution at nadir is 5.0 km for infrared, water vapor, and normal visible, and 2.5 km for double visible. Due to the curvature of the Earth, the resolution along the meridian scales with $1/\cos(\varphi)$, where φ is the geocentric latitude. For the Netherlands, this means a resolution of about 5×8 kilometers in the first three modes, and 2.5×4 in the Double Visual mode. Therefore, it is not possible to discern small cumulus clouds. It is however, possible to get an overview of the weather situation, the location of fronts and depressions, etc. The higher temporal sampling, when compared to AVHRR, provides a better correlation with the ERS SAR acquisitions.

4.2.2 Weather radar

The weather radar data are a combination of the data acquired by two active radars: De Bilt and Schiphol. These radars use C-band microwave pulses and measure the scatter due to precipitation particles. The scatter intensity, azimuth direction and elevation angle of the radar, and time delay are combined into a scatter map, where the scatter intensity can be related to the precipitation rate in mm/hr. Such a scatter map is available every 15 minutes, and a series of scatter maps over some hours gives a clear insight in the progression and development of precipitation fields. The radar echos with highest elevation can be determined using the range and elevation. Corrections are applied for beam attenuation in rain, refraction, and side lobe echos.

By plotting the radar reflectivity against the rain rate, it has been found that it follows a power-law relationship: $Z = aR^b$, where Z is the radar reflectivity in units of (mm^6/m^3) and R is the rain rate in mm/hr. The relationship used by the KNMI radars is $Z = 200R^{1.6}$. The accuracy can often be a factor 3 too large or too small (Wessels, 1997). The beam width of the antenna is 1 degree, resulting in a linear decay in azimuth resolution moving away from the antenna.

Possible erroneous interpretation of the radar signal can be caused by the scattering of, e.g., inversion layers and high buildings. However, due to the characteristics of these signals, they can mostly be discerned from real precipitation. A further important feature of the radar is the lack of signal from the lowest levels of the atmosphere, which becomes dominant for precipitation far from the radar instrument, due to the Earth's curvature.

Therefore, it is possible that the radar senses precipitation up to hundred kilometer from the instrument, although this precipitation does not reach the ground, due to evaporation along its path.

4.2.3 Radiosonde

Radiosonde data (in meteorology also known as *TEMPs*) are acquired at a large number of meteorological stations in the world. Within the framework of the World Meteorological Organization (WMO), all observations are performed at the "synoptic" hours: 0, 6, 12, and 18 h UTC. The sonde performs the ascent in about one hour. At specified pressure levels a minimal set of observations is extracted and transfered to the national and international meteorological organizations.

The radiosonde system consists of an *instrument package*, a *radio receiver* a *tracking unit*, and a *recorder* (Hopkins, 1996). The instrument package contains a *thermistor*, which measures temperature with an accuracy of 0.2°C, a *hygristor*, which senses the relative humidity in the range from 15% to 100%, with an accuracy of 3.5%, and an *aneroid barometer* which measures pressure (Elliot and Gaffen, 1991). Apart from these meteorological instruments, it contains a radio transmitter and a battery. Wind speed and direction are obtained at the ground unit, tracking the sonde using triangulation.

The radiosonde transmits the measured temperature and relative humidity at each pressure level. The altitudes of these levels are calculated using the hypsometric equation. The recorded parameters are then plotted in a *thermodynamic diagram*, see figure 4.1. Note that there are many variations of thermodynamic diagrams possible. The diagram in figure 4.1 shows the *liquid water potential temperature* at the vertical lines, and pressure at the horizontal lines.[1] Using this convention, the vertical lines are *saturated adiabates.* The real temperature is shown as the diagonal straight lines. Furthermore the *dry adiabates* are indicated as the dotted curved lines. These lines represent the change in temperature that a dry air parcel would undergo if moved up and down in the atmosphere and allowed to expand or become compressed (in a dry adiabatic process) because of the air pressure change in vertical direction. The dry adiabates converge to the saturated adiabates at some height. Finally *isohumes* or *saturation mixing ratio lines* are shown as dashed diagonal lines. These lines define the maximum amount of water vapor that could be held in the atmosphere (the saturation mixing ratio) for each combination of temperature and pressure. These lines can be used to determine whether a parcel is saturated or not. For a certain pressure, the combination with the air temperature yields the saturation mixing ratio, and with the dew point temperature it yields the actual mixing ratio.

The combination of the dewpoint temperature and the air temperature in a thermodynamic diagram reveals a wealth of meteorological information on, e.g., cloud formation, atmospheric stability, and inversion layers.

The wind direction and speed is plotted using the standard meteorological convention for showing winds. The feathers, or *barbs*, indicate the wind speed: a long barb is 10 knots,

---

[1] The potential temperature is the temperature an air parcel would have at a certain reference pressure level if the dry adiabatic temperature changes during vertical displacement would be removed (Stull, 1995). In other words, if an air parcel is moved vertically in a dry adiabatic way, the potential temperature does not change. The liquid water potential temperature describes the temperature of a fully saturated parcel, moved vertically along the saturated adiabat.

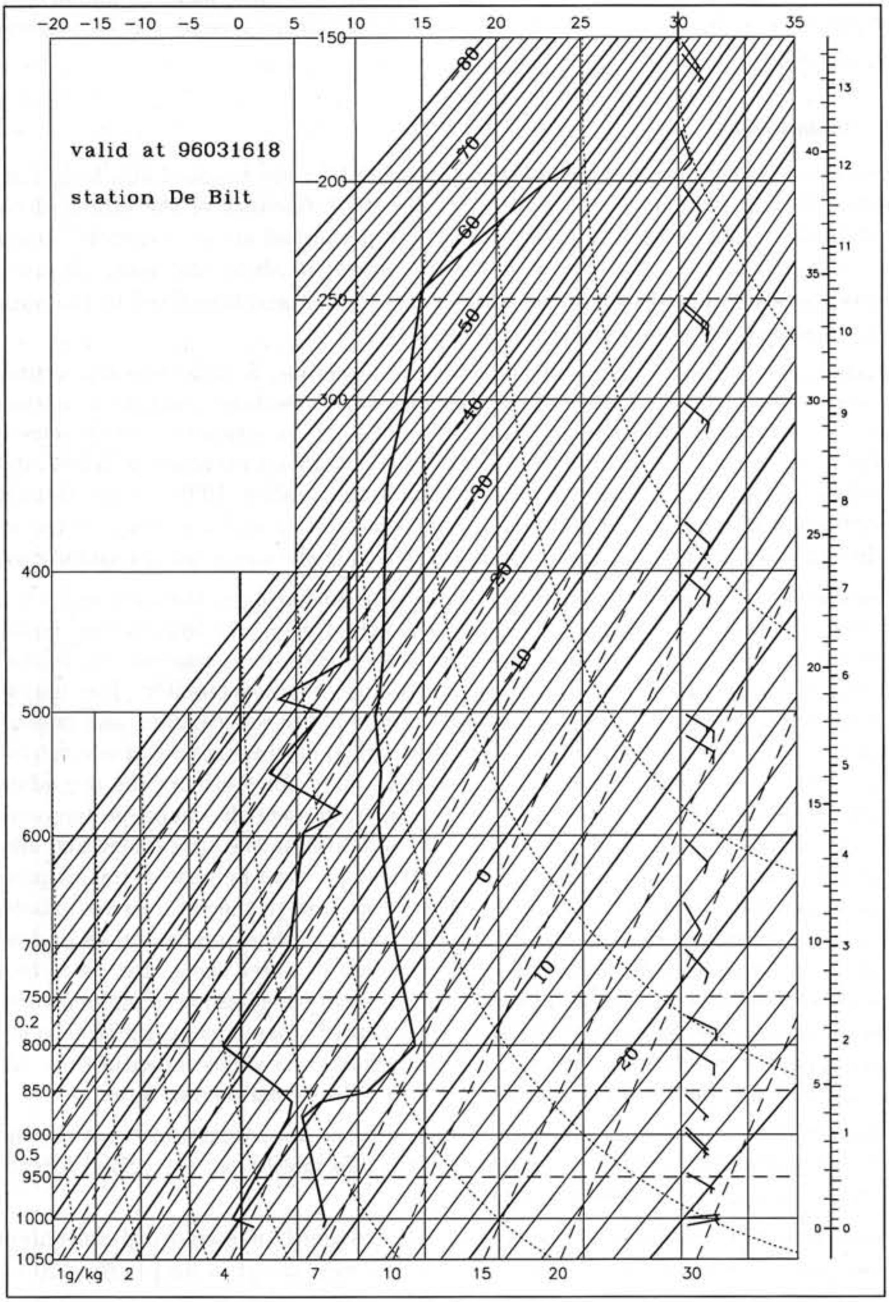

Figure 4.1 *Example of a radiosonde profile for De Bilt, 16 March 1996, 18:00 UTC , interferogram gd4*

or 5 m/s. A short barb is 5 knots or 2.5 m/s. The accuracy of the wind speeds is 2–3 m/s (ECMWF, 1994; Stull, 1995)

The radiosonde observations used for this study were obtained from the stations *De Bilt* in the Netherlands, *Ukkel* in Belgium, and *Emden* in Germany. The location of the stations is shown in figure 3.1. Two sondes, before and after each SAR acquisition, were used from the De Bilt station, and one sonde (the closest to the SAR acquisition) from the Emden and Ukkel stations. In total eight radiosonde profiles were analyzed for every interferogram.

4.2.4 Synoptic observations

Synoptic observations are obtained by a large number of manned or automatically operating meteorological stations. The different categories of observations are listed in table 4.2, and discussed below.

Code	Quantity	Units
stn	station number	
jjjjmmdd	Date	
uumm	Time (UTC)	h, m
t	Temperature	0.1°C
u	Relative humidity	%
rh	Amount of precipitation during the last hour	mm
dr	Duration if the precipitation in the last hour	0.1 h
dd	Average wind direction in the last 10 minutes of the last hour	degrees
ff	Average wind speed in the last 10 minutes of the last hour	0.1 m/s
q	Radiation during the last hour	J cm^{-2}
ww	Present weather category	code
v	Horizontal visibility	m
p	Pressure at sea level	mbar
n	Total cloud cover	octa
nh	Cloud cover low and medium clouds	octa
n1–n4	Cloud cover layer 1–4	octa
c1–c4	Cloud type or genus layer 1–4	code
h1–h4	Estimated height cloud base layer 1–4	code

Table 4.2 *Observation parameters at the synoptic stations*

Synoptic weather observations are stored in UTC and are available every whole hour. Airports often provide additional observations every half hour. The synoptic temperature `t` is determined at a height of 1.5 m above the ground level, with an accuracy of 0.1°C, and at the observation time. Relative humidity `u` is measured with an accuracy of a few percents. Precipitation, `rh`, in mm/hr is collected in the hour prior to reporting. Synoptic wind speeds `ff` and directions `dd` are measured at a height of 10 m above ground level. The reported wind speeds are mean values during 10 minutes of measurement. Wind speed accuracies are 3–4 m/s for surface stations (ECMWF, 1994; Stull, 1995). Table 4.3 lists the conversion between the Beaufort scale and its equivalent wind speed at a height of 10 m (McIlveen, 1995). The amount of solar radiation, `q`, can be interpreted as an

Beaufort	0	1	2	3	4	5	6	7	8	9	10	11
m/s	0	0.8	2.4	4.3	6.7	9.3	12.3	15.5	18.9	22.6	26.4	30.5

Table 4.3 *Conversion between the first 12 Beaufort wind forces and the equivalent mean wind speed at 10 m above the ground*

indirect measure of cloud cover. High radiation values mean that there is no cloud cover, low values imply thick cloud cover.

The weather code system—the `ww` observations in table 4.2—is a comprehensive range of codes to describe the particular behavior of the weather during the last hour or at observation time. It includes different degrees of haze and fog, development measures for clouds, types and patterns of precipitation, visibility measures, thunderstorm types, and different types of special weather phenomena. A list of weather codes can be found in, e.g., McIlveen (1995).

Pressure, `p`, is measured in mbar, currently often listed in hPa, and is measured with an accuracy of 0.1 mbar (ECMWF, 1994). Cloud cover, `n`, is defined as the fraction of the sky that is covered by clouds. It is estimated in fractions from 0/8 to 8/8, or *octa*, for the total cover and—if possible—for up to four height levels, `n1`–`n4`. The type of cloud cover, denoted by `c1`–`c4`, is a code for one of the 10 *genera*, see table 4.4, and is reported for every observed level of coverage. Furthermore, the height of each layer is estimated and reported, `h1`–`h4`.

Code	Genus	Level	Features
St	Stratus	Low	Low, spatially extensive sheet of cloud
Sc	Stratocumulus	Low	Low, broken into cumuliform masses
Cu	Cumulus	Low	Detached, hill shaped, flat base
Cb	Cumulonimbus	Low	Large cumulus, usually with showers. Large vertical extent
As	Altostratus	Medium	Extensive sheet, featureless
Ac	Altocumulus	Medium	Shallow sheet, broken into patches or rolls
Ns	Nimbostratus	Medium	Extensive sheet, usually precipitating
Ci	Cirrus	High	Detached, white fibrous clouds
Cc	Cirrocumulus	High	Shallow patch or sheet, broken into blobs or ripples
Cs	Cirrostratus	High	Shallow extensive sheet, transparent

Table 4.4 *Cloud classification in 10 genera, after McIlveen (1995). Low level clouds are at heights between 0–2 km above sea level, medium level at 2–7 km, and high level at 5–14 km, for temperate regions.*

The number of synoptic stations used in the analysis of the SAR interferograms vary according to the size of the interferogram area and the availability of the data. For all available stations, observations are used on the hours before and after each SAR acquisition. Cloud observations and weather codes are only available at the manned meteorological stations, mostly at airfields. These are listed in the interferogram analyses in chapter 5.

Based on the wind direction and velocity measured at the stations, interpolated surface wind fields are plotted to enable a comparison with the interferograms. Furthermore interpolated pressure and temperature fields are calculated. If these plots significantly enhance the interpretation of a specific interferogram, they are included in the analysis in chapter 5.

4.2.5 Weather charts

Weather charts, as provided by national and international meteorological services, are a combination of observations from different sensors and their meteorological situation. The weather charts used in this study are daily overviews of the weather over Europe at 12:00 UTC. They mainly show the location of high and low pressure regions and the isobars. Frontal systems are drawn over this plot. Selected surface observations of the main synoptic stations in the region are included, giving information on the temperature, wind speed and direction, total cloud cover, and precipitation. Five selected stations in the Netherlands are listed, with average values for the whole day for windspeed, temperature at two height levels, water vapor pressure, relative humidity, and pressure. Furthermore total values for the amount and duration of precipitation, and the duration of sunshine during the day. Although the information obtained from these charts is limited, it can give a rough estimation on the type and dynamics of the weather during that day. The plots are not shown during the interpretation of the interferograms in chapter 5 for the sake of conciseness.

4.3 Meteorological models

Weather analysis is the operational procedure for characterizing the spatial structure of the atmosphere at a specific time or epoch (Bevis et al., 1996). Initial state analyses are produced twice daily by most operational analysis centers, and are assimilated in a numerical weather model to produce weather forecasts. In Europe, the ECMWF[2] applies a model with a horizontal resolution of about 60 km, and 31 vertical layers. Meteorological variables are computed every 15 minutes (Stull, 1995). In the Netherlands the HIgh Resolution Limited Area Model (HIRLAM) is used. Resolutions are 55 to 5 km horizontally with 16 to 31 vertical layers. The Netherlands' implementation of the HIRLAM model applies a 3-hourly variational data assimilation scheme, using a cut-off time of 2h50 after the initialization time. The boundary values for the HIRLAM domain are taken from the ECMWF model output.

Since the model data described above lack in spatial resolution for the purpose of SAR interferometry, they were not used in the interferogram analyses. The specific disturbances in the interferograms are often of a smaller spatial extent. Moreover, these types of disturbances mostly apply on smaller time scales than the 3 hour averages in a model such as HIRLAM.

Just as the daily weather charts, model data can be used to get an overview of the meteorological conditions during the SAR acquisitions. This enables one to get likelihood estimates for specific types of disturbance. The readily availability of model data makes this type of information convenient for the analysis of larger regions, e.g., to select suitable

---

[2] European Center for Medium-Range Weather Forecasts

interferometric pairs from a database of SAR imagery.

4.4 Meteorological codes

Meteorological codes are used to facilitate quick information exchange with a format which enables automatic data processing. They are defined by the World Meteorological Organization in WMO Manual No. 306. The codes are composed of a set of code forms and binary codes made up of groups of letters representing meteorological or other geophysical elements. Different code forms are used to represent different types of observations or products. In messages, these groups of letters are transcribed into figures indicating the value of state of the elements described (Darling and Mongeon, 1996).

Chapter 5

Analysis and interpretation

Here, the set of interferograms is analyzed using all available meteorological information. It first describes the used methodology, and lists the main characteristics of the interferograms. Hereafter, the interferograms are analyzed by observing the possible atmospheric effects, interpreting these observations using suitable meteorological information, and providing concluding remarks per situation. The chapter concludes with a discussion of the analyses, in which the results are merged and classified.

key words: methodology, analysis, interpretation, classification

5.1 Analysis techniques

Although each computed interferogram should in fact be analyzed in a way optimized for the particular situation, a more or less standardized approach was chosen here to facilitate overall comparison and conclusions on the magnitude and type of recurrent effects. This results in a specific setting for each interferogram. Nevertheless, when phenomena are observed who deserve any special attention, also different analysis techniques were applied.

The interferograms are categorized according to their location into four groups: Groningen descending, Flevoland ascending, Flevoland descending, and Delft descending. Within each group, the interferograms are ordered chronologically. After a brief summary of the technical characteristics of the interferogram, three subsections list the specific interferometric *observations*, the *interpretation* of the observations using meteorological information, and the *conclusions* on the atmospheric signatures in the interferogram.

For every interferogram the relative and absolute phase are shown in the observation section, corresponding with the wrapped and unwrapped interferograms. The original, wrapped, interferogram has a phase fixed between $-\pi$ and $+\pi$, which enables a quick impression of the complexity of the phase variations. The phase scale of the unwrapped interferogram increases with the number of fringes, and is unique for every interferogram. If necessary, phase variations induced by topography are extracted using a reference DEM, which produces the differential interferogram. For the areas with few topography, combined with small perpendicular baselines, the original interferogram can be regarded as a differential interferogram. It is assumed that the only remaining interferometric phase variations are caused by horizontal spatial variations in the path delay.

A statistical analysis of the phase is then performed using a histogram, which also yields a rms value. There are two important consequences of this approach. First, obviously, the phase can only be analyzed over sufficiently coherent areas, e.g., excluding the water parts formed by the North Sea and IJsselmeer. Therefore, if necessary, in the histogram analysis several patches were selected who jointly contribute to the histogram. Since every patch has its own distribution, with a mean which can be different from other patches, the total histogram is sometimes composed of more than one more or less Gaussian distribution. Secondly, because the total surface of the selected patches is different for every interferogram, it is hard to use, e.g., the derived rms value as representative for the atmospheric phase variation. The combined interferograms of the Flevoland-ascending passes will therefore have larger rms values than the single-interferograms of Groningen. However, it is tried to use the same area of analysis per location, and therefore the results per location are comparable.

The standard observations conclude with the plot of a rotationally averaged spectrum of the largest possible rectangle in the interferogram. Plotting this spectrum on a log-log scale enables the comparison of the spectral frequencies with the $-5/3$ power law lines, commonly associated with turbulence in Kolmogorov theory. For the theoretical background of this evaluation, see section 2.4.5. The plots are shown to test the method to identify turbulent regions, and to discriminate different types of atmospheric signature in the SAR interferograms.

Following the observations, the data for each interferogram are interpreted, using all information available. The meteorological data sources are described in section 4.2. Since the amount of data used for each interpretation is too large to be fully printed in this report, only some derived and condensed plots, tables, or graphs are shown in the interpretations. For some of the interferograms, first hypotheses are given at the start of the interpretation, based on the interferogram only, or in combination with the daily weather charts.

Finally, conclusions are derived for every interferometric situation. The most probable cause or hypothesis for the observed differential phase variation is described, based on the available information. Some statistical information is summarized.

5.2 Analysis Groningen descending

The interferograms labeled as *Groningen descending* (gd) and their adjacent track (gdex) are situated in the northeast of the Netherlands, covering the Dutch provinces Groningen, Friesland, and Drenthe, and a part of Germany in the east. Just off shore, the *Frisian islands* mark the boundary between the *Wadden Sea* and the *North Sea.* The Wadden Sea is a tidal area with flats and channels. Depending on the tide during the SAR acquisitions, the tidal flats are either dry or flooded. Acquisitions during ebb tide are sometimes well correlated, providing an extended area of useful interferometric phase observations.

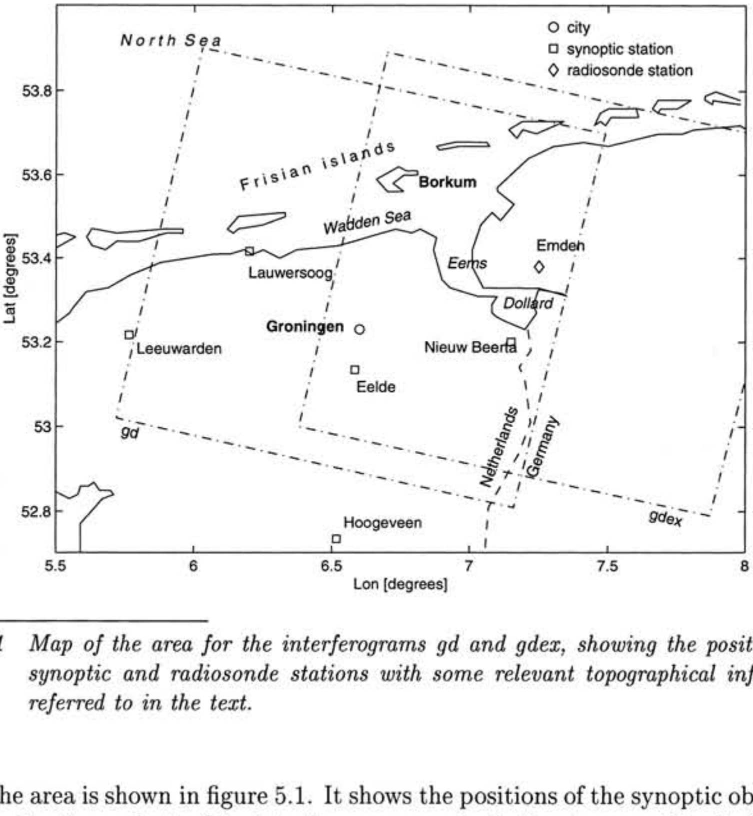

Figure 5.1 *Map of the area for the interferograms gd and gdex, showing the position of the synoptic and radiosonde stations with some relevant topographical information, referred to in the text.*

A map of the area is shown in figure 5.1. It shows the positions of the synoptic observation stations used in the analysis of the interferograms, and all other topographical information referred to in the following text. Both the stations *Eelde* and *Leeuwarden* are air fields, i.e., manned stations providing a full range of meteorological observations, including cloud types, heights, levels and coverage. The city of Groningen is shown nearly in the center of the map. Apart from the Dutch islands (Ameland and Schiermonnikoog) at the western side of the area, the first German island Borkum is labeled in the map. The Eems-Dollard estuary divides the northern parts of Germany and the Netherlands. Radiosonde observations are available from the meteorological station Emden.

The area can be considered flat for the interferometric interpretation, varying between −2 and +3 meters for the majority of the land surface. A small ridge covers the southern part of interferogram *gd*, with a maximal height of 20 m. Even for the longest baseline, these elevations are not significantly observable in the interferograms. Therefore, all interferograms of the area can be considered *differential* interferograms, i.e., a *flat* elevation model is subtracted.

Interferogram *gdex* is a single SAR pair from an adjacent track. Synoptic observations in this area are limited, therefore mostly satellite observations, radiosondes and larger scale weather charts are used for the analysis.

5.2.1 Analysis of interferogram gd1

Interferogram gd1 was acquired at July 15 and 16, 1995, at 10:31:58 UTC (12:31:58 LT). SAR frame number 2529. ERS-1 orbit 20909, ERS-2 orbit 1236. The parallel baseline was 3 m, the perpendicular baseline −27 m. Phase unwrapping was performed using the minimal cost flow algorithm (Costantini, 1996).

5.2.1.1 Observations

The interferogram in figure 5.2 is exceptionally disturbed, especially in the lower right corner. After unwrapping, see figure 5.3, more than 4.5 cycles difference in interferometric phase can be observed, mainly in the form of isolated anomalies with a diameter of 5–10 km. The section within the square in the unwrapped interferogram was analyzed using a histogram, see figure 5.4 and a rotational averaged spectrum, see figure 5.5. This spectrum shows a −5/3 power law in wavelengths between 1 and 25 km. The rms in this area is 3.4 rad.

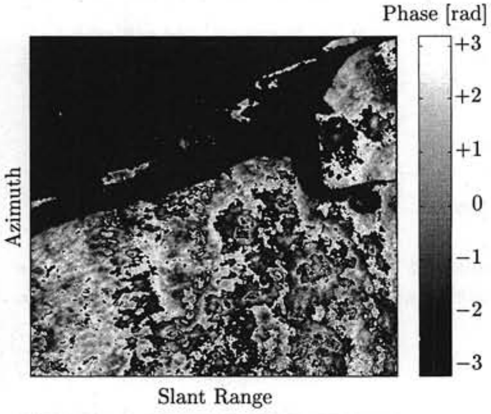

Figure 5.2 *Interferogram gd1*

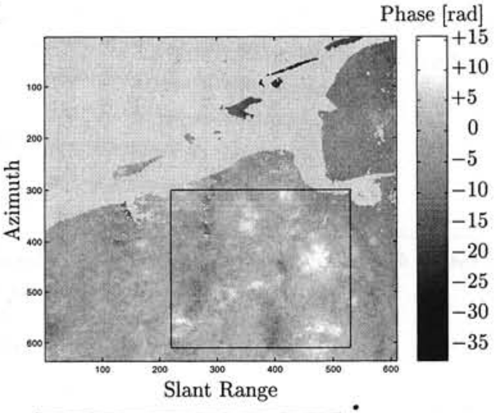

Figure 5.3 *Unwrapped interferogram gd1*

5.2.1.2 Interpretation

The main signatures of the interferogram are strong isolated cells and more or less elongated structures in azimuth direction. Due to the amount of phase delay, the hypothesis for the driving mechanism is that this is caused by a thunderstorm. This could cause local differences in humidity, pressure and temperature, which locally increases refractivity.[1]

The weather radar at day 1, figure 5.6, shows isolated showers at the locations of the negative values in absolute phase. The soundings of both days at Emden reveal instability

---

[1] During a thunderstorm passage, pressure changes up to 4 mbar per 10 minutes have been observed!

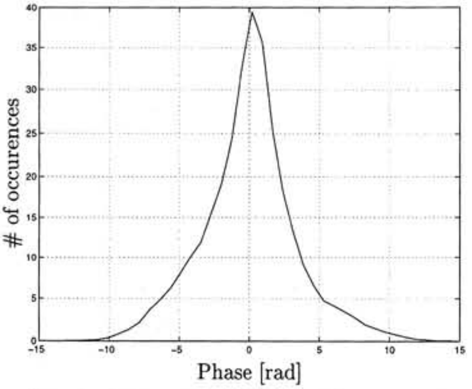

Figure 5.4 *Histogram of selected part of interferogram gd1*

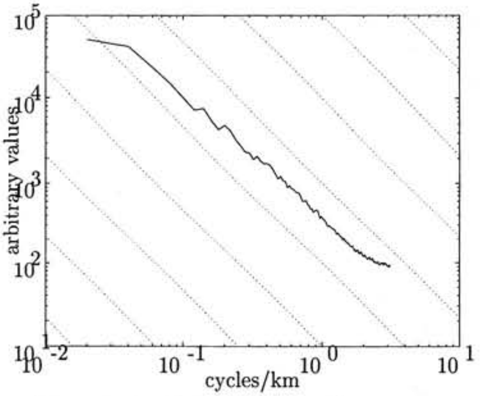

Figure 5.5 *Rotational average spectrum of interferogram gd1*

around the time of launch and ascent (launch at 11:00 UTC). They show low relative humidity at higher levels. Relative humidities at surface level at the time of SAR acquisition are 75–96%. Some isolated showers are building up around the time of the SAR acquisition. In the upper right corner of the overall weather radar image showers are reaching a height of about 6 km. These are cumulonimbus clouds. Note that at this distance from the radar, the lower part (1 km) of the rainfall is obscured due to the Earth's curvature. There is a shower over the island Borkum, in the north-eastern part of the image. Relative humidities are 75–96%. The wind direction was around 200 degrees (SSW). This corresponds with the the orientation of the negative phase values in the interferogram.

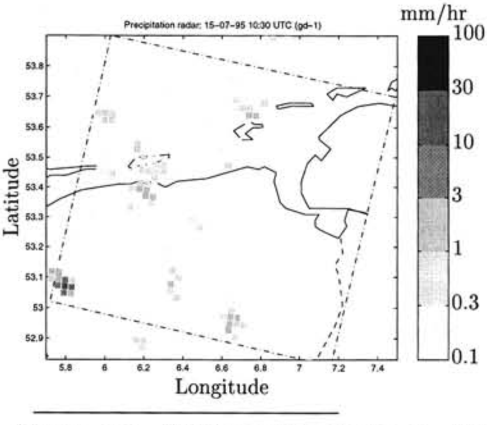

Figure 5.6 *Weather radar of day 1, 10:30 UTC*

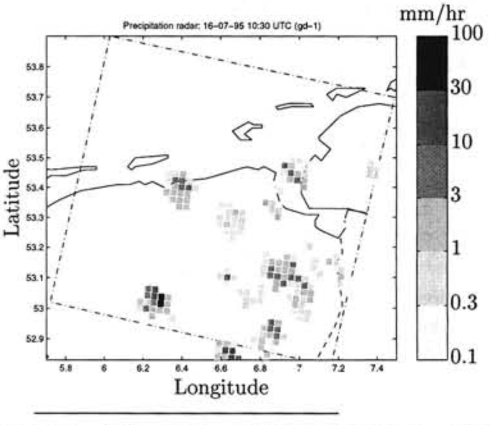

Figure 5.7 *Weather radar of day 2, 10:30 UTC*

At day 2, the high resolution VIS-channel of Meteosat shows a line of showers over the east of the Netherlands, just as the AVHRR: an organized pattern of showers, caused by a trough passage. The weather radar shows this line of showers as well, cf. figure 5.7. Here the locations of the showers are identical to the locations of the high positive absolute phase values in the interferogram. The showers reach a height of approximately 8 km.

The synoptic data show cumulonimbus with cloud base at 700 meters. Relative humidities at surface level are 72–82%, wind direction 240–250 degrees (SW).

Surface temperatures were 20°C at both days. A southwesterly flow of polar air, which became unstable due to heating up the surface, caused the thunderstorms.

The comparison of the unwrapped interferogram and the weather radar image suggests a strong correlation between the almost north-south band of showers over Groningen and the elongated structures in the interferogram.

Station	#	UTC	Day	Level 1	Level 2
Leeuwarden	270	1000	1	4/8, Cu, 700 m	4/8, Sc, 1600 m
Eelde	280	1000	1	3/8, Cu, 650 m	5/8, Ac, 3000 m
Leeuwarden	270	1100	1	7/8, Cu, 700 m	
Eelde	280	1100	1	3/8, Cu, 650 m	
Leeuwarden	270	1000	2	2/8, Cu, 650 m	
Eelde	280	1000	2	2/8, Cb, 700 m	3/8, Cu, 800 m
Leeuwarden	270	1100	2	2/8, Cu, 650 m	
Eelde	280	1100	2	2/8, Cb, 700 m	3/8, Cu, 800 m

Table 5.1 *Cloud observations gd1: 15-07/16-07-1995. The observations give the amount of cloud cover (okta), the type of cloud, and the cloud base at 2 levels.*

The cloud observations in table5.1 consist mainly of cumulus and cumulonimbus clouds. At the first day, in the morning also some higher clouds were observed.

5.2.1.3 Conclusion

Two thunderstorms, active during both SAR acquisitions, are responsible for these phase delays. The position of the rain fields detected by the weather radar coincide very well with the phase inhomogeneities. Therefore the weather radar observations can be used to predict the phase inhomogeneities in the interferogram, up to the sign difference between the two SAR acquisitions.

5.2.2 Analysis of interferogram gd2

Interferogram gd2 was acquired at August 19 and 20, 1995, at 10:31:58 UTC (12:31:58 LT). SAR frame number 2529. ERS-1 orbit 21410, ERS-2 orbit 1737. The parallel baseline was 37 m, the perpendicular baseline −81 m. Phase unwrapping was performed using the minimal cost flow algorithm (Costantini, 1996).

5.2.2.1 Observations

The interferogram figure 5.9 is relatively clean, although a "trough" can be seen at the right hand side of the image. The phase variations are spatially small, and can be characterized as "strings of pearls": lineated and frayed features which vary regularly in wideness. The directions of the strings are approximately 16 and 65 degrees. The observed structures become somewhat larger in diameter when farther from the coast. Figure 5.8 is the result of the phase unwrapping. Some of the Frisian islands still have a 2π phase shift with respect to the others, caused by the loss of coherent phase continuity over water areas. Figure 5.10 is the histogram over a representative part of the image. The rms value is 1.5 rad. Figure 5.11 shows the rotationally averaged spectrum. The $-5/3$ power law is roughly followed in the ranges between 0.3–1 km, and between 10–25 km.

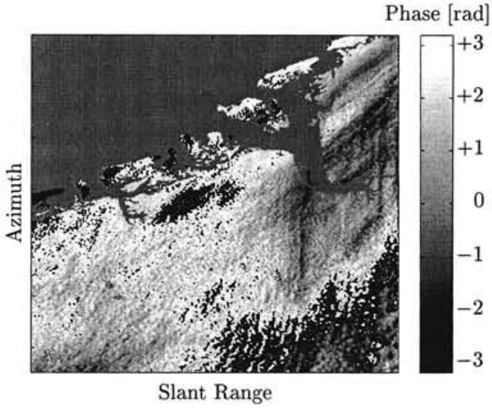

Figure 5.8 *Interferogram gd2*

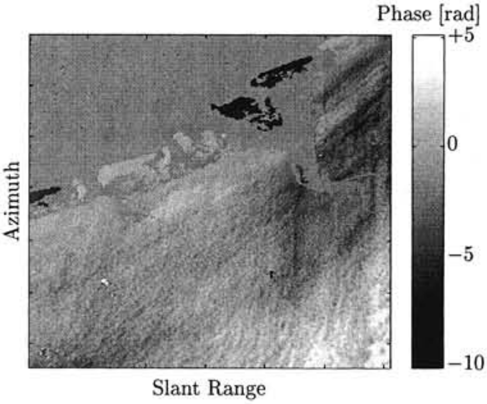

Figure 5.9 *Absolute interferogram gd2*

5.2.2.2 Interpretation

From the radiosondes, station Emden, it follows that day 1 and 2 are both very dry. However, there is some cloud cover on day 2 at low levels. The synoptic data showed that it was very warm both days (above 23°C). In Nieuw Beerta it was 29°C at 11:00 UTC. There was almost no cloud cover, at day 1 only a little cirrus (1/8) at 7 km, which can be neglected. At day 2 there may have been some low clouds in the western part of the test site (station Leeuwarden): 3/8 cumulus at 500 m. On day 1 a weak wind blew east to north-east (090-060) while on day 2 it turned to north, north-northeast (350 - 040). These directions correspond roughly with the directions observed in the interferogram.

The radiosonde data (day 1) confirms a strong subsidence inversion at 2200 m. At high levels in the troposphere it is rather dry. There is a change in wind direction of 60–70 degrees just below and above the inversion. The highest relative humidity is found at the inversion base, where it reaches 73%.

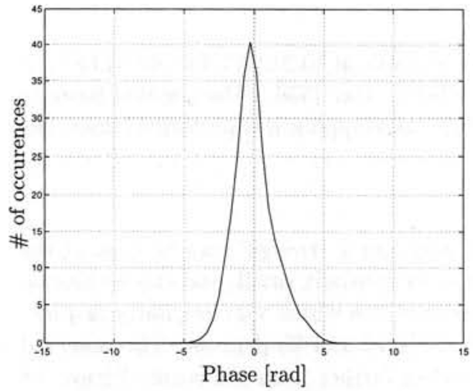

Figure 5.10 *Histogram interferometric phase interferogram gd2*

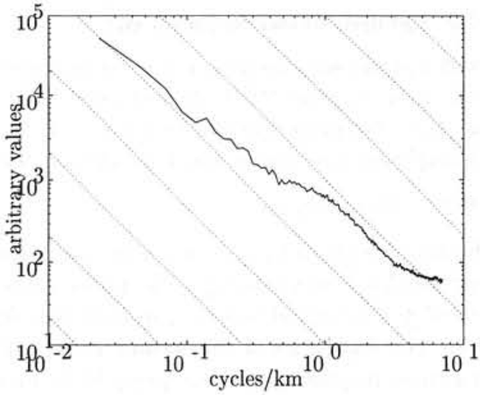

Figure 5.11 *Rotationally averaged spectrum interferogram gd2*

The weather radar did not show any rain in the test area. However, at 10:15 UTC, it still showed some signal east of the Dollard, due to a surface inversion. This is in fact an artifact of the rain detection capabilities of the precipitation radar.

AVHRR showed no clouds at day 1, and some vague cirrus at day 2. Also the Meteosat IR channel did not reveal anything in our test area.

The synoptic data revealed a north-eastern wind at day 1 and more northern winds at day 2. This seems to correlate with the directions in the interferogram. There is not much spatial variation in the relative humidity.

Looking forward in time to day 3 we see that moisture is transported into the area by the wind turning from east/ north-east to north. This probably correlates with the general appearance of the interferogram in which the coastal area seems invaded by humidity.

Station	#	UTC	Day	Level 1	Level 2
Leeuwarden	270	1000	1		
Eelde	280	1000	1		
Leeuwarden	270	1100	1		
Eelde	280	1100	1	1/8, Ci, 6600 m	
Leeuwarden	270	1000	2	1/8, Cu, 500 m	3/8, Ci, 8300 m
Eelde	280	1000	2	2/8, Ci, 8300 m	
Leeuwarden	270	1100	2	4/8, Ci, 8300 m	
Eelde	280	1100	2	2/8, Ci, 8300 m	

Table 5.2 *Cloud observations gd2: 19-08/20-08-1995. The observations give the amount of cloud cover (okta), the type of cloud, and the cloud base at 2 levels.*

5.2.2.3 Conclusions

Phase variation is small over most of the area. Since the observed directions correspond with the prevailing winds, it is expected to be caused by transport of moisture from the north. The distribution and size of the phase disturbances indicate a transition from more laminar flow in the north to more turbulent flow in the south of the area.

5.2.3 Analysis of interferogram gd3

Interferogram gd3 was acquired at December 2 and 3, 1995, at 10:31:56 UTC (11:31:56 LT). SAR frame number 2529. ERS-1 orbit 22913, ERS-2 orbit 3240. The parallel baseline was 17 m, the perpendicular baseline 44 m. Phase unwrapping was performed using the minimal cost flow algorithm (Costantini, 1996). The ERS-1 SAR had 128 missing azimuth lines.

5.2.3.1 Observations

The interferogram figure 5.13 has a striking "wave-like" feature in the lower left side of the image. The remaining parts are relatively clean. The horizontal line in the middle of the image is an artifact, possibly caused by incorrect treating of a number of missing lines in the original SAR data. Figure 5.12 results from phase unwrapping. Figure 5.14 is the histogram over a representative part of the image. The superposition of three Gaussian curves is probably caused by the sine-wave in the lower left of the image. Figure 5.15 is the rotationally averaged spectrum, following the −5/3 curve between 3 and 40 km wavelengths.

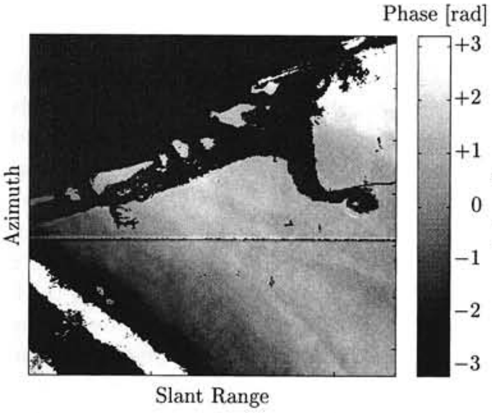

Figure 5.12 *Interferogram gd3*

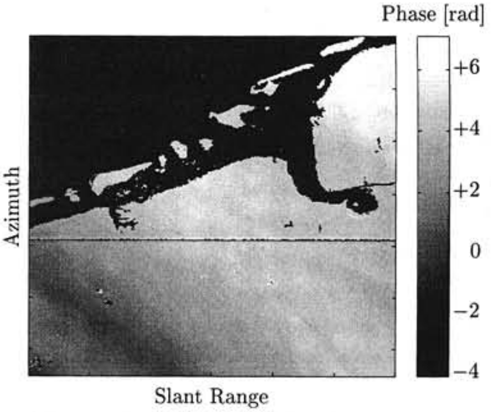

Figure 5.13 *Unwrapped interferogram gd3*

5.2.3.2 Interpretation

The most prominent feature in this interferogram is visible in the lower left corner of the scene. We have labeled this feature the "dog ear". There is a possibility that this a processor artifact, however, SAR processing with an independent SAR processor (DLR-BSAR) yielded the same error (Schättler, 1997). Different tests with other approximations of the reference phase, and using independent precise orbits (DEOS) did not eliminate the effect either. The remaining part of the interferogram seems to have few phase variations.

Since the "dog ear" has a negative sign, the cause of the effect is expected in the second SAR acquisition, at December 3. Both AVHRR and Meteosat (figure 5.16) show at this day low cloud structures in the same direction as the dog ear. According to the cloud observations 5.3 the cloud type is stratocumulus.

The weather radar shows nothing at all: no rain. From Meteosat we learn that at day 1 there was a "frontal" zone that is being pushed back at day 2. Above the Netherlands

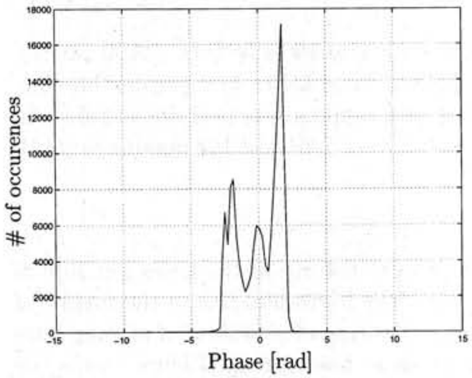

Figure 5.14 *Histogram of major part of interferogram gd3*

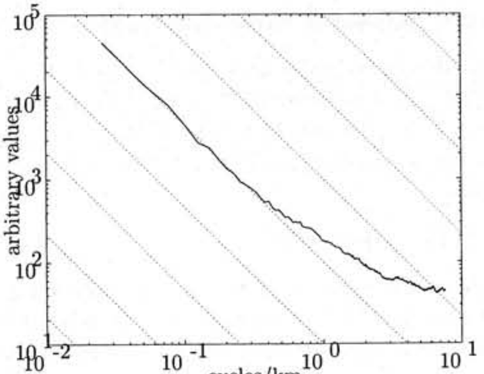

Figure 5.15 *Rotationally averaged spectrum of interferogram gd3*

there are several quasi-stationary fronts: at the boundary between warm air in SW-part and cold air in NE-part of the Netherlands.

The synoptic data show that it was cold, around the freezing level. There is a high relative humidity, therefore the air is very moist, especially in the SW-part in low levels (0–1000m) almost 100% RH. All stations in the test area report misty weather: reduced visibility between 2.5–3.7 km. At day 1 it was totally clouded. There was stratocumulus with base at 400 m. The radiosonde of De Bilt (day 1) shows very dense cloud layer between 50–1000 m. In the SW-part of the observed area part of this low cloudiness can be present at day 1. Note that NOAAs AVHRR does not see this, since it is hidden under cirrus clouds, with tops above 8 km. Also, the amount of solar flux is low, indicating thick cloud cover. At day 2 the solar flux is higher, which indicates less thick cloud cover. The solar flux is, however, more variable over the area, which indicates inhomogeneities in the cloud thickness.Synops-station Eelde, reports 2/8 cumulus at about 400 m with holes in the cover. The wind at both days was ESE (90-100 degrees).

Station	#	UTC	Day	Level 1	Level 2	Level 3
Leeuwarden	270	1000	1	2/8, St, 200 m	8/8, St, 300 m	
Eelde	280	1000	1	3/8, St, 150 m	5/8, St, 200 m	8/8, St, 300 m
Leeuwarden	270	1100	1	1/8, St, 200 m	8/8, St, 300 m	
Eelde	280	1100	1	3/8, St, 100 m	5/8, St, 200 m	8/8, St, 250 m
Leeuwarden	270	1000	2	3/8, Sc, 500 m	8/8, Sc, 600 m	
Eelde	280	1000	2	5/8, Sc, 350 m		
Leeuwarden	270	1100	2	2/8, Sc, 650 m	8/8, Sc, 800 m	
Eelde	280	1100	2	3/8, Cu, 400 m		

Table 5.3 *Cloud observations gd3: 02-12/03-12-1995. The observations give the amount of cloud cover (okta), the type of cloud, and the cloud base at 3 levels.*

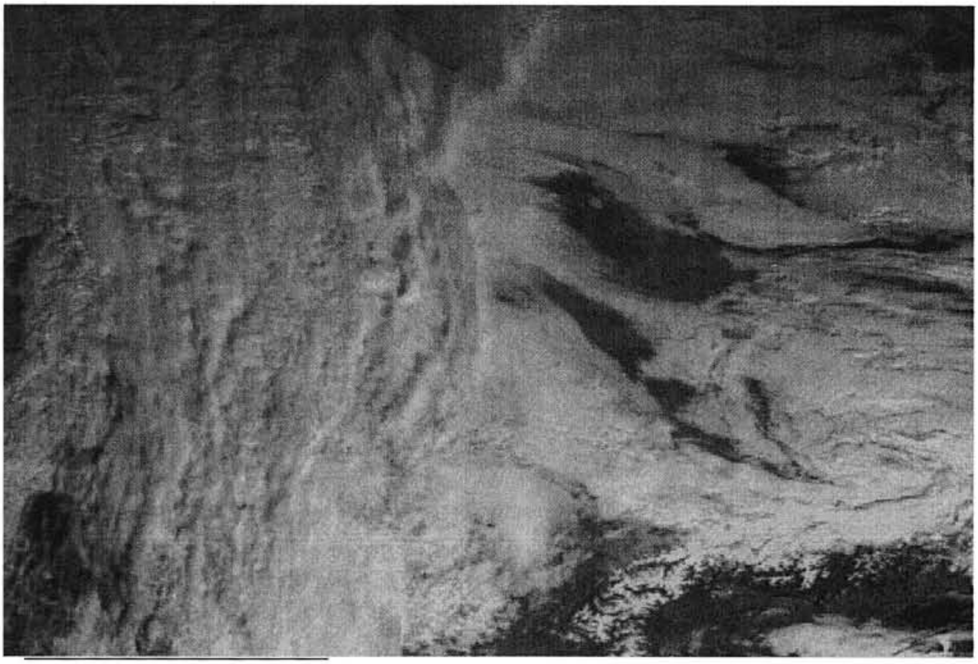

Figure 5.16 *Visual image Meteosat, 03-12-95, 10:30 UTC, gd3. The Netherlands are located in the center of the image. Refer to figure 5.139 at page 113 for orientation.*

5.2.3.3 Conclusions

Since the "dog ear" has a negative sign, localized delay changes at the second acquisition cause this effect. The combination of the satellite observations from Meteosat and NOAA with the manual cloud observations and radiation flux measurements show a non-uniform cloud cover. The effect is therefore probably caused by a localized cloud band in northwest–southeast direction.

5.2.4 Analysis of interferogram gd4

Interferogram gd4 was acquired at March 16 and 17, 1996, at 10:31:46 UTC (11:31:46 LT). SAR frame number 2529. ERS-1 orbit 24416, ERS-2 orbit 4743. The parallel baseline was 16 m, the perpendicular baseline −18 m. Phase unwrapping was performed using the minimal cost flow algorithm (Costantini, 1996).

5.2.4.1 Observations

The interferogram (figure 5.17) exhibits many small waves in varying directions. The unwrapped interferogram, the absolute phase, is shown in figure 5.18. Two parts of the absolute phase are extracted from this image, and analyzed using the Radon transform (figures 5.19 and 5.20). Part A is the large square, part B the smaller one. From these transforms, the dominant directions of 41 and 45 degrees, counterclockwise from the positive azimuth axis, can be found for part A and B respectively. Wavelengths are 2.4 and 3.5 km respectively. The waves in part A have an amplitude of less than 0.7 rad, in part B less than 1 rad. A 3D visualization of part B is given in figure 5.21.

Figure 5.22 is the histogram over a representative part of the image. It shows that phase variation is very little, with an rms of 0.6 rad. Figure 5.23 is the rotationally averaged spectrum. The −5/3 line is only followed in the longer wavelengths: 12–45 km. Clearly, the wave patterns in the interferogram cannot be considered isotropic, which is one of the assumptions in Kolmogorov turbulence theory (Tatarskii, 1971).

An extensive GPS campaign was performed during the period in which the SAR images were acquired, see Hanssen (1996); Stolk et al. (1997).

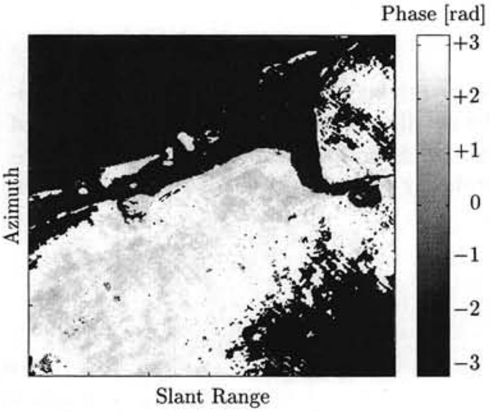

Figure 5.17 *Interferogram gd4*

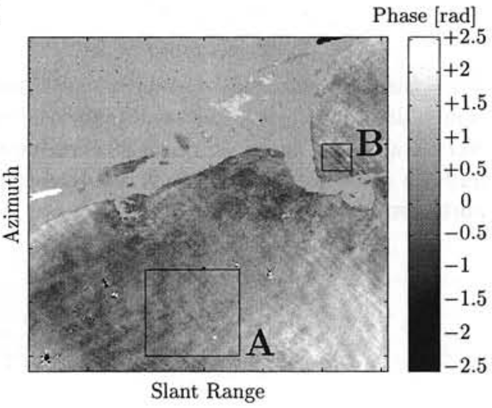

Figure 5.18 *Unwrapped interferogram gd4*

5.2.4.2 Interpretation

The main signal consists of waves with relatively short wavelengths, 3 km, in different directions. Hypotheses for these effects are: (1) cloud streets or gravity waves, (2) wave effects on top side of fog, or (3) a subsidence inversion.

The weather radar does not show anything at both days. The synoptic data indicate that it was cold, just above freezing level. There was no rain, it was misty with a visibility between 2.1 and 4 km. Both Leeuwarden and Eelde reported 8/8 cloud cover, with especially much

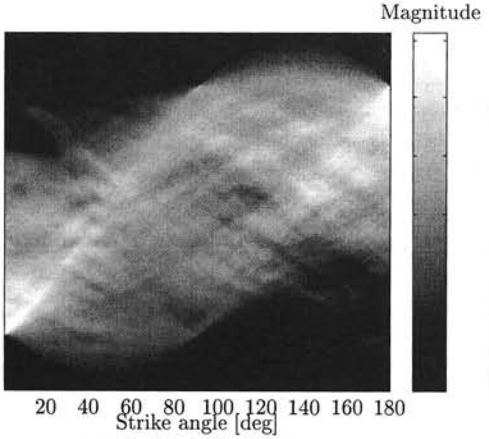

Figure 5.19 *The Radon transform of part A of the absolute interferogram*

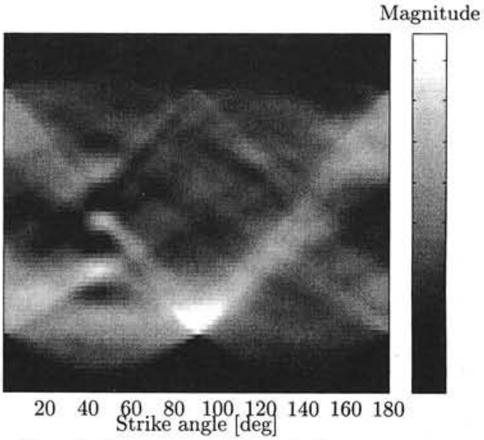

Figure 5.20 *The Radon transform of part B of the absolute interferogram*

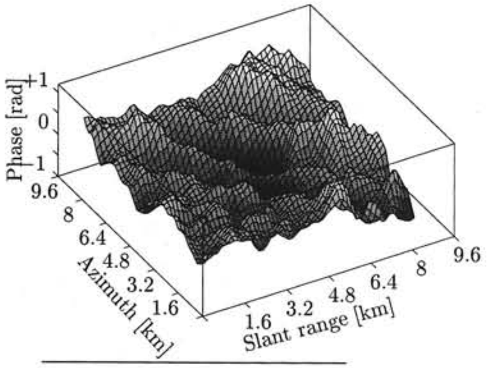

Figure 5.21 *A 3D view of the waves in part B of the absolute interferogram*

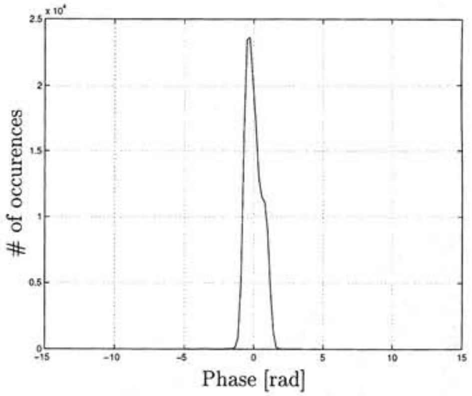

Figure 5.22 *Histogram of major part of interferogram gd4*

low-level clouds: 5/8 stratocumulus at 400 m in Leeuwarden and 6/8 stratus at 350 m in Eelde, see table 5.4. On both days the wind direction was east, with a wind force 4 at the first day. At day 2, Eelde reports 5/8 stratocumulus at 400–500 m, and Leeuwarden 5/8 stratocumulus at 3800 m. More layers are observed at day 2 than at day 1. Meteosat VIS reveals a closed cloud cover, with several layers. The IR image shows that the clouds at day 1 are not that high, while at day 2 there is also higher (colder) cloud cover. NOAA AVHRR observations of day 1 reveal very many cloud wave features in the area, in different directions. The directions observed in the interferogram are also just visible in the AVHRR imagery, although the resolution level needs to be tweaked.

At the surface the wind direction is east. Low stratocumulus cloud streets are oriented east-west. However, at higher altitudes the wind becomes more southern oriented. From the radiosonde data it is found that there can be cloud levels at different altitudes.

The atmosphere is unstable in the layer below 800 m on the first day and 1500 m on

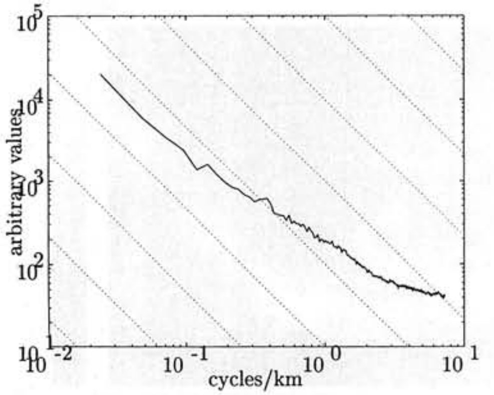

Figure 5.23 *Rotationally averaged spectrum of interferogram gd4*

day 2. Due to an inversion, it is stable above this height.

Station	#	UTC	Day	Level 1	Level 2
Leeuwarden	270	1000	1	8/8, Sc, 400 m	
Eelde	280	1000	1	8/8, St, 300 m	
Leeuwarden	270	1100	1	8/8, Sc, 400 m	
Eelde	280	1100	1	8/8, Sc, 400 m	
Leeuwarden	270	1000	2	7/8, Sc, 450 m	8/8, Sc, 1200 m
Eelde	280	1000	2	8/8, Sc, 400 m	
Leeuwarden	270	1100	2	7/8, Sc, 500 m	8/8, Sc, 1200 m
Eelde	280	1100	2	8/8, Sc, 400 m	

Table 5.4 *Cloud observations gd4: 16-03/17-03-1996. The observations give the amount of cloud cover (okta), the type of cloud, and the cloud base at 2 levels.*

5.2.4.3 Conclusions

The hypothesis of wave effects on the top side of the fog seems to be very unlikely, since there is not much wind at that altitude. Also there are no signs of a subsidence inversion from the radiosonde. Based on the observations of cloud bands in the AVHRR imagery, the phase fluctuations in the interferogram are very likely to be caused by anisotropic cloud distributions at several layers. Gravity waves at the inversion level is probably the driving mechanism for the observed waves in the interferogram.

5.2.5 Analysis of interferogram gd5

Interferogram gd5 was acquired at April 20 and 21, 1996, at 10:31:59 UTC (12:31:59 LT). SAR frame number 2529. ERS-1 orbit 24917, ERS-2 orbit 5244. The parallel baseline was 34 m, the perpendicular baseline −76 m. Phase unwrapping was performed using the minimal cost flow algorithm (Costantini, 1996).

5.2.5.1 Observations

The interferogram (figure 5.24) shows small undulations, within half a cycle, and a longer wavelength feature, causing just one fringe in the middle of the interferogram. Waves with a small wavelength (2–3 km) can be observed in the lower left and the upper right corner of the interferogram. Longer wavelength striated effects are visible just right of the middle of the interferogram (wavelengths 10–13 km). It seems that the waves become more turbulent towards the lower right part of the interferogram, where a honeycomb pattern can be observed The unwrapped interferogram, the absolute phase, is shown in figure 5.25. Figure 5.26 is the histogram over the main part of the image, showing two superposed Gaussians, due to the large curvature in the interferogram. Overall rms is 1.4 rad, although the two separate Gaussians have rms values of approximately 1 and 0.45 rad respectively. Figure 5.27 is the rotationally averaged spectrum. Wavelengths following the −5/3 power law include the 0.5–2 km range and the 10–45 km range.

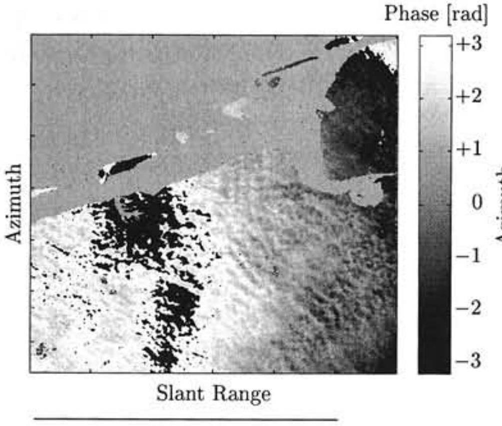

Figure 5.24 *Interferogram gd5*

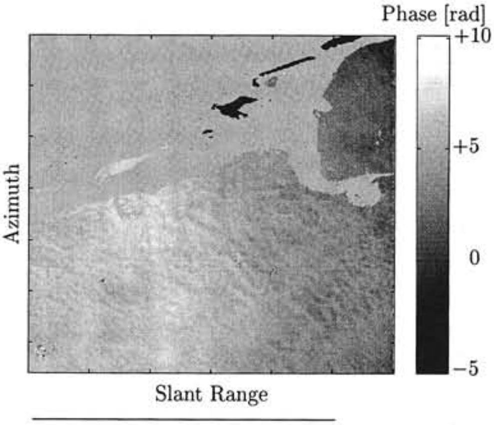

Figure 5.25 *Unwrapped interferogram gd5*

5.2.5.2 Interpretation

The weather radar indicates no rain at both days. AVHRR observations shows cirrus clouds at day 1. The Meteosat IR image shows some flaky structures at day 1, but almost no structure at day 2.

The synoptic data give a weather category 5 at day 1, which indicates haze. This is possibly due to solid particles. The relative humidity is 50–60%, which indicates very dry air! In the area 6/8 cirrus is reported at about 7–8 km. Eelde also reports some medium level clouds for day 1: 3/8 altocumulus at about 3.5 km. At day 2 there is also only a little cirrus cloud cover. Table 5.5 lists the cloud observations. The solar flux of 220 is very high (which indicates sunny weather), and the temperatures vary around 20°C.

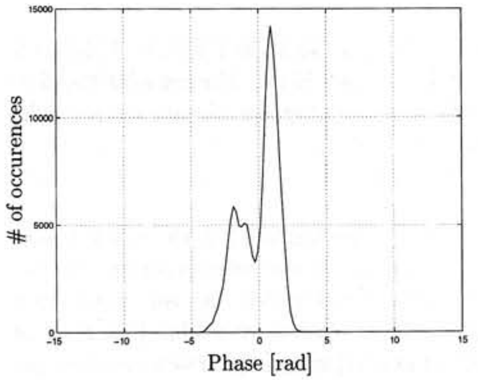

Figure 5.26 *Histogram of major part of interferogram gd5*

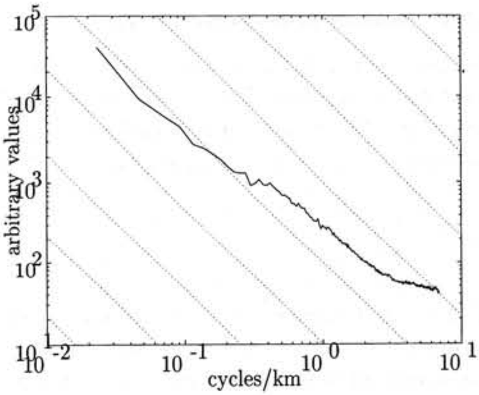

Figure 5.27 *Rotational averaged spectrum of interferogram gd5*

For the interferogram we would therefore also expect that there are not much variations in water vapor. The radiosonde data reveal no signs of an inversion at both days.

Surface wind directions were south-southeast at day 1, and more south to south-southwest at day 2. The structures in the interferogram are tending more towards the south-eastern direction. From the radiosondes, however, we find that wind is veering with height. At the height of the cirrus clouds, 8–9 km, the wind direction was both days more south-west, which is nearly perpendicular to the wave effects in the interferogram.

Station	#	UTC	Day	Level 1	Level 2
Leeuwarden	270	1000	1	6/8, Ci, 8300 m	
Eelde	280	1000	1	6/8, Ci, 8300 m	
Leeuwarden	270	1100	1	6/8, Ci, 8300 m	
Eelde	280	1100	1	1/8, Ac, 3300 m	7/8, Ci, 8300 m
Leeuwarden	270	1000	2	5/8, Ci, 8300 m	
Eelde	280	1000	2	3/8, Ci, 8300 m	
Leeuwarden	270	1100	2	5/8, Ci, 8300 m	
Eelde	280	1100	2	3/8, Ci, 8300 m	

Table 5.5 *Cloud observations gd5: 20-04/21-04-1996. The observations give the amount of cloud cover (okta), the type of cloud, and the cloud base at 2 levels.*

5.2.5.3 Conclusions

Evidence for the observed effects is poor for this situation. Based on the discrepancy between the surface winds and the direction of the waves in the interferogram, it is expected that the driving mechanism for these effects is at a higher altitude. Only the influence of cirrus clouds at day 1 could have a significant effect in the interferogram, since relative humidities were fairly constant with height. The perpendicular direction of the wind at the height of the cirrus clouds agrees with this hypothesis.

5.2.6 Analysis of interferogram gd6

Interferogram gd6 was acquired at May 25 and 26, 1996, at 10:31:50 UTC (12:31:50 LT). SAR frame number 2529. ERS-1 orbit 25418, ERS-2 orbit 5745. The parallel baseline was 52 m, the perpendicular baseline 99 m. Used phase unwrapping algorithm: minimal cost flow (Costantini, 1996). The SAR processing is subject to an error in the Sampling Window Start Time (SWST) shift. This causes the loss of coherence in the band in the upper right corner of the interferogram.

5.2.6.1 Observations

Interferogram gd6, shown in figure 5.28, exhibits atmospheric phase variation of up to 1 cycle. A clear direction is visible in the artifacts, from lower left to middle right. It seems that the striation is becoming more turbulent in the right part of the image, where they dissolve in more isolated cells. In the left part of the interferogram, more laminar flows are observed. The unwrapped interferogram, the absolute phase, is shown in figure 5.29. Figure 5.30 is the histogram over the main part of the image, with an rms value of 1.8 rad. Figure 5.31 is the rotationally averaged spectrum, showing a small band of $-5/3$ behavior between 0.4–1 km and 15–50 km wavelengths.

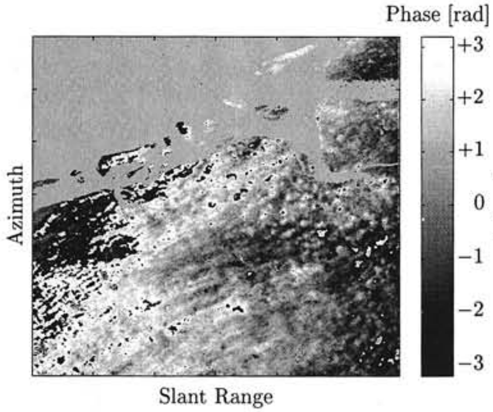

Figure 5.28 *Interferogram gd6*

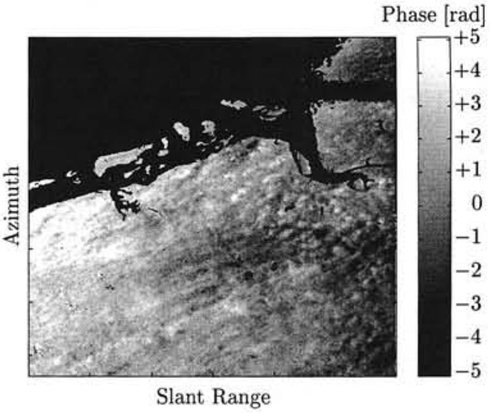

Figure 5.29 *Unwrapped interferogram gd6*

5.2.6.2 Interpretation

This interferogram is composed of the still rather humid air of day 1, after the passage of a front and rainfall, and the rather dry, but unstable air of the second day. The instabilities at the second day could be the cause of the phase disturbance in the interferogram.

From the weather charts we learn that at day 1 a cold front has just passed: there is polar air in the area. Some clouds are moving in the tail of this cold front, as we observe from the AVHRR data. From the precipitation radar we see that a vast field of rain is located in the south-east part of the Netherlands. It does not rain in the test area at the moment of the day 1 SAR acquisition.

The synoptic data show at day 1 for station Eelde: 5/8 cumulus at 500 m and 6/8 altocumulus at 4 km, see table 5.6. In total, 7/8 cloud cover is reported. For station Leeuwarden: 2/8 cumulus at 300 m, and 4/8 cumulus at 400 m. Station Hoogeveen

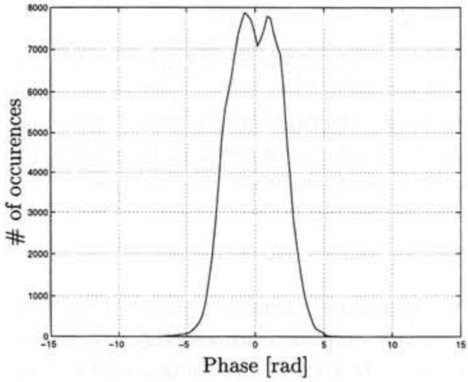

Figure 5.30 *Histogram of major part of interferogram gd6*

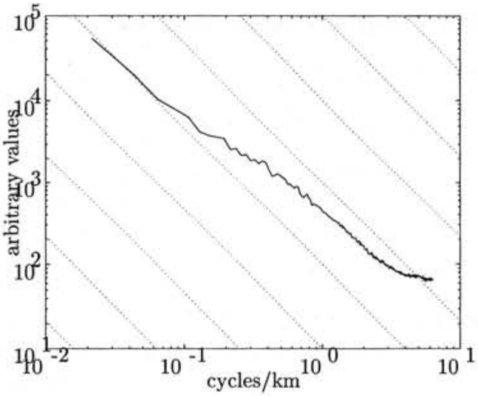

Figure 5.31 *Radial averaged spectrum of interferogram gd6*

(279) reported some precipitation (4 mm). The wind direction turns from west to west-southwest in the interferogram, see figure 5.32.

At day 2, the area is still in polar air. Station Eelde observes 2/8 cumulus at low altitude and 5/8 altocumulus at 3300 m. Leeuwarden denoted 2/8 cumulus at 800 m, and 4/8 altocumulus at 3 km. There is more sunshine on day 2 and a fair amount of wind from west-southwest,see figure 5.33.

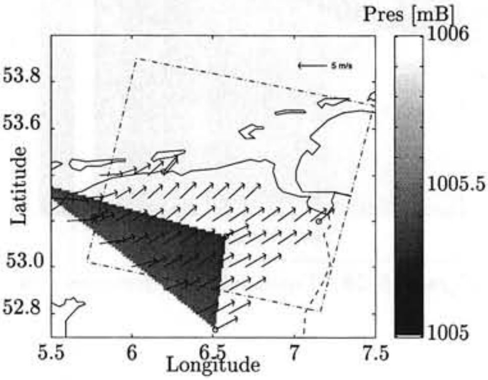

Figure 5.32 *Pressure and surface wind field gd6, day 1, 10:00 UTC*

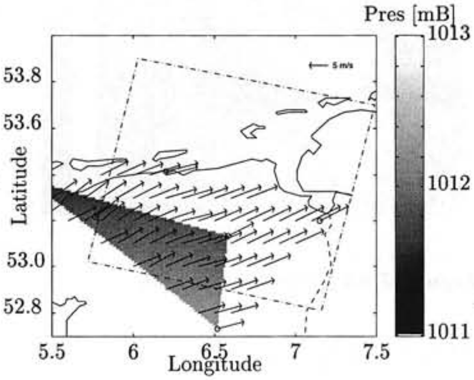

Figure 5.33 *Pressure and surface wind field gd6, day 2, 10:00 UTC*

At day 2, we see in the AVHRR image that cloud streets seem to be forming directly over our test area. The direction and significance of these cloud streets corresponds closely with the direction in the interferogram, where we find striation in the direction of the surface winds. The amplitude and diameter of the phase effects increases towards the east, as corresponds with the AVHRR imagery. It is possible that this wind "carries" moisture over the IJsselmeer to our test area which condensates due to convective heating over land, and thus forms the cloud streets. A plot of the wind vectors in the area confirms this hypothesis.

Station	#	UTC	Day	Level 1	Level 2
Leeuwarden	270	1000	1	2/8, Cu, 400 m	4/8, Cu, 500 m
Eelde	280	1000	1	5/8, Cu, 500 m	6/8, Ac, 3300 m
Leeuwarden	270	1100	1	1/8, Cu, 400 m	5/8, Cu, 500 m
Eelde	280	1100	1	3/8, Cu, 650 m	6/8, Ac, 3300 m
Leeuwarden	270	1000	2	2/8, Cu, 800 m	4/8, Ac, 3000 m
Eelde	280	1000	2	3/8, Cu, 1100 m	
Leeuwarden	270	1100	2	3/8, Cu, 800 m	
Eelde	280	1100	2	2/8, Cu, 1000 m	5/8, Ac, 3300 m

Table 5.6 *Cloud observations gd6: 25-05/26-05-1996. The observations give the amount of cloud cover (okta), the type of cloud, and the cloud base at 2 levels.*

5.2.6.3 Conclusions

Cloud streets in the wind direction are the most likely cause for the artifacts in the interferogram. Transport of moisture from the IJsselmeer changes from laminar flow to turbulent flow in the area. Main indicators for the effects are the AVHRR imagery and the synoptic observations.

5.2.7 Analysis of interferogram gd7

Interferogram gd7 was acquired at August 3 and 4, 1996, at 10:31:48 UTC (12:31:48 LT). SAR frame number 2529. ERS-1 orbit 26420, ERS-2 orbit 6747. The parallel baseline is 46 m, the perpendicular baseline 103 m. Phase unwrapping was performed using the minimal cost flow algorithm (Costantini, 1996). There were no precise state vectors available for the ERS-1 orbit, which resulted in a relative baseline error of 6.3 m. A manual correction for the orbit errors was therefore necessary. Furthermore, the SAR processing caused an error in the handling of the Sampling Window Start Time Shift. This caused the loss of coherence in the upper right corner of the interferogram.

5.2.7.1 Observations

Atmospheric artifacts, growing in scale from the upper to the lower side of the image (figure 5.34), are characteristic in this interferogram. The amplitude of the artifacts is growing towards a bit more than a cycle. No specific direction is visible in the disturbances. In the northern part of the area, the patterns have a small honeycomb pattern. The unwrapped interferogram, or the absolute phase, is shown in figure 5.35. Figure 5.36 is the histogram over the main part of the image, showing a smooth Gaussian curve with an rms of 1.8 rad. Figure 5.37 is the rotationally averaged spectrum. Between 0.5 and 2.5 km wavelengths, the −5/3 Kolmogorov power law is followed.

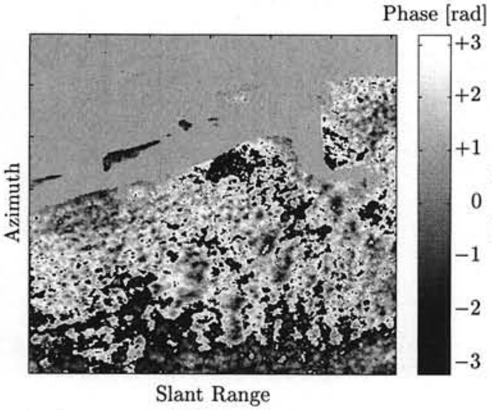

Figure 5.34 *Interferogram gd7*

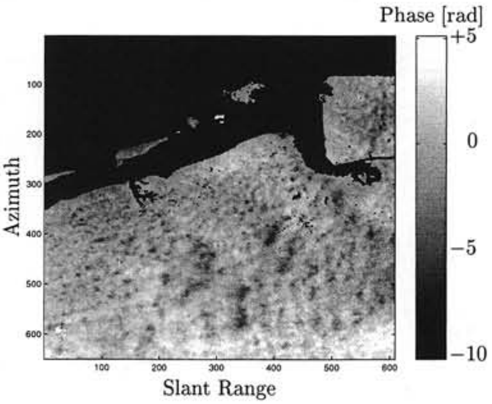

Figure 5.35 *Unwrapped interferogram gd7*

5.2.7.2 Interpretation

The weather radar does not show any rain on both days. The synoptic data indicate that there was a north-western wind at day 1 (4 m/s), with very good visibility. At day 2, the visibility is again splendid, while the wind was weaker (1–2 m/s) and from the east. At day 1, about 4/8 cumulus is observed at approximately 900–1100 m. At day 2, there is about 2/8 cumulus at about 1000 m. Based on the cloud observations, local disturbances in the interferogram are expected. At both days, the temperature was around 19°C.

The first day, there was an in-flow of humidity from the sea, the second day this in-flow was cut-off by eastern winds.

AVHRR-images from 11:50 UTC show at day 1 cumulus clouds, growing from the northern coast line to the lower side of the interferogram. Their influence should be a positive

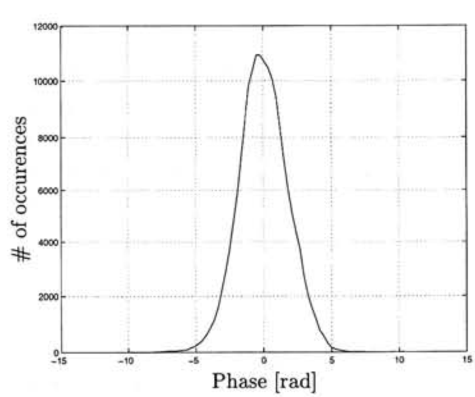

Figure 5.36 *Histogram of major part of interferogram gd7*

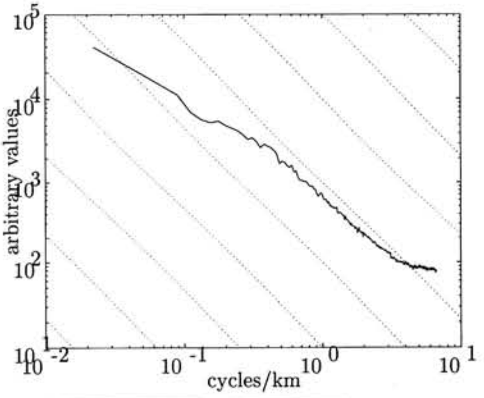

Figure 5.37 *Rotational averaged spectrum of interferogram gd7*

interferometric phase. This pattern can be recognized in the interferogram. At the same time at day 2, only some very small cumulus clouds are visible, having a more ore less east–west orientation. Their influence should, however, be small. These clouds, both at day 1 and 2, are too small to be distinguished in the Meteosat data.

Station	#	UTC	Day	Level 1	Level 2
Leeuwarden	270	1000	1	4/8, Cu, 900 m	
Eelde	280	1000	1	4/8, Cu, 1100 m	
Leeuwarden	270	1100	1	4/8, Cu, 900 m	
Eelde	280	1100	1	3/8, Cu, 1100 m	3/8, Sc, 3000 m
Leeuwarden	270	1000	2	2/8, Cu, 800 m	
Eelde	280	1000	2	1/8, Cu, 1000 m	
Leeuwarden	270	1100	2	2/8, Cu, 1100 m	
Eelde	280	1100	2	1/8, Cu, 1100 m	

Table 5.7 *Cloud observations gd7: 03-08/04-08-1996. The observations give the amount of cloud cover (okta), the type of cloud, and the cloud base at 2 levels.*

5.2.7.3 Conclusions

The observed effects in the interferogram are due to cloud cover heterogeneities: cumulus clouds in varying sizes. The direction on which the artifacts grow in amplitude and size corresponds closely with the wind direction at day 1.

5.2.8 Analysis of interferogram gdex2

Interferogram gdex2 was acquired at February 26 and 27, 1996, at 10:29:05 UTC, or 11:29:05 LT. SAR frame number 2529. ERS-1 orbit 24144, ERS-2 orbit 4471. The parallel baseline is −15 m, the perpendicular baseline −31 m. Phase unwrapping is performed using the minimal cost flow algorithm (Costantini, 1996). This interferogram, covering the Dutch-German border area around the Eems estuary, was originally not planned for this study. Considering its availability, however, it has been included as well. The amount of synoptic observations for the area is limited.

5.2.8.1 Observations

The interferogram gdex2, (figure 5.38), is characterized by mainly a long wavelength trend, of almost 1 cycle from the upper left side to the lower right side of the image. Due to its nature, it is not expected that orbit errors are causing it, although a small trend could still be caused by orbit inaccuracies. In two parts of the unwrapped interferogram, outlined by the square boxes A and B shown in figure 5.39, small waves can be observed. A 3D view of these parts is shown in figure 5.40 and 5.41, and profiles perpendicular to the waves in figure 5.42 and 5.43. Profile A has a wavelength of about 1 km and an amplitude of less than 0.4 rad. The direction of the waves is −60 degrees with respect to the azimuth direction, which corresponds to −44 degrees with respect to the north. Profile B has a shorter wavelength, around 600 m, and an amplitude of 0.4 rad. The direction is the same as for extraction A.

The histogram, figure 5.44 indicates a superposition of three Gaussian curves, centered around −3, −1, and 3 radians respectively. The superposition is caused by the long wavelength curve over the interferogram. The overall rms is 1.9 rad. Figure 5.45 is the rotationally averaged spectrum, showing a perfect −5/3 power law behavior over the range from 0.012 to 1.2 cycles per km, corresponding with wavelengths between 800 m and 80 km.

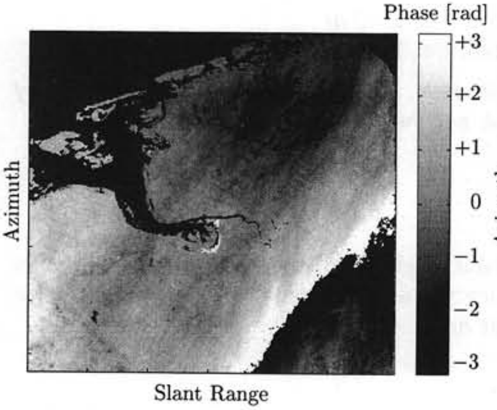

Figure 5.38 *Interferogram gdex2*

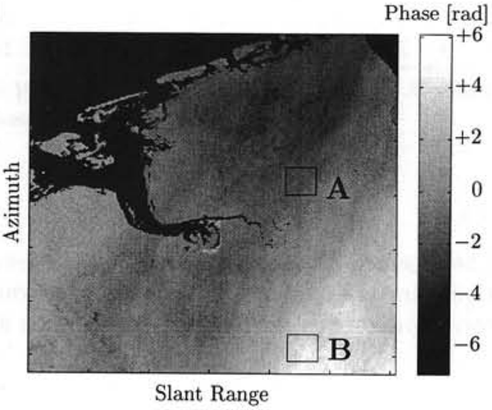

Figure 5.39 *Unwrapped interferogram gdex2*

5.2.8.2 Interpretation

In the interferogram smooth variations and waves of small wavelength and amplitude are observed. Based on the weather charts, the smooth variations might be due to a

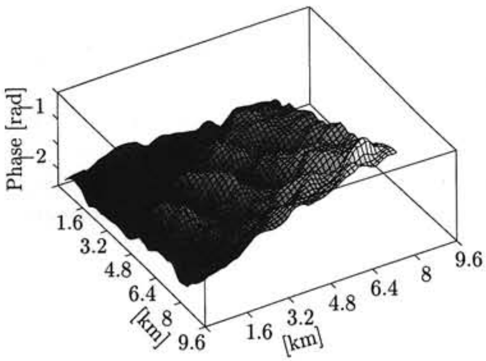

Figure 5.40 *Extraction A from interferogram gdex2*

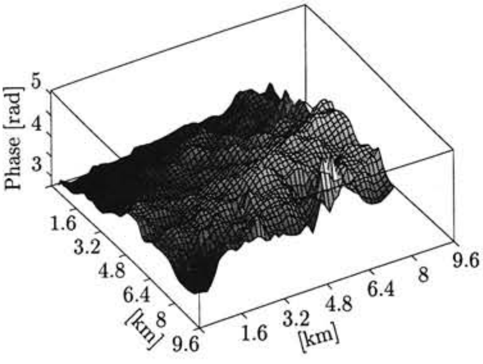

Figure 5.41 *Extraction B from interferogram gdex2*

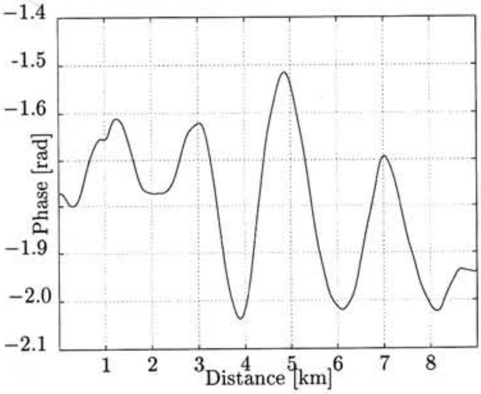

Figure 5.42 *Profile over extraction A, perpendicular to waves in gdex2*

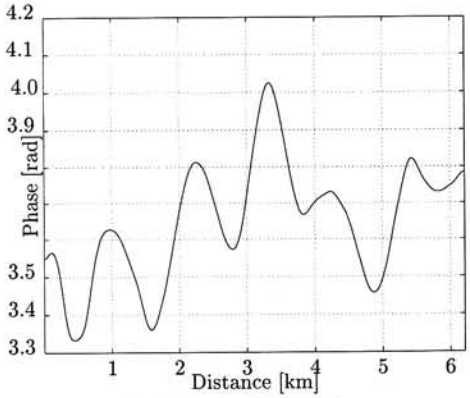

Figure 5.43 *Profile over extraction B, perpendicular to waves in gdex2*

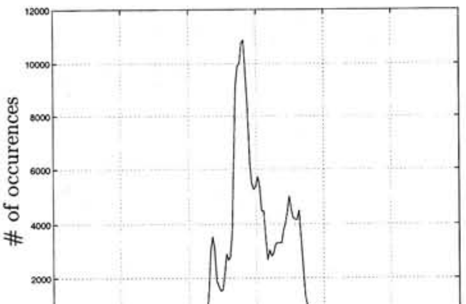

Figure 5.44 *Histogram of major part of interferogram gdex2*

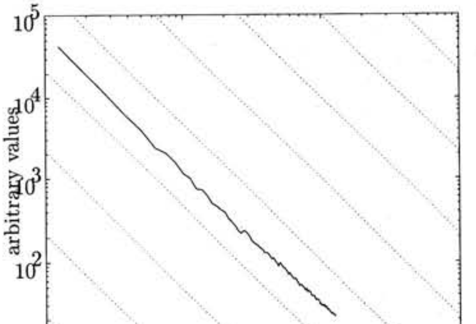

Figure 5.45 *Rotational averaged spectrum of interferogram gdex2*

quasi-stationary frontal system during both days.

From the Meteosat data we derive that the meteorological situation is complicated: a cold front smoothly turns into a warm front when following the front from north to south. The area can, however, be classified as a frontal zone. The second day, the front has shifted little to the east.

The weather radar does not reach far enough into the area of interest. However, from the available data we expect that the rain area is oriented in north-east–south-western direction, and it covers most of the south-eastern part of the study area, shifting even slightly more to the south-east on day 2.

From the synoptic data we derive that there was slight drizzle and rain at the first day, and local fog or freezing fog at the second day with a visibility at Eelde of 700–1400 m. The Eelde station reported three cloud layers at day 1: 1/8 stratus at 300 m, 4/8 stratocumulus at 800 m , and 8/8 altostratus at 4 km. At both days there was a high relative humidity of 100%. The second day, it reported 2/8 stratus at 30 m, and 6/8 altocumulus at 4 km. There was not much wind, 3–5 m/s, from south-western direction. It was approximately 4°C.

Unfortunately, only the radiosonde profile from Emden for the first day was available, and wind speed and direction measures were not available as well. The radiosonde profile at day 1, however, indicated a fully saturated layer at 1.2 km. It is possible that the small waves are gravity waves, which find their origin around this layer.

Station	#	UTC	Day	Level 1	Level 2	Level 3
Eelde	280	1000	1	1/8, St, 300 m	4/8, Sc, 800 m	8/8, As, 3300 m
Eelde	280	1100	1	3/8, Sc, 1200 m	8/8, As, 3300 m	
Eelde	280	1000	2	1/8, St, 0 m	6/8, Ac, 3300 m	
Eelde	280	1100	2	2/8, St, 0 m	6/8, Ac, 3300 m	

Table 5.8 *Cloud observations gdex2: 26-02/27-02-1996. The observations give the amount of cloud cover (okta), the type of cloud, and the cloud base at 3 levels.*

The interferogram seems to indicate the frontal zone. In the Meteosat WV image, the structure (wave) of the front is clearly visible, and the direction closely corresponds with the direction of the long wavelength effect in the interferogram. Unfortunately, no AVHRR imagery was available. Based on the sign of the disturbance, which is positive, the main disturbance is expected at the first day.

5.2.8.3 Conclusions

The large scale disturbance in the interferogram is believed to be caused by a quasi-stationary front at the first day. Synoptic weather charts give a first indication for this explanation, and Meteosat confirms this as well. The orientation of the waves, where the wave crests are perpendicular to the wind direction, indicates their origin as gravity waves, possibly in a small, fully saturated layer at day 1.

5.3 Analysis Delft descending

A single SAR pair was processed interferometrically and interpreted over the south-western parts of the Netherlands, over the provinces *Zeeland*, *Noord-Brabant*, and *Zuid-Holland.* The south-eastern part of the interferogram is situated over *Belgium.* Especially the province Zeeland is characterized as a delta region of the rivers Maas and Rhine, and consists of a number of islands. Figure 5.46 shows the location of the islands. Over most of the area the topographic variation is less than 2 meters. A small area in the south-west of the interferogram reaches heights of 20 meters.

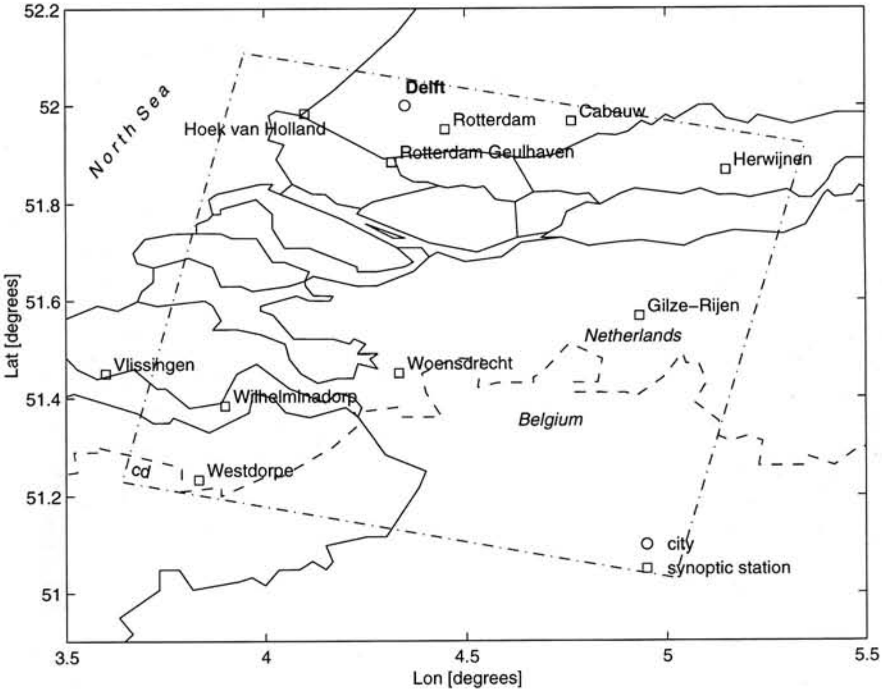

Figure 5.46 *Map of the area for the interferogram Delft descending, showing the position of the synoptic stations with some relevant topographical information, referred to in the text.*

This area is also labeled *CLARA descending*, since the data were acquired simultaneously with a part of the meteorological *CLouds And RAdiation* experiment (van Lammeren et al., 1997), which enables comparison with many additional and more unconventional atmospheric observations.[2] Aircraft measurements of droplet size, temperature, pressure, and relative humidity were carried out in the region over the city of *Delft*, shown

---

[2] see `http://www.knmi.nl/CLARA/`

in figure 5.46, as well as water vapor radiometer, lidar, GPS, ground based radar, and radiosonde observations. The analysis of the interferograms using these additional observations is, however, beyond the scope of this report, and a subject for further research.

5.3.1 Analysis of interferogram cd1

Interferogram cd1 was acquired at April 23 and 24, 1996, at 10:38:07 UTC (12:38:07 LT). The SAR frame number is 2565, for ERS-1 orbit 24960, and ERS-2 orbit 5287. The parallel baseline is 38 m, the perpendicular baseline 78 m. Phase unwrapping was performed using the method of Ghiglia and Romero (1994).

5.3.1.1 Observations

The interferogram labeled cd1, figure 5.47, shows lineated series of small anomalies, with some stronger disturbances just under the center of the image. Phase changes are limited to about one cycle. The unwrapped interferogram is shown in figure 5.48. Water areas are masked out for this analysis.

The rms value of the interferogram is 1 rad. The full histogram is shown in figure 5.49, revealing a Gaussian shape. The rotationally averaged spectrum, figure 5.50, completes the analysis. The spectrum follows the $-5/3$ lines for wavelengths between 0.5 and 2 km.

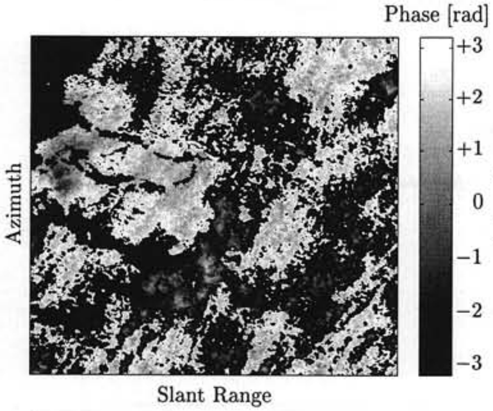

Figure 5.47 *Interferogram cd1*

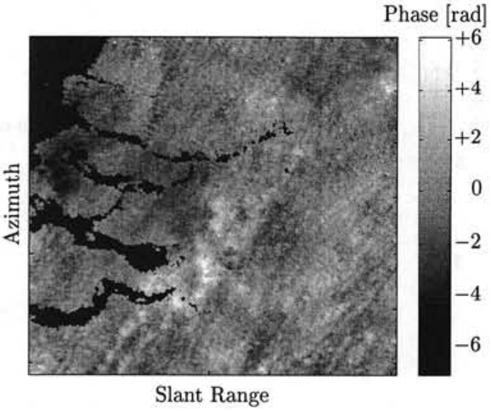

Figure 5.48 *Unwrapped interferogram cd1*

5.3.1.2 Interpretation

In the interferogram, the phase striations have a clear orientation. This corresponds very accurately to the wind directions observed, see figure 5.54. In the upper left corner, also wave features perpendicular to the wind direction are apparent.

At day 1, a cold front has just passed the test area. This gives rise to isolated showers. Cloud tops reach up to 6 km. The wind direction was south-southwest. At 10:00 UTC, both Gilze-Rijen and Woensdrecht reported rain. Rotterdam reported no rain. At 11:00 UTC,all stations reported “no rain”. The synoptic situation confirms the showery weather. In the radiosondes we see instabilities and cold advection.[3] The relative humidity is 60–80%. There is a lot of wind: wind force 6 or 7 (see table 4.3, p. 38), and

---

[3] Advection is the horizontal transport of air or atmospheric properties. The term is commonly used

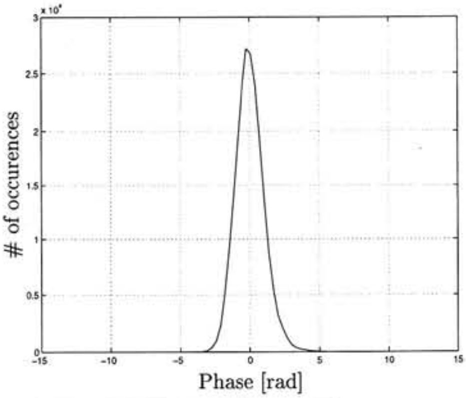

Figure 5.49 *Histogram of major part of interferogram cd1*

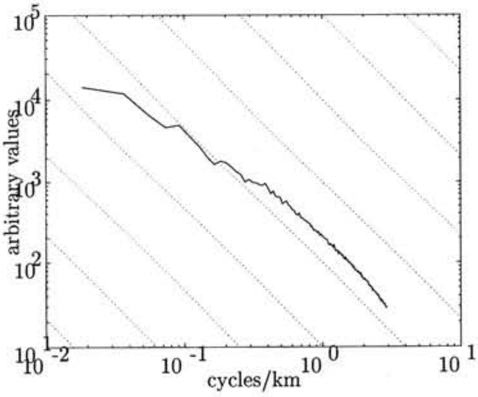

Figure 5.50 *Rotational averaged spectrum of interferogram cd1*

not much precipitation. The cloud cover observations report cumulus, cumulonimbus, stratocumulus, and altocumulus, see table 5.9.

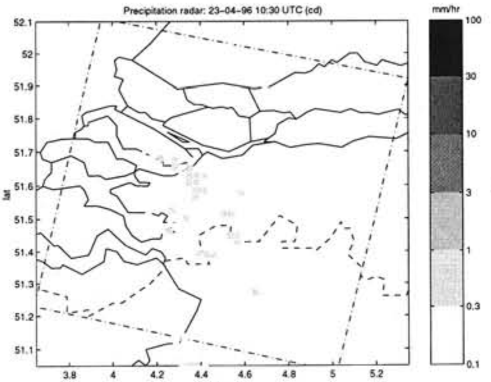

Figure 5.51 *Weather radar cd1, day 1, 10:30 UTC*

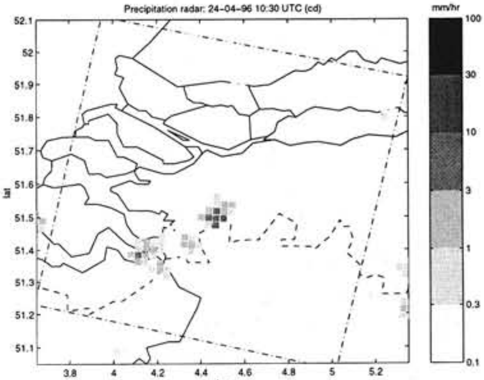

Figure 5.52 *Weather radar cd1, day 2, 10:30 UTC*

Stratocumulus fields are visible in the AVHRR imagery and the interferometric images.

At day 2 the front is already far away, over Central Europe. There is advection of polar air. The weather radar indicates a shower over Woensdrecht, with cloud tops at 8 km. Vlissingen indicates a moderate shower and Woensdrecht a light shower. In terms of cloud cover, cumulonimbus, stratocumulus, cumulus, and altocumulus is reported. The wind direction is mainly southwest.

---

with temperatures, i.e., "warm air advection". A cold advection is defined as the transport of cold air into a region by horizontal winds.

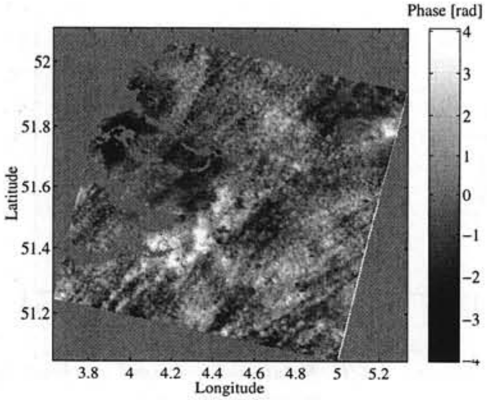

Figure 5.53 *Geocoded absolute interferogram cd1*

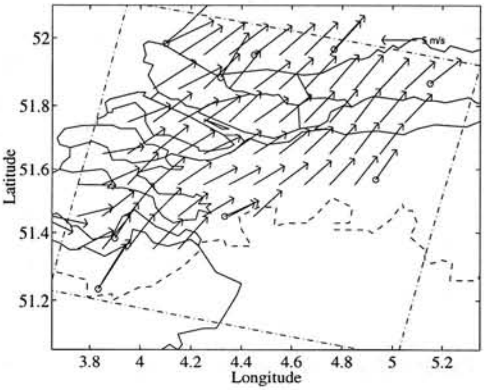

Figure 5.54 *Pressure and surface wind field cd1, day 2*

Station	#	UTC	Day	Level 1 (m)	Level 2 (km)	Level 3 (km)
Vlissingen	310	1000	1	1/8, Cu, 1000	3/8, Cu, 1.1	7/8, Ac, 3.3
Hoek v. Holland	330	1000	1			
Woensdrecht	340	1000	1	2/8, Cu, 800	3/8, Sc, 3.0	6/8, Ac, 3.3
Rotterdam	344	1000	1	2/8, Cu, 800	3/8, Sc, 3.0	7/8, Ac, 3.3
Gilze-Rijen	350	1000	1	1/8, Cb, 650	3/8, Sc, 1.6	6/8, Ac, 3.0
Vlissingen	310	1100	1	3/8, Cu, 1200	6/8, Ac, 3.3	
Hoek v. Holland	330	1100	1			
Woensdrecht	340	1100	1	2/8, Cu, 1000	6/8, Ac, 3.3	
Rotterdam	344	1100	1	3/8, Cu, 1000	6/8, Ac, 3.0	
Gilze-Rijen	350	1100	1	1/8, Cu, 800	6/8, Sc, 3.0	
Vlissingen	310	1000	2	2/8, Cu, 900		
Hoek v. Holland	330	1000	2			
Woensdrecht	340	1000	2	1/8, Cu, 1000	6/8, Ac, 3.0	
Rotterdam	344	1000	2	1/8, Cu, 1000	7/8, Ac, 3.3	
Gilze-Rijen	350	1000	2	1/8, Cu, 900	5/8, Ac, 3.0	
Vlissingen	310	1100	2	2/8, Cb, 1000	4/8, Sc, 1.5	
Hoek v. Holland	330	1100	2			
Woensdrecht	340	1100	2	1/8, Cb, 1000	3/8, Sc, 1.6	
Rotterdam	344	1100	2	3/8, Cu, 1100		
Gilze-Rijen	350	1100	2	4/8, Cu, 1200		

Table 5.9 *Cloud observations cd1: 23-04/24-04-1996. The observations give the amount of cloud cover (okta), the type of cloud, and the cloud base at 3 levels.*

5.3.1.3 Conclusions

The observed structures are probably not cloud streets: with the instabilities seen and the strong winds reported no cloud streets will form. Furthermore, no inversion exists that could give rise to cloud street formation. However, the orientation of the rectilinear structures corresponds closely with the wind direction, and could therefore be caused by transport of moisture. The stronger phase signatures are attributed to the showers. Weather radar signals coincide with the main phase disturbances.

5.4 Analysis Flevoland descending

Interferogram *Flevoland descending* covers the central part of the Netherlands, and shows the central lake, *IJsselmeer*, surrounded by the provinces *Noord-Holland* in the west, *Utrecht* in the south, *Overijssel* in the south-east, and *Friesland* in the north. Within the IJsselmeer, two polders are situated. *Flevoland* covers the southern part of the IJsselmeer, and is sometimes subdivided in a northern and a southern part, *Noord-Flevoland* and *Zuid-Flevoland* respectively. *Noord-oostpolder* is situated in the most eastern part of the IJsselmeer lake area. Both polders are very flat areas with heights varying between -2 and $+3$ meters.

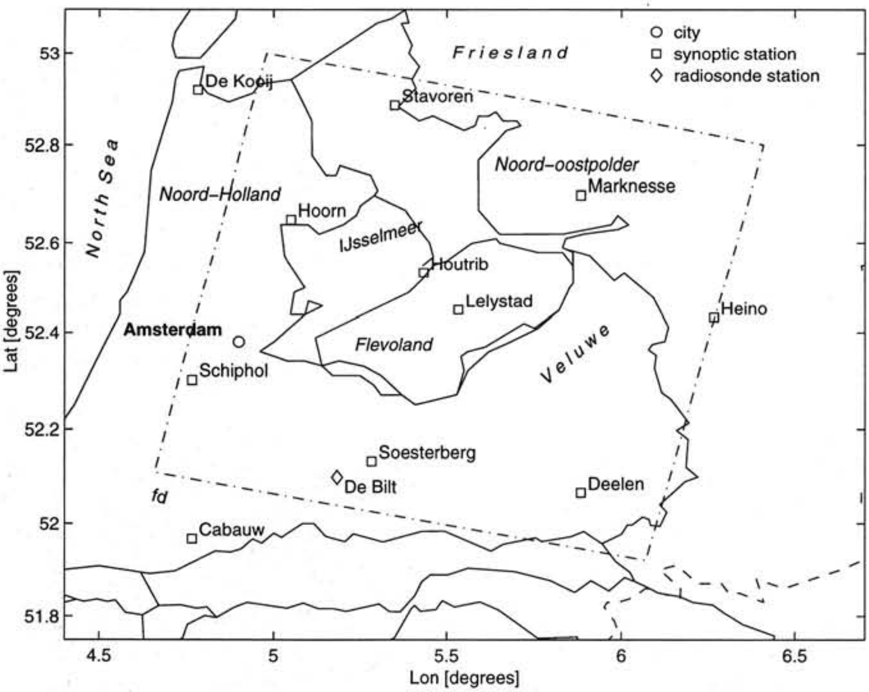

Figure 5.55 *Map of the area for the interferograms Flevoland descending, showing the position of the synoptic and radiosonde stations with some relevant topographical information, referred to in the text.*

In the south-eastern part of the interferogram area, the *Veluwe* is a hilly elevated area of glacial origin. The maximum height is approximately 100 m. Additionally to the Veluwe area, some small, less elevated areas are situated in the southern part of the interferograms. Apart from these area, the variation of topographic height in the interferogram area is small, within 5 meters.

The map in figure 5.55 shows the position of the synoptic stations, as well as the city of *Amsterdam*. Manual cloud observations are available from the stations *De Kooij*, *Schiphol*, *Soesterberg*, *Deelen* and *De Bilt*. Radiosondes are being launched four times daily from the latter station.

5.4.1 Analysis of interferogram fd1

Interferogram fd1 was acquired at August 3 and 4, 1995, at 10:35:06 UTC (12:35:06 LT). SAR frame number 2547, for ERS-1 orbit 21181, and ERS-2 orbit 1508. The parallel baseline is 32 m, the perpendicular baseline 58 m. The minimal cost flow algorithm (Costantini, 1996) is used for phase unwrapping.

5.4.1.1 Observations

Interferogram *fd1*, (figure 5.56), shows phase variations with a magnitude of one cycle. Lineated structures, referred to as striation, crossing the interferogram diagonally, can be observed over the whole image. Especially in the unwrapped interferogram, figure 5.57, it can be observed how the striation organized. The main direction is from upper right to lower left, but some deviations can be seen at the left side of the image, where the directions tends more towards a horizontal direction, and at the lower right corner, where the striation seem to "curve". First the direction is more vertically inclined, but after some distance, it re-finds its original direction. The position where this curve appears, is just before the *Veluwe*, an elongated hill with a maximum height of about 100 meters.[4]

The histogram, shown in figure 5.58 shows a smooth Gaussian distribution, with an rms of 1.7 rad. The rotationally averaged spectrum in figure 5.59 shows how wavelengths between 400 and 2000 m, and 12.5 and 25 km follow roughly the $-5/3$ exponential reference line.

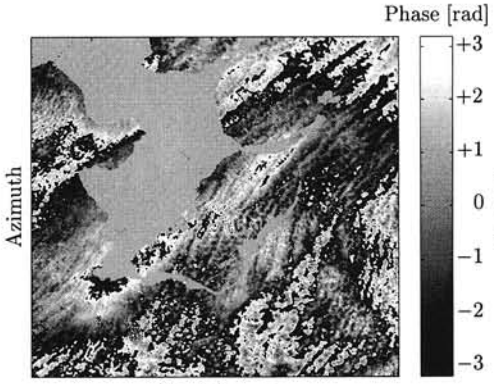

Figure 5.56 *Interferogram fd1*

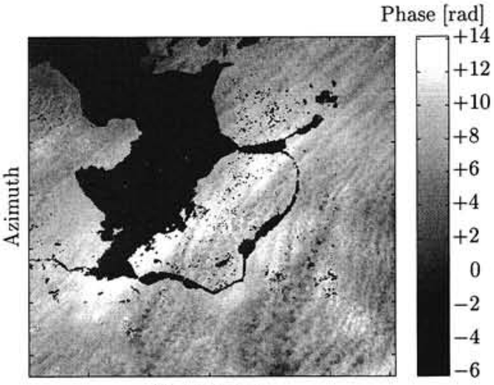

Figure 5.57 *Unwrapped interferogram fd1*

5.4.1.2 Interpretation

The interferogram shows lineated structures or striation which at some points become more diffused, and form more or less isolated cells in the lower part of the image.

---

[4] See figure 5.73 at page 81 for an impression of the topography

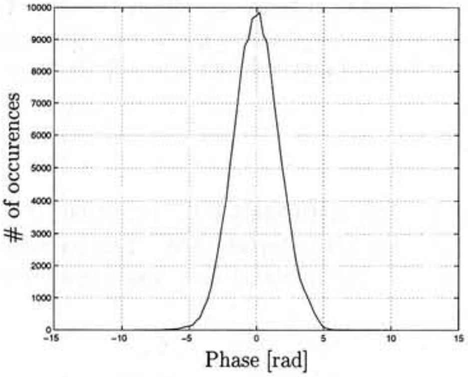

Figure 5.58 *Histogram of major part of interferogram fd1*

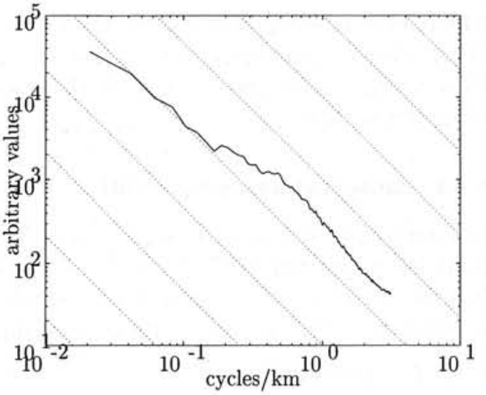

Figure 5.59 *Rotationally averaged spectrum of interferogram fd1*

The Meteosat image of day 1 reveals a large area of fog/stratus over the North Sea. The weather radar gives some signal over Noord-Flevoland. This however, is an artifact associated with the scatter of the precipitation radar at an inversion layer. Therefore, there is no rain in the test area. The synoptic data at Houtrib indicate that there is some haze, with a reduced visibility to about 5 km. It is not that humid in the area, the relative humidity is around 60-70%. From the radiosonde data we conclude that there is quite some humidity throughout the whole tropospheric column. It concentrates around the inversion.

The radiosonde data clearly show that there is a subsidence inversion, lowering from 2000 m at day 1 to approximately 1200 m at day 2. At the second day, the inversion is stronger than at the first day.

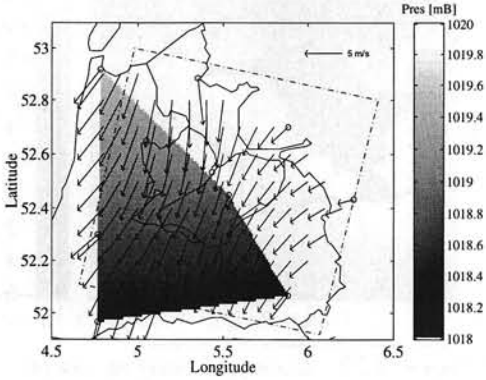

Figure 5.60 *Pressure and surface wind field fd1, day 1, 10:00 UTC*

At day 1 there is around 1/8 cumulus at 1.6 km, and 5/8 cirrus with a temperature around 23°C. At day 2 the temperature is slightly lower, around 21°C, and there is more cloud cover. In most parts of the area low level cumulus clouds are reported, see table 5.10.

Wind directions are northeast at day 1 and north at day 2.

A comparison of the unwrapped interferogram with a plot of wind directions at the synoptic stations at day 1, see figure 5.60, shows striking similarities, especially since it has such a characteristic behavior at this day. The striation aligns with the wind vectors of most stations. In the lower right part of the interferogram the elongated hills of the *Veluwe*, seem to spread the flow apart. Since the wind direction was more north at day 2, the observed effects cannot be caused at that time. The relatively low relative humidities at the surface indicate that the moisture must be at higher altitudes, possibly at the inversion altitude.

Station	#	UTC	Day	Level 1	Level 2
De Kooij	235	1000	1	1/8, Ac, 3300 m	3/8, Ci, 8300 m
Schiphol	240	1000	1	5/8, Ci, 8300 m	
De Bilt	260	1000	1	1/8, Cu, 1600 m	
Soesterberg	265	1000	1	1/8, Cu, 1300 m	6/8, Ci, 8300 m
Deelen	275	1000	1	1/8, Cu, 1500 m	4/8, Ci, 8300 m
De Kooij	235	1100	1	1/8, Ac, 3300 m	4/8, Ci, 8300 m
Schiphol	240	1100	1	1/8, Cu, 1600 m	4/8, Ci, 8300 m
De Bilt	260	1100	1	2/8, Cu, 1500 m	
Soesterberg	265	1100	1	1/8, Cu, 1400 m	5/8, Ci, 8300 m
Deelen	275	1100	1	1/8, Cu, 1600 m	5/8, Ci, 10000 m
De Kooij	235	1000	2	1/8, Cu, 800 m	6/8, Sc, 1400 m
Schiphol	240	1000	2	2/8, Sc, 1200 m	7/8, Ci, 10000 m
De Bilt	260	1000	2	3/8, Cu, 1000 m	6/8, Ci, 8300 m
Soesterberg	265	1000	2	2/8, Cu, 1000 m	6/8, Ci, 10000 m
Deelen	275	1000	2	1/8, Sc, 800 m	5/8, Ci, 8300 m
De Kooij	235	1100	2	1/8, Cu, 800 m	6/8, Sc, 1400 m
Schiphol	240	1100	2	1/8, Cu, 1000 m	6/8, Sc, 1200 m
De Bilt	260	1100	2	1/8, Cu, 1200 m	5/8, Ci, 8300 m
Soesterberg	265	1100	2	2/8, Cu, 1200 m	5/8, Ci, 10000 m
Deelen	275	1100	2	2/8, Sc, 900 m	4/8, Ci, 8300 m

Table 5.10 *Cloud observations fd1: 03-08/04-08-1995. The observations give the amount of cloud cover (okta), the type of cloud, and the cloud base at 2 levels.*

5.4.1.3 Conclusions

The observed effects are most likely due to moisture fluctuations, transported by the wind at day 1. The moisture does, however, not necessary indicate visible cloud streets. It may be appropriate to speak of "moisture streets" in this context.

5.4.2 Analysis of interferogram fd2

Interferogram fd2 was acquired at September 7 and 8 , 1995, at 10:35:04 UTC, or 12:35:04 LT. SAR frame number 2547, for ERS-1 orbit 21682, and ERS-2 orbit 2009. The parallel baseline is 30 m, the perpendicular baseline 37 m. Phase unwrapping was performed using the minimal cost flow algorithm (Costantini, 1996).

5.4.2.1 Observations

The variation in the interferometric phase of interferogram fd2, figure 5.61, is relatively smooth for large parts, although small variations can be found as well. Wave effects can be observed in the Noord-oostpolder (at the right side of the IJsselmeer), and just under the Veluwe, in the lower right corner. The absolute phase is shown in figure 5.62. Note that there is loss of coherence over some forested areas. These areas have been masked for the analysis.

The histogram is shown in figure 5.63. The rms is 1.3 rad. The rotationally averaged spectrum of a significant area of the interferogram is drawn in figure 5.64. Over the whole range of wavenumbers, the slope angle differs from $-5/3$, although some similarity can be found for wavelengths within 3 and 8 km.

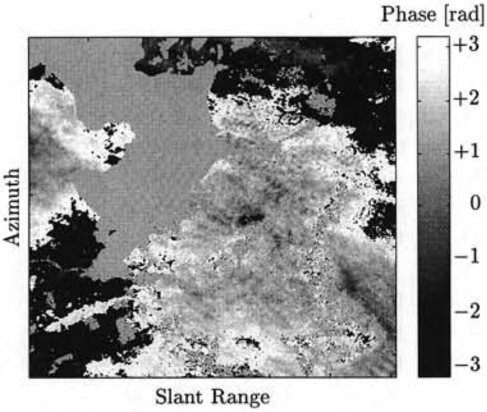

Figure 5.61 *Interferogram fd2*

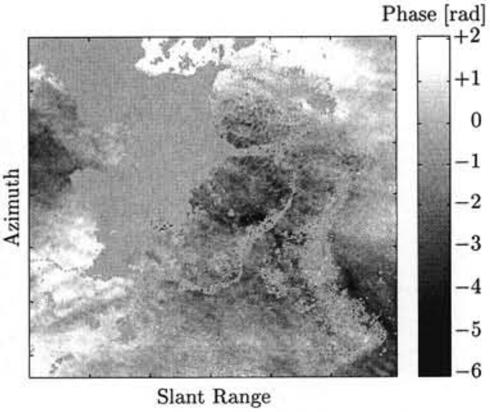

Figure 5.62 *Unwrapped interferogram fd2*

5.4.2.2 Interpretation

The light variations in the phase can be due to humidity changes associated with a frontal passage, or precipitation. A frontal zone has just passed the area, which makes it very humid. There are showers on day 1, after a front passage, and rain on day 2, associated with a secondary cold front just over the area. There is much cloud cover, on day 1 it is layered, on day 2 the cloud formation is solid up to 4 km. Above that level it is more layered.

The weather radar shows precipitation at both days. The radar image of day 1, figure 5.66, closely correlates with the anomalies in the interferogram. The rain cells have tops at around 4 km, which is not extremely high. The weather charts indicate an occlusion over the north-eastern part of the Netherlands. This results in an "upper level warm front". This means that the cold front overtakes the warm front, and forces the warm air to move upwards, see figure 5.65.

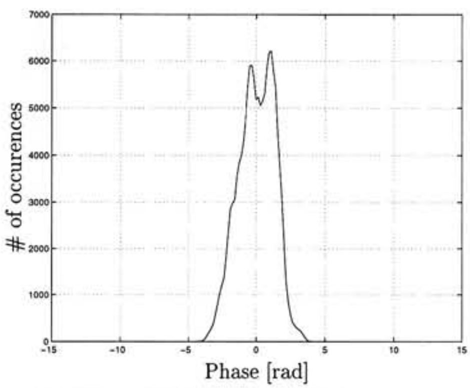

Figure 5.63 *Histogram of a significant part of interferogram fd2*

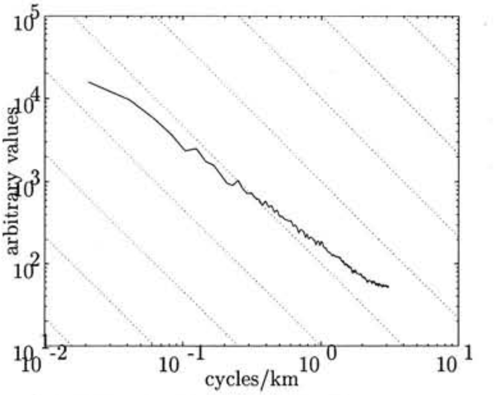

Figure 5.64 *Rotationally averaged spectrum of interferogram fd2*

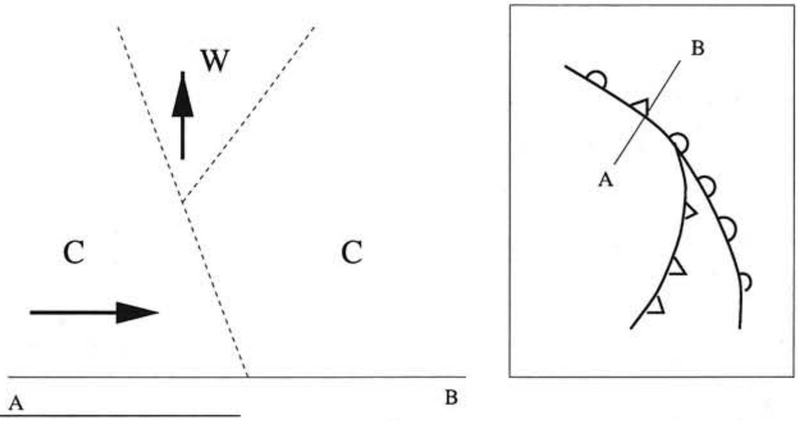

Figure 5.65 *An occlusion front. The right figure shows a top view of the configuration. The left figure shows the cross section labeled AB. Warm air is forced upward, creating an upper level warm front.*

At the second day, the low pressure area is centered right over the Netherlands. Weather radar time-loops clearly confirm the counterclockwise rotation. The anomalies in the north-eastern area of the interferogram correlate with the rain fields from the weather radar of day 2, see figure 5.67.

The synoptic data from Schiphol indicate that at day 1 there are rain showers over the area: it rains around 2 mm. At day 2 almost all stations report drizzle and/or rain.

The cloud reports are listed in table 5.11. Observations at day 1 include mainly stratocumulus and altocumulus. At day 2, it is mainly stratus and stratocumulus.

At day 1 the wind direction was southeast over nearly the whole image, at day 2 it turned from southeast at the right side of the image, to east at the left side. Due to this wind direction, the waves over the Noord-oostpolder are probably gravity waves at day 1.

The weather radar indicates tops of rain cells at 8 km for the second day. Synoptic data

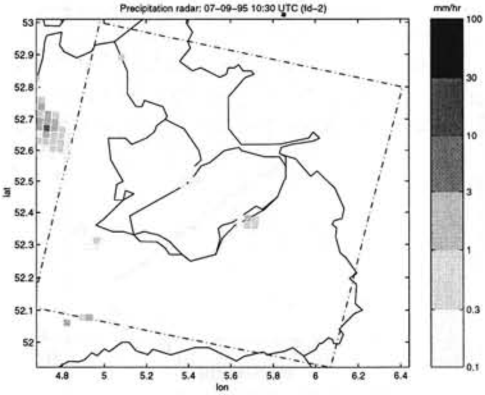

Figure 5.66 *Weather radar interferogram fd2, day 1, 10:30 UTC*

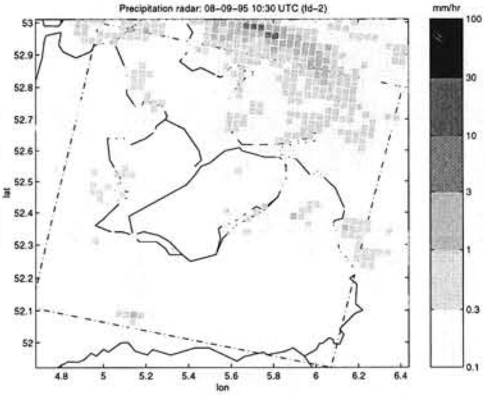

Figure 5.67 *Weather radar interferogram fd2, day 2, 10:30 UTC*

report showery precipitation. The radiosonde data confirm this cloud and rain analysis. At day 2, the whole boundary layer has a relative humidity of nearly 100%.

Station	#	UTC	Day	Level 1	Level 2	Level 3
De Kooij	235	1000	1	1/8, Cu, 1300	4/8, Sc, 1600	7/8, Ac, 3000
Schiphol	240	1000	1	1/8, Sc, 800	6/8, Ac, 3000	8/8, Cs, 6600
De Bilt	260	1000	1	1/8, Sc, 3000	4/8, Ac, 3000	7/8, As, 3300
Soesterberg	265	1000	1	2/8, Sc, 3000	8/8, Cs, 8300	
Deelen	275	1000	1	4/8, Sc, 1600	3/8, Ac, 3300	6/8, Ci, 8300
De Kooij	235	1100	1	1/8, Cu, 1300	3/8, Sc, 1600	5/8, Ac, 3000
Schiphol	240	1100	1	2/8, Ac, 3000	6/8, Ac, 3000	8/8, Cs, 6600
De Bilt	260	1100	1	3/8, Cu, 1000	7/8, As, 3300	8/8, Cs, 6600
Soesterberg	265	1100	1	2/8, Sc, 1100	3/8, Ac, 3300	7/8, Cs, 8300
Deelen	275	1100	1	1/8, Cu, 900	3/8, Sc, 3000	6/8, Ci, 8300
De Kooij	235	1000	2	2/8, Sc, 1000	5/8, Sc, 1500	6/8, Ac, 3300
Schiphol	240	1000	2	1/8, St, 250	5/8, Sc, 400	6/8, Sc, 500
De Bilt	260	1000	2	3/8, St, 200	5/8, St, 250	8/8, St, 300
Soesterberg	265	1000	2	3/8, St, 200	8/8, St, 300	
Deelen	275	1000	2	1/8, St, 200	3/8, Sc, 400	8/8, Sc, 650
De Kooij	235	1100	2	1/8, St, 250	3/8, Sc, 500	6/8, Sc, 700
Schiphol	240	1100	2	2/8, St, 150	5/8, St, 250	6/8, Sc, 400
De Bilt	260	1100	2	4/8, St, 200	6/8, St, 250	8/8, St, 300
Soesterberg	265	1100	2	4/8, St, 200	8/8, St, 300	
Deelen	275	1100	2	2/8, St, 200	4/8, Sc, 400	8/8, Sc, 600

Table 5.11 *Cloud observations fd2: 07-09/08-09-1995. The observations give the amount of cloud cover (okta), the type of cloud, and the cloud base at 3 levels. Height is given in meters.*

5.4.2.3 Conclusions

The phase variations are caused by precipitation at both days, which causes humidity variations. Other effects, such as the waves, are probably gravity waves at the first day. There is strong correlation between precipitation in the weather radar images and phase disturbance in the interferogram.

5.4.3 Analysis of interferogram fd3

Interferogram fd3 was acquired at October 12 and 13, 1995, at 10:34:58 UTC, or 11:34:58 LT. SAR frame number 2547, for ERS-1 orbit 22183, and ERS-2 orbit 2510. The parallel baseline is −127 m, the perpendicular baseline is −324 m. The phase unwrapping is performed using the minimal cost flow algorithm (Costantini, 1996).

5.4.3.1 Observations

Interferogram fd3, shown in figure 5.68, has an absolute perpendicular baseline of approximately 324 m. Therefore, the sensitivity of the interferometric configuration for height is high. The Veluwe is clearly visible in the interferogram, and causes up to 4 fringes. A reference DEM was transformed into the slant range geometry of the interferogram, and subtracted from the unwrapped interferogram. This differential unwrapped interferogram is shown in figure 5.69. A diagonal feature is visible in this differential interferogram, from the lower left corner to the upper right. Near Amsterdam, the phase gradient perpendicular to this feature is largest, while the gradient diminishes over the Noord-oostpolder.

The histogram is shown in figure 5.70, rms 1.3 rad, and the rotationally averaged spectrum in figure 5.71. The −5/3 gradient is only found in the 20–50 km wavelength range.

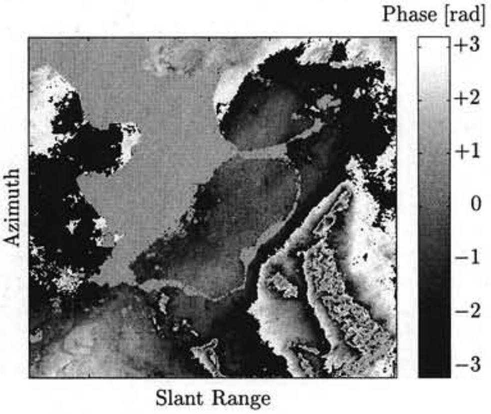

Figure 5.68 *Interferogram fd3, showing topographical as well as atmospheric fringes*

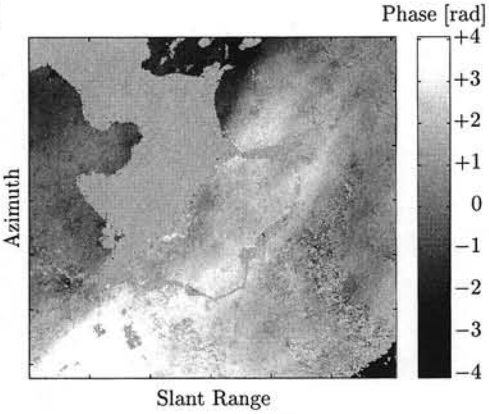

Figure 5.69 *Unwrapped differential interferogram fd3. Only atmospheric phase delay remains visible.*

5.4.3.2 Interpretation

At day 1, around 10:00 (12:00 local time) there was fog at Houtrib (in the middle of Flevoland). The strong intrusion over Flevoland could have some relation with the foggy area. Marknesse reports a reduced visibility of 1100 m: haze. Deelen reports a relative humidity of 92%, and reduced visibility to 1800 m. Also Lelystad reports reduced visibility: 1700 m. Therefore, the whole area can be considered as foggy, with visibilities between 900–2300 m. At 11:00 (13:00 local time) there is still fog, but now in more localized areas. The weather radar at day 1 indicates no rain, but has some signal due to an inversion layer. The radiosonde profile gives an inversion at approximately 400 m. The lower 40 m must be 100% humid. Meteosat lacks in resolution for this area. AVHRR shows the field of fog, which is not totally homogeneous.

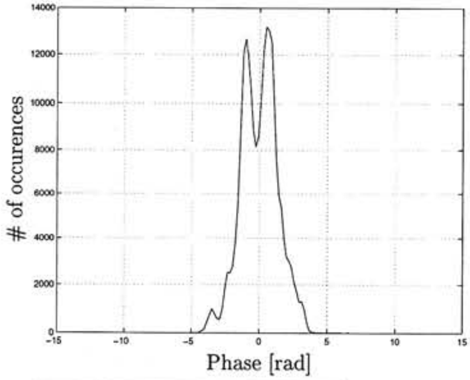

Figure 5.70 *Histogram of major part of interferogram fd3*

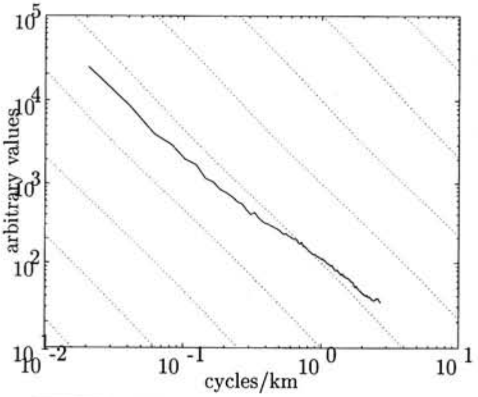

Figure 5.71 *Rotationally averaged spectrum of interferogram fd3*

At day 2 the fog covers a wider area: all stations report 100% relative humidity, with reduced visibility between 100–1400 m, both at 10:00 and 11:00 UTC. The humidity below the inversion is now completely mixed according to the radiosonde. The weather radar detects no rain signal.

Cloud cover and type observations are listed in table 5.12. The cloud cover at day 1 is mainly stratus. At day 2, De Bilt report 9/8 total cloud cover (not listed in the table), which means that the vertical visibility is less than 30 m. Other stations report stratus at low levels (70–100 m).

5.4.3.3 Conclusions

Water vapor distribution caused by fog gives rise to phase shifts. The diagonal feature over Flevoland is probably due to fog heterogeneities at day 1.

Station	#	UTC	Day	Level 1	Level 2	Level 3
De Kooij	235	1000	1	1/8, St, 150 m	6/8, St, 200 m	7/8, St, 300 m
Schiphol	240	1000	1	4/8, St, 150 m	8/8, St, 200 m	
De Bilt	260	1000	1	5/8, St, 150 m	8/8, St, 200 m	
Soesterberg	265	1000	1	2/8, St, 200 m	6/8, St, 200 m	8/8, St, 300 m
Deelen	275	1000	1	3/8, St, 200 m	8/8, St, 300 m	
De Kooij	235	1100	1	2/8, St, 150 m	6/8, St, 200 m	8/8, St, 250 m
Schiphol	240	1100	1	3/8, St, 200 m	6/8, St, 200 m	8/8, St, 300 m
De Bilt	260	1100	1	4/8, St, 200 m	7/8, St, 250 m	
Soesterberg	265	1100	1	6/8, St, 300 m	7/8, Ci, 8300 m	
Deelen	275	1100	1	2/8, St, 200 m	8/8, Sc, 350 m	
De Kooij	235	1000	2	1/8, St, 50 m	5/8, St, 100 m	8/8, St, 150 m
Schiphol	240	1000	2	6/8, St, 0 m	8/8, St, 0 m	
De Bilt	260	1000	2			
Soesterberg	265	1000	2	6/8, St, 0 m	8/8, St, 100 m	
Deelen	275	1000	2	8/8, St, 0 m		
De Kooij	235	1100	2	1/8, St, 50 m	5/8, St, 100 m	8/8, St, 150 m
Schiphol	240	1100	2	7/8, St, 0 m	8/8, St, 50 m	
De Bilt	260	1100	2	8/8, St, 150 m		
Soesterberg	265	1100	2	4/8, St, 0 m	8/8, St, 100 m	
Deelen	275	1100	2	4/8, St, 100 m	8/8, St, 100 m	

Table 5.12 *Cloud observations fd3: 12-10/13-10-1995. The observations give the amount of cloud cover (okta), the type of cloud, and the cloud base at 3 levels.*

5.4.4 Analysis of interferogram fd4

Interferogram fd4 was acquired at November 16 and 17, 1995, at 10:35:01 UTC, or 11:35:01 LT. SAR frame number 2547, for ERS-1 orbit 21181, and ERS-2 orbit 3011. The parallel baseline is 259 m, the perpendicular baseline 531 m. Phase unwrapping is performed using the minimal cost flow algorithm (Costantini, 1996).

5.4.4.1 Observations

Figure 5.72 is showing interferogram fd4. The absolute perpendicular baseline is 531 m, which explains the amount of fringes over the Veluwe and other small elevated areas in the terrain. The absolute phase of this interferogram, figure 5.73, is dominated by the effects of topography. Using the reference DEM of the area, a differential interferogram was created, see figure 5.74. Especially the upper left corner of this differential interferogram exhibits phase artifacts, starting from the lower-left/upper-right diagonal. The amount of phase bias in these areas reaches a maximum of more than a phase cycle. Figure 5.75 shows the unwrapped differential interferogram.

The histogram is shown in figure 5.78, (rms 1.8 rad), and the rotationally averaged spectrum in figure 5.79. The −5/3 range of wavelengths is 7–20 km.

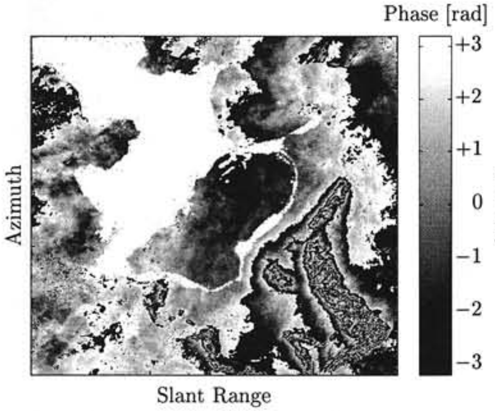

Figure 5.72 *Interferogram fd4*

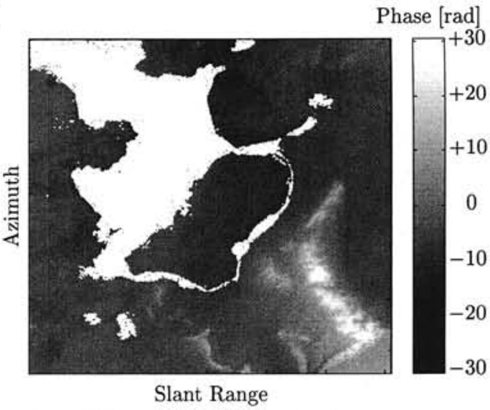

Figure 5.73 *Unwrapped interferogram fd4*

5.4.4.2 Interpretation

There is a cold front passage at day 1. Especially at day 2, there is showery precipitation. This may give rise to the small flake-like features in the interferogram.

The weather charts show that a cold front is passing over the Netherlands from the northwest. The weather radar indicates showers at day 1 over the northern part of the SAR image, consisting of embedded cumulonimbus clouds. Tops of the rain cells are located at about 6 km over Friesland, and 4 km over Noord-Holland. The rain rates over Friesland and Noord-Holland reach 10–30 mm/hr at some spots, which is heavy rain fall. This rain image corresponds very well with the disturbances in the interferogram, including the cloud heights and the amount of phase shift.

Meteosat High Resolution VIS shows the cells of heavy rain of the weather radar very clearly as "embedded Cb's" (cumulonimbus) over the Netherlands.

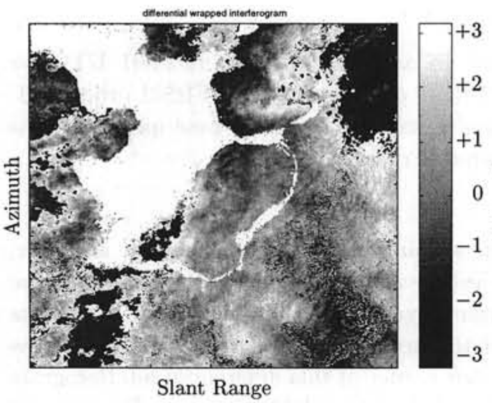

Figure 5.74 *Wrapped differential interferogram fd4*

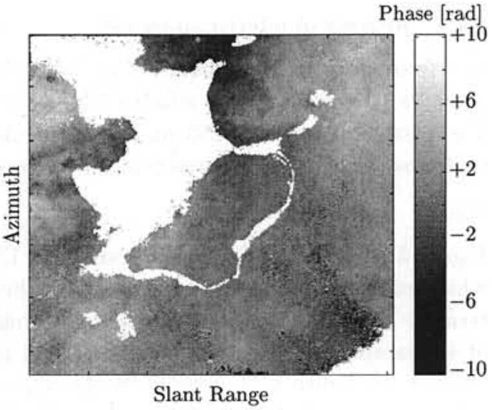

Figure 5.75 *Unwrapped differential interferogram fd4*

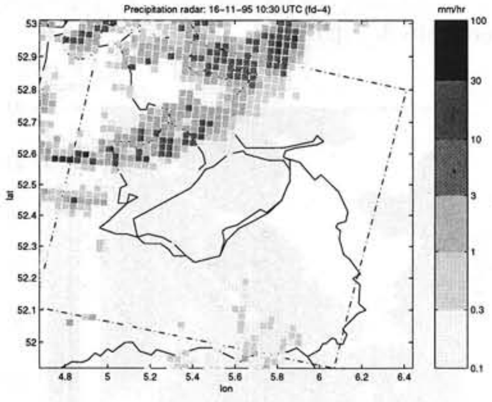

Figure 5.76 *Weather radar fd4, day 1*

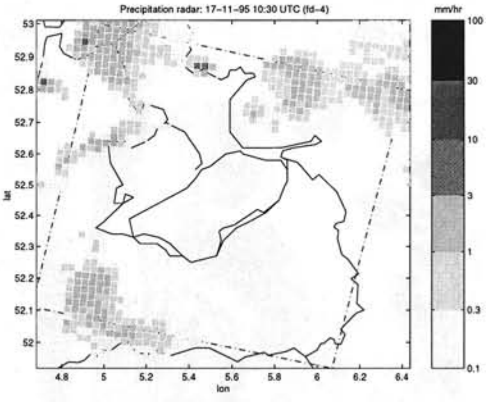

Figure 5.77 *Weather radar fd4, day 2*

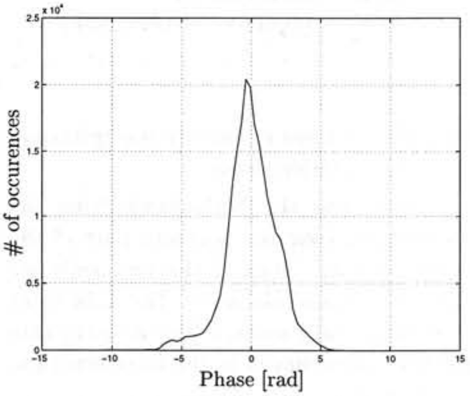

Figure 5.78 *Histogram of major part of interferogram fd4*

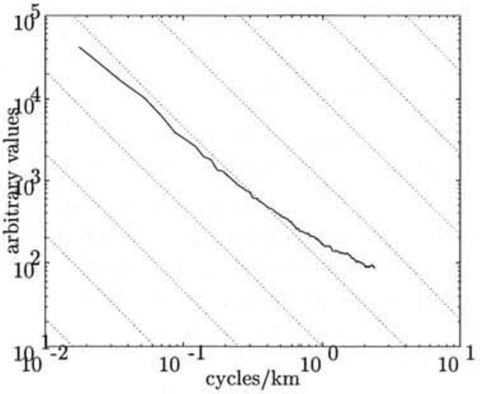

Figure 5.79 *Rotationally averaged spectrum of interferogram fd4*

The synoptic data at day 1 report around 10:00 UTC light and moderate showers. At 11:00 UTC, the rain front has moved a little further to the southeast. The showery precipitation gives rise to local differences in the rain intensities. Cloud reports all include cumulonimbus with a cloud base of approximately 500 m.

At day 2, the atmosphere is very unstable. There is a north-northwest flow and there is not much sunshine. The relative warm water of the North Sea in combination with the cold polar air results in lots of showers. The weather radar indicates these, sometimes at the same spots as day 1. All stations report cumulonimbus clouds and showers, although the showers are now more widespread than on day 1. The positions of the flake-structures in the weather radar seem to match the shower structure.

Station	#	UTC	Day	Level 1	Level 2	Level 3
De Kooij	235	1000	1	1/8, St, 250	3/8, Cb, 500	
Schiphol	240	1000	1	1/8, St, 250	3/8, Cu, 400	6/8, Sc, 1600
De Bilt	260	1000	1	2/8, Cu, 400	5/8, Cu, 500	5/8, Sc, 1600
Soesterberg	265	1000	1	4/8, Cu, 400	6/8, Sc, 500	
Deelen	275	1000	1	1/8, St, 200	3/8, St, 300	6/8, Sc, 450
De Kooij	235	1100	1	1/8, Cu, 500	3/8, Cu, 650	7/8, Ci, 8300
Schiphol	240	1100	1	1/8, St, 250	3/8, Cb, 500	
De Bilt	260	1100	1	1/8, Cu, 350	3/8, Cu, 500	7/8, Sc, 1600
Soesterberg	265	1100	1	4/8, Cu, 400	7/8, Sc, 3000	
Deelen	275	1100	1	2/8, St, 300	1/8, Cb, 450	5/8, Sc, 3000
De Kooij	235	1000	2	3/8, Cb, 600	3/8, Cu, 750	6/8, Ci, 6600
Schiphol	240	1000	2	1/8, St, 250	4/8, Cb, 400	
De Bilt	260	1000	2	1/8, Cu, 400	2/8, Cb, 650	7/8, Ac, 3300
Soesterberg	265	1000	2	1/8, Cu, 650	3/8, Sc, 1600	5/8, Ac, 3000
Deelen	275	1000	2	1/8, Cu, 700	5/8, Ac, 3000	5/8, Ci, 8300
De Kooij	235	1100	2	2/8, Cb, 600	4/8, Ci, 6600	
Schiphol	240	1100	2	1/8, Cb, 400	3/8, Cu, 500	7/8, Ci, 6600
De Bilt	260	1100	2	1/8, Cu, 500	3/8, Cb, 650	5/8, Ac, 3300
Soesterberg	265	1100	2	2/8, Cu, 650	3/8, Sc, 1600	5/8, Ci, 8300
Deelen	275	1100	2	1/8, Cu, 400	4/8, Ac, 3000	5/8, Ci, 8300

Table 5.13 *Cloud observations fd4: 16-11/17-11-1995. The observations give the amount of cloud cover (okta), the type of cloud, and the cloud base at 3 levels. Height is given in meters.*

5.4.4.3 Conclusions

The correspondence between the shower patterns from the weather radar and the phase distortion in the interferogram points at rain, associated with higher cumulonimbus clouds, as the main cause of the phase variation.

5.4.5 Analysis of interferogram fd5

Interferogram fd5 was acquired at December 21 and 22, 1995, at 10:35:07 UTC, or 11:35:07 LT. SAR frame number 2547, for ERS-1 orbit 23185, and ERS-2 orbit 3512. The parallel baseline is 62 m, the perpendicular baseline 173 m. Phase unwrapping is performed using the minimal cost flow algorithm (Costantini, 1996).

5.4.5.1 Observations

Interferogram fd5, figure 5.80, has relatively small disturbances, up to 1–1.5 rad. Extraction of the topographic phase, which dominates the unwrapped phase in figure 5.81 results in the differential interferogram, see figure 5.82. Since only a small part of the $[-\pi, +\pi]$ range is used, figure 5.83 shows a scaled-up version of the differential interferogram. The disturbances are mainly lineated features running horizontally over Noord-Holland, and small isolated "humps" over the Noord-oostpolder , Flevoland, and the right side of the image.

The histogram in figure 5.84 reveals the small variance, the rms value is 0.7 rad. The rotationally averaged spectrum in figure 5.85 deviates considerably from the $-5/3$ power law lines.

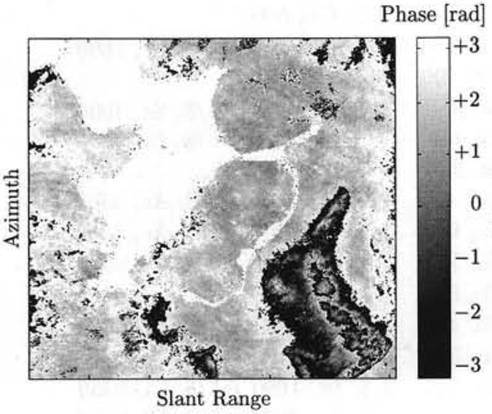

Figure 5.80 *Interferogram fd5*

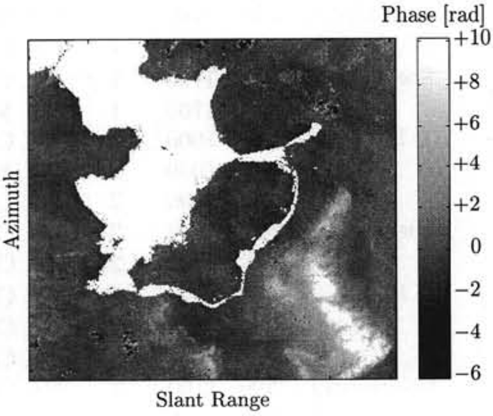

Figure 5.81 *Unwrapped interferogram fd5*

5.4.5.2 Interpretation

The differential interferogram, figure 5.83, is quite undisturbed, ranging from -2 to 1 rad. From the SAR intensity images ice cover over the IJsselmeer is observed.

At day 1, the weather radar does not show precipitation in the area. From Meteosat we find that there are only high and middle level clouds, mostly cirrus. The synoptic data show high relative humidities, and haziness: a reduced visibility to 2–5 km at 10:00, increasing to 6–13 km at 11:00 UTC. The wind is southeast. The current meteorological situation can be called a *frontal jam*, which consists of the weak remains of different frontal systems. In terms of cloud cover we find 6/8–8/8 cover for the whole area, with only middle and high level clouds, see table 5.14. The surface wind field is shown in figure 5.86.

At day 2, the weather radar indicates a large homogeneous rain field with embedded Cb's

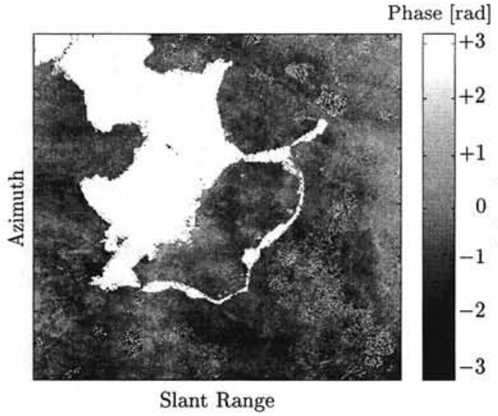

Figure 5.82 *Differential interferogram fd5, in the* $[-\pi, +\pi]$ *range.*

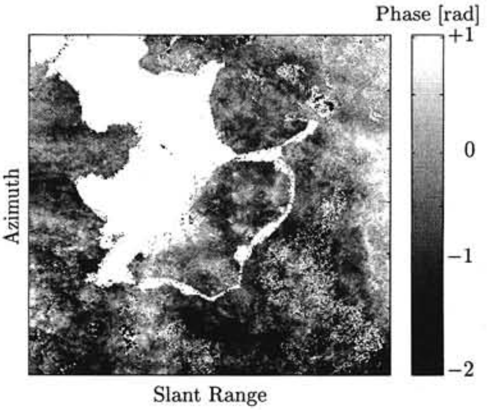

Figure 5.83 *Unwrapped differential interferogram fd5*

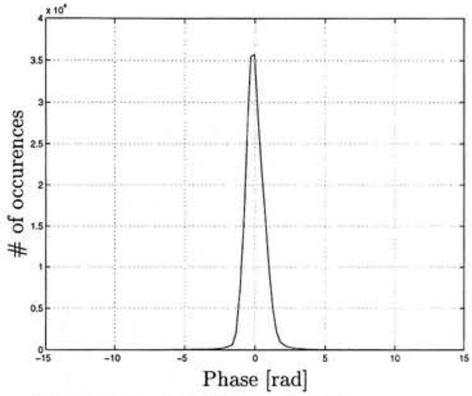

Figure 5.84 *Histogram of a major part of interferogram fd5*

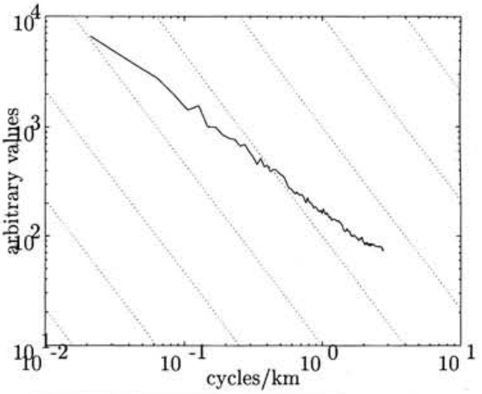

Figure 5.85 *Rotationally averaged spectrum of interferogram fd5*

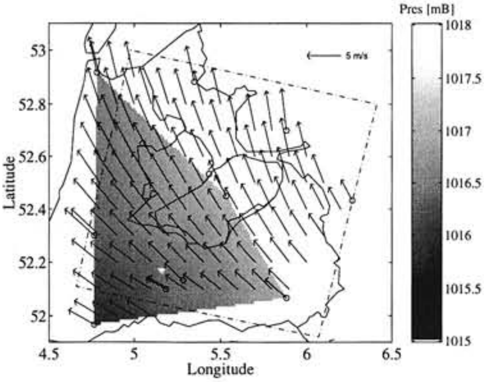

Figure 5.86 *Pressure and surface wind field fd5, day 1, 11:00 UTC*

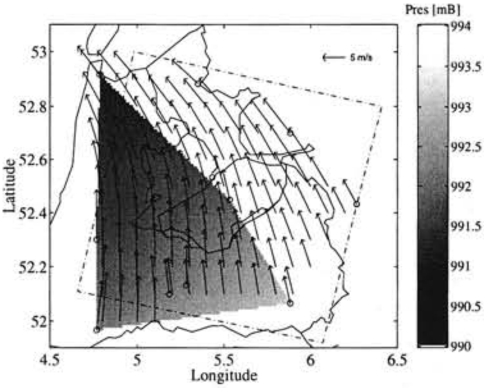

Figure 5.87 *Pressure and surface wind field fd5, day 2, 11:00 UTC*

with tops up to 7 km. This field is covering the whole interferogram. The high tops of the *embedded cumulonimbus* clouds are located over Noord-Holland and southwest Friesland in the interferogram. All synoptic stations indicate medium precipitation in the last hour at 10:00 UTC: 1.8–3.9 mm/hr. This is *homogeneous rain*: all stations report more or less the same. Therefore the effect in the differential interferogram may be small. All stations report 100% relative humidity. At the image acquisition time, it was raining for at least two hours continuously. Cloud cover was 8/8 at 70–100 m. Temperatures were just above the freezing level. The satellite imagery from AVHRR and Meteosat shows a layered, thick cloud cover with sometimes holes in the cirrus layer. The surface wind field is shown in figure 5.87.

Station	#	UTC	Day	Level 1	Level 2	Level 3
De Kooij	235	1000	1	1/8, Cu, 800	5/8, Ac, 3300	7/8, Ci, 8300
Schiphol	240	1000	1	5/8, Ac, 3300	6/8, Ci, 6600	
De Bilt	260	1000	1	2/8, Ac, 3300	7/8, Ci, 8300	
Soesterberg	265	1000	1	2/8, Ac, 3300	5/8, Cs, 6600	5/8, Ci, 8300
Deelen	275	1000	1	1/8, Ac, 3300	7/8, Ci, 8300	
De Kooij	235	1100	1	1/8, Sc, 1000	3/8, Ci, 6600	7/8, Ci, 8300
Schiphol	240	1100	1	1/8, Ac, 3000	6/8, Ac, 3300	8/8, Cs, 8300
De Bilt	260	1100	1	4/8, Ci, 8300	8/8, Cs, 8300	
Soesterberg	265	1100	1	2/8, Ac, 3300	6/8, Cs, 6600	5/8, Ci, 8300
Deelen	275	1100	1	5/8, Ci, 6600	7/8, Ci, 8300	
De Kooij	235	1000	2	2/8, St, 0	7/8, St, 50	7/8, St, 100
Schiphol	240	1000	2	1/8, St, 0	7/8, St, 100	7/8, St, 200
De Bilt	260	1000	2	8/8, St, 0		
Soesterberg	265	1000	2	5/8, St, 100	8/8, St, 200	
Deelen	275	1000	2	5/8, St, 50	8/8, St, 150	
De Kooij	235	1100	2	6/8, St, 50	7/8, St, 100	7/8, St, 200
Schiphol	240	1100	2	3/8, St, 0	7/8, St, 100	8/8, St, 100
De Bilt	260	1100	2	6/8, St, 100	8/8, St, 300	
Soesterberg	265	1100	2	4/8, St, 100	8/8, St, 150	
Deelen	275	1100	2	8/8, St, 50		

Table 5.14 *Cloud observations fd5: 21-12/22-12-1995. The observations give the amount of cloud cover (okta), the type of cloud, and the cloud base at 3 levels. Height is given in meters.*

5.4.5.3 Conclusions

The small phase variations (the humps) in the interferogram are considered to be caused by variations in humidity and rain rates, especially during the second acquisition. The linear horizontal patterns over Noord-Holland align with the wind direction of day 2.

5.4.6 Analysis of interferogram fd6

Interferogram fd6 was acquired at April 4 and 5, 1996, at 10:34:55 UTC (12:34:55 LT). SAR frame number 2547, for ERS-1 orbit 24688, and ERS-2 orbit 5015. The parallel baseline is 26 m, the perpendicular baseline 59 m. Phase unwrapping is performed using the method of Ghiglia and Romero (1994).

5.4.6.1 Observations

Interferogram fd6 is characterized by an organized diagonal wave pattern, covering the whole image, see figure 5.88. Phase unwrapping leads to the absolute interferogram, shown in figure 5.89. The differential interferogram in figure 5.91, where the topographic effect is eliminated, has only small phase variations, with an rms of 0.53 rad, see the histogram in figure 5.94. Although the wave pattern is clearly anisotropic, and therefore this assumption of Kolmogorovs turbulence theory is not fulfilled, a radial averaged spectrum is shown in figure 5.95. A closer look at extraction A in the absolute differential interferogram gives a clear view of the wave pattern, see figure 5.92, and the Radon transform in figure 5.93 indicates the azimuth strike of the waves (125 degrees counterclockwise from the azimuth axis) and the wavelength of 700 m.

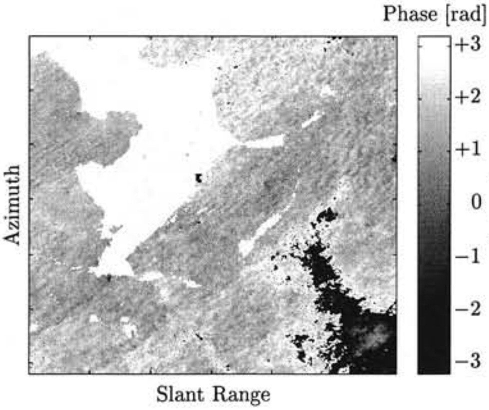

Figure 5.88 *Interferogram fd6*

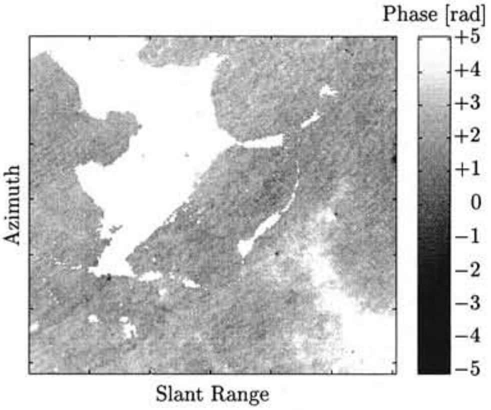

Figure 5.89 *Unwrapped interferogram fd6*

5.4.6.2 Interpretation

A pattern of small waves is observed, with a wavelength of 2 km. Two hypotheses hold for this situation. The first is that the waves are cloud streets, the second assumes that it is connected with moisture under an inversion. When there is vertical circulation in the layer under the inversion, moisture could heap up in the upward moving air. The horizontal diameter of such a upward moving cell is estimated to be approximately equal to the height of the inversion.

At the time of the first image acquisition, the Netherlands are in a high pressure zone. Unfortunately no Meteosat data were available. AVHRR imagery showed no visible clouds. The weather radar did not show any precipitation at both days. At station De Kooy the observers indicated haze, all other stations had good visibility. The air was dry at ground level: relative humidities around 50–60% The wind direction at surface level was east-northeast, and visibility was better than 10 km. It was totally unclouded, although

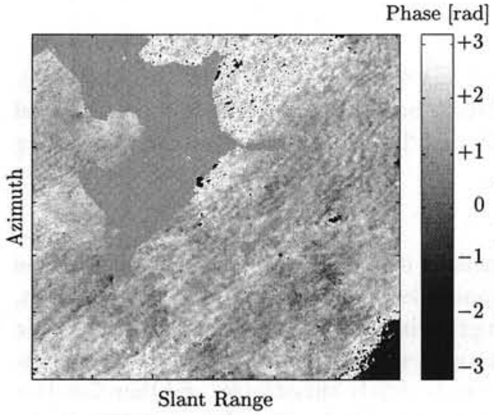

Figure 5.90 *Wrapped differential interferogram fd6*

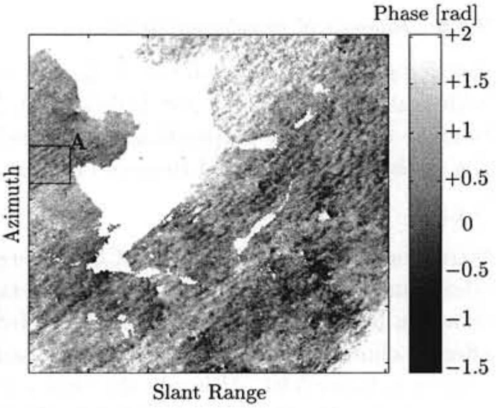

Figure 5.91 *Unwrapped differential interferogram fd6*

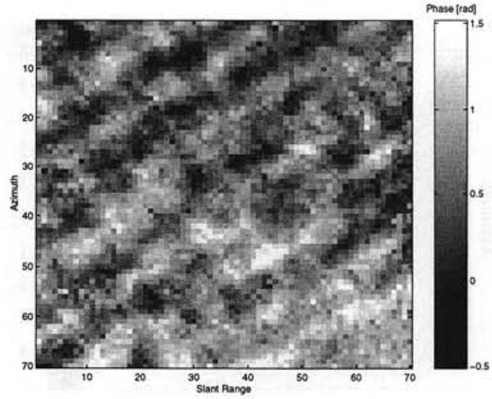

Figure 5.92 *Extraction A of the absolute phase of differential interferogram fd6 in figure 5.91*

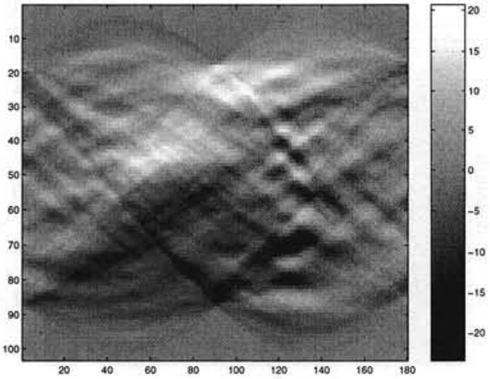

Figure 5.93 *Radon transform of extraction A, showing strong intensity variations at angles of 125 degrees.*

station Deelen reported 6/8 altocumulus at 11:00 UTC. A strong inversion is observed from the radiosonde data, with the inversion base at 2200 m. The wind is backing from the surface (east-northeast) to under the inversion (north-northeast), and is then suddenly veering 90 degrees to east-southeast! This can be labeled as directional wind shear. Surface wind velocities are around 6–8 m/s.

At the second day the weather was cold and dry. There was a fair amount of wind from east-northeast, and according to AVHRR and synoptic data, there was some more cirrus cloud cover, see also table 5.15. The radiosonde profile indicated an inversion at 1000 m. Wind direction (east–east-northeast) and speed did not change considerably over height. Surface wind velocities are equal to the first day, around 6–8 m/s.

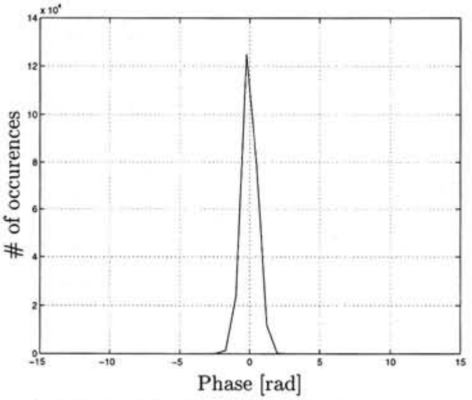

Figure 5.94 *Histogram of a major part of interferogram fd6*

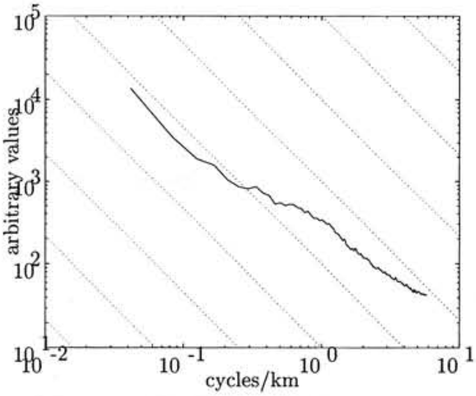

Figure 5.95 *Rotationally averaged spectrum of interferogram fd6*

Station	#	UTC	Day	Level 1	Level 2
De Kooij	235	1000	1		
Schiphol	240	1000	1		
De Bilt	260	1000	1		
Soesterberg	265	1000	1		
Deelen	275	1000	1		
De Kooij	235	1100	1		
Schiphol	240	1100	1		
De Bilt	260	1100	1		
Soesterberg	265	1100	1		
Deelen	275	1100	1	6/8, Ac, 3000 m	
De Kooij	235	1000	2	1/8, Ci, 8300 m	
Schiphol	240	1000	2	2/8, Ci, 8300 m	
De Bilt	260	1000	2	5/8, Ci, 8300 m	
Soesterberg	265	1000	2	6/8, Ci, 10000 m	
Deelen	275	1000	2	6/8, Ci, 8300 m	
De Kooij	235	1100	2	1/8, Ci, 8300 m	
Schiphol	240	1100	2	2/8, Ci, 8300 m	
De Bilt	260	1100	2	1/8, Cu, 1300 m	6/8, Ci, 8300 m
Soesterberg	265	1100	2	6/8, Ci, 8300 m	
Deelen	275	1100	2	7/8, Ci, 8300 m	

Table 5.15 *Cloud observations fd6: 04-04/05-04-1996. The observations give the amount of cloud cover (okta), the type of cloud, and the cloud base at 2 levels.*

5.4.6.3 Conclusions

The stripes in the interferogram have a north to northeast direction. Two explanations are: (1) directional wind shear at day 1 due to the sudden change in wind direction around the inversion, (2) moisture streets due to moisture circulation under the inversion. Due to the fact that the waves are bulged, which is not expected for a plain wave phenomenon, the moisture street hypothesis seems to be more likely.

5.4.7 Analysis of interferogram fd7

Interferogram fd7 was acquired at June 13 and 14, 1996, at 10:35:04 UTC (12:35:04 LT). SAR frame number 2547, for ERS-1 orbit 25690, and ERS-2 orbit 6017. The parallel baseline is 45 m, the perpendicular baseline 77 m. Phase unwrapping is performed using the minimal cost flow algorithm (Costantini, 1996). There were no precise state vectors available for the ERS-1 orbit, which made a manual correction for the orbit errors necessary.

5.4.7.1 Observations

Interferogram fd7 has phase variations of two phase cycles, see figure 5.96 for the interferogram, and figure 5.97 for the unwrapped interferogram. The differential interferogram, shown in figure 5.99, reveals that although some topography caused this phase variation, the maximum variation is still two phase cycles. The rms of the variation is 1.7 rad, see the histogram in figure 5.100. The signature of the variation varies from small waves in the upper left corner of the interferogram to artifacts with larger dimensions (max. diameter around 20 km) over Flevoland and in the lower right corner. The rotationally averages log-log spectrum in figure 5.101 shows a $-5/3$ power law for wavelengths between 400 m and 3.3 km, and between 15 and 30 km.

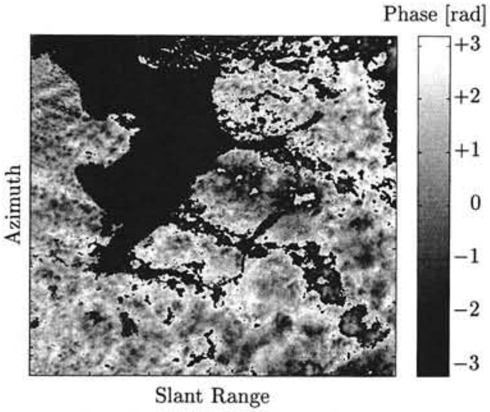

Figure 5.96 *Interferogram fd7*

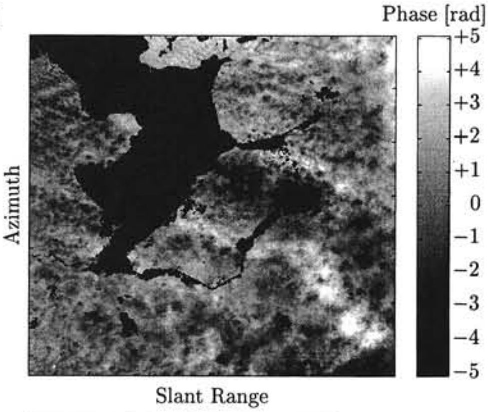

Figure 5.97 *Unwrapped interferogram fd7*

5.4.7.2 Interpretation

The pattern of phase behavior shows clearly small laminar structures in the west which grow more turbulent in diameter and magnitude towards the east. This corresponds clearly with the prevailing wind direction, see figure 5.102. NOAA's AVHRR shows at day 1 northwestern winds, with cloud streets which grow bigger, starting just after reaching the coast. The cloud street patterns can be clearly associated with the phase variation in the interferograms. The Meteosat visual channel shows the same type of cloud patterns, though with less resolution. The synoptic data of day 1 indicate cumulus clouds. The relative humidity lies between 40–50% and temperatures vary between 16–19°C.

At day 2, there is a weak cold front over the Netherlands. There are some cumuli, combined with stratocumulus and cirrus. Relative humidity is 50–60%, temperature 13–16°C. AVHRR confirms these observations.

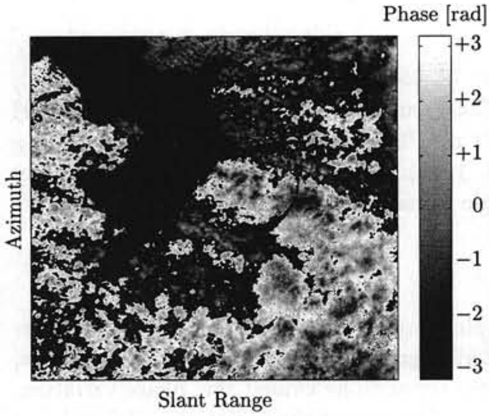

Figure 5.98 *Wrapped differential interferogram fd7*

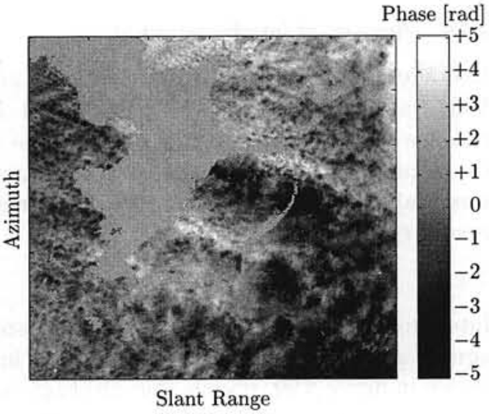

Figure 5.99 *Unwrapped differential interferogram fd7*

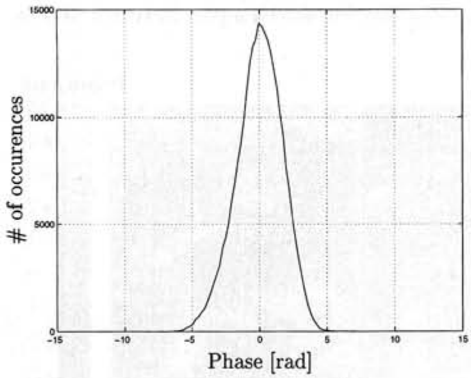

Figure 5.100 *Histogram of a major part of interferogram fd7*

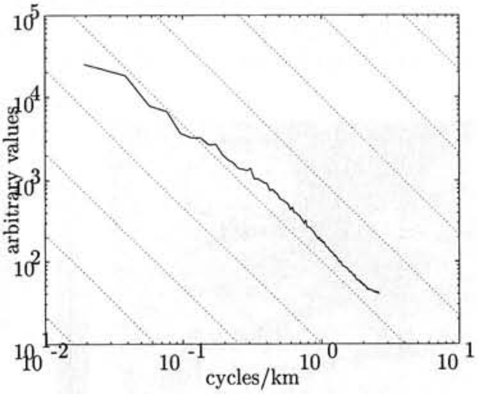

Figure 5.101 *Rotationally averaged spectrum of interferogram fd7*

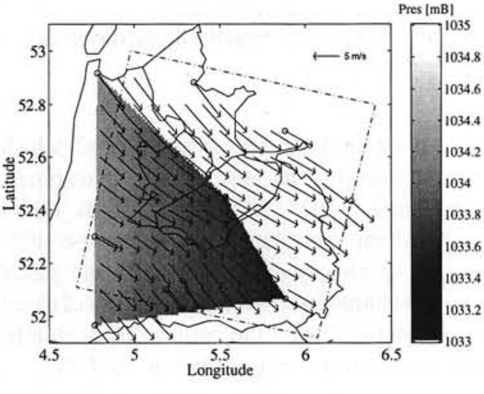

Figure 5.102 *Pressure and surface wind field fd7, day 1*

The inversion height in De Bilt at day 1 is 2000 m, and 1200 m at day 2. On the first day the cloud layer under the inversion is not very thick yet, the second day it clearly gets thicker. We see from the radiosondes that there must be a cirrus layer over Emden. From the synoptic data we see that this is also reported in De Bilt.

Station	#	UTC	Day	Level 1	Level 2	Level 3
De Kooij	235	1000	1	1/8, Cu, 650		
Schiphol	240	1000	1	2/8, Cu, 1300		
De Bilt	260	1000	1	3/8, Cu, 1100		
Soesterberg	265	1000	1	3/8, Cu, 1500		
Deelen	275	1000	1	5/8, Cu, 1600		
De Kooij	235	1100	1	1/8, Cu, 650		
Schiphol	240	1100	1	2/8, Cu, 1400		
De Bilt	260	1100	1	3/8, Cu, 1100		
Soesterberg	265	1100	1	4/8, Cu, 1600		
Deelen	275	1100	1	3/8, Cu, 1600	3/8, Sc, 3000	
De Kooij	235	1000	2	2/8, Cu, 800	5/8, Cu, 1300	
Schiphol	240	1000	2	2/8, Cu, 1000	6/8, Sc, 1300	
De Bilt	260	1000	2	6/8, Cu, 1000	5/8, Ci, 8300	
Soesterberg	265	1000	2	2/8, Cu, 1200		
Deelen	275	1000	2	2/8, Cu, 1000	7/8, Sc, 1300	
De Kooij	235	1100	2	2/8, Cu, 850	6/8, Cu, 1300	
Schiphol	240	1100	2	1/8, Cu, 800	3/8, Cu, 1000	6/8, Sc, 1300
De Bilt	260	1100	2	3/8, Cu, 1000		
Soesterberg	265	1100	2	2/8, Cu, 1200	5/8, Sc, 1500	
Deelen	275	1100	2	2/8, Cu, 1000	6/8, Sc, 1400	

Table 5.16 *Cloud observations fd7: 13-06/14-06-1996. The observations give the amount of cloud cover (okta), the type of cloud, and the cloud base at 3 levels. Height is given in meters.*

5.4.7.3 Conclusions

Based on the AVHRR observations of day 1, the wind speed and direction, and the radiosonde data, it is clear that the phase variation in the differential interferogram is caused by cloud streets, transporting moisture from the North-Sea to the inland. The observed low relative humidities at the surface indicate that the moisture variations occur at some height, presumably just below the inversion height.

5.5 Analysis Flevoland ascending

The interferograms *Flevoland ascending-north* and *Flevoland ascending-south* cover a large part of the Netherlands. Since the Flevoland polder is situated near the center of the combined interferograms, both areas are referred to by that name. The northern image just extends from the first of the *Frisian islands*, *Texel*, in the north-west, to the *Veluwe* hills in the south-east. A 30 km long dike, the *Afsluitdijk*, spans the distance between the provinces *Noord-Holland* and *Friesland*, at the west and east side of the *IJsselmeer* respectively. The southern image covers a land area with the provinces *Utrecht*, *Gelderland*, *Overijssel* and *Limburg*, as well as a part of Germany, see figure 5.103.

A large number of synoptic stations is used for the analysis of the interferograms. These stations are listed in figure 5.103. More or less regularly divided over the area, cloud observations are available from civil and military air fields, and the main meteorological station in *De Bilt*. Radiosonde observations are available from the De Bilt station and from the Belgian station *Ukkel* and the German station *Emden*, shown in figure 3.1.

Apart from topographic heights in the *Veluwe* area, some topography can be found in the eastern and south-eastern parts of interferogram area *fa-s*, and in the German areas in the interferogram. Since no reference elevation model was available from the German areas, this area is not included in the analysis.

5.5.1 Analysis of interferogram fa1

Interferogram fa1 was acquired at August 29 and 30, 1995, at 21:41:08 UTC, equivalent to 23:41:08 LT. SAR frame numbers 1053 and 1035 are used, for ERS-1 orbit 21560, and ERS-2 orbit 1887. The parallel baseline changed from −30 to −31 m, the perpendicular baseline from −79 to −80 m, for the southern and northern image respectively. The phase unwrapping is performed using the minimal cost flow algorithm (Costantini, 1996).

5.5.1.1 Observations

Interferogram fa1, see figure 5.104, is combined of two SAR frames, taken directly after each other in the same orbit. The frames were fitted together to form one, 100 × 200 km frame. This larger area gives some more specific detail of a different scale of atmospheric phenomena. Unwrapping of the interferogram gives figure 5.106. The phase varies over a range of a little more than one cycle, and a large "ridge" seems to cross the interferogram in the azimuth direction. Elimination of the topographic phase is performed in the differential interferogram, see figure 5.106. Note that the used reference DEM did not cover the whole area: the lower right corner, delimited by the line in the figure, still has some topographic phase signatures. This area is excluded from further analysis.

Characteristic of this differential interferogram is the ridge along azimuth direction, which affects the lower part as well as the upper part of the interferogram. Furthermore, small wave features are observed at different small areas in the interferogram. The wave direction is more or less in azimuth direction (−16 degrees w.r.t. the north), the wavelength is around 1 km, and the amplitude is less than 2 rad. A strong isolated artifact is located in the upper left part of the interferogram. A zoom of this area is shown in figure 5.107. This is a very localized artifact—it fits within a rectangle of 8 × 16 km—with a maximum phase difference of 8 rad (1.3 phase cycles). A horizontal cross section of this phenomenon is plotted in figure 5.108.

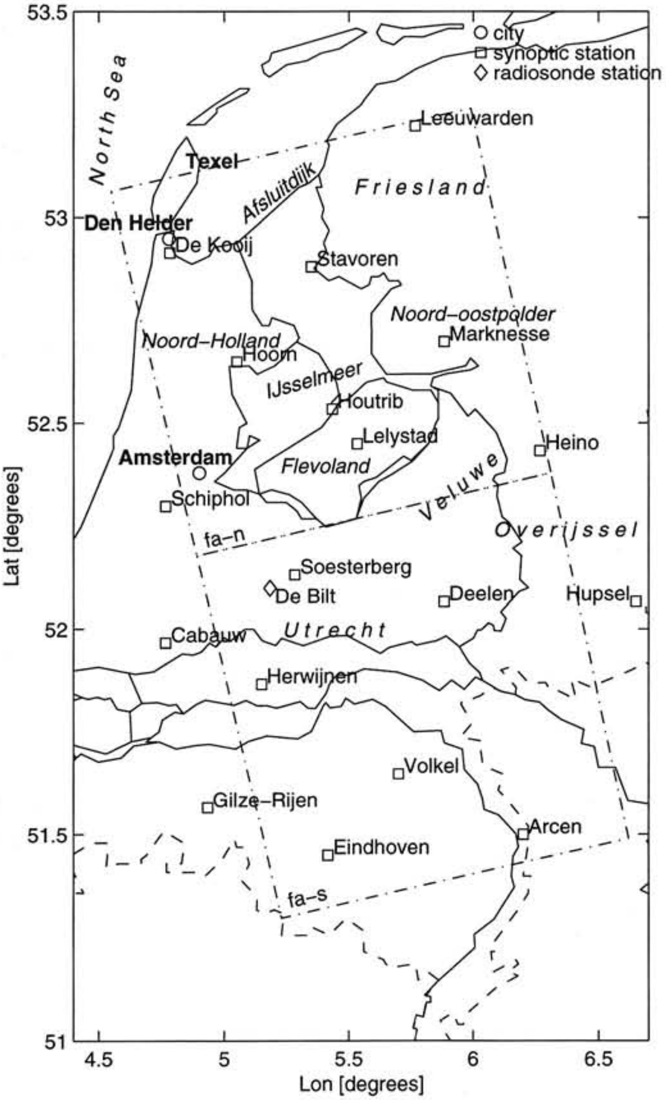

Figure 5.103 *Map of the area for the combined interferograms Flevoland ascending, showing the position of the synoptic and radiosonde stations with some relevant topographical information, referred to in the text.*

The overall phase statistics of the differential interferogram are analyzed, producing the histogram shown in figure 5.109. The overall rms is 2 rad. Note that the histogram is slightly divided as a consequence of lacking phase information over water areas. The rotationally averaged spectrum is shown in figure 5.110. The overall angle of the spectrum is not parallel with the $-5/3$ lines, although for wavelengths between 10 and 25 km it is nearly at this angle.

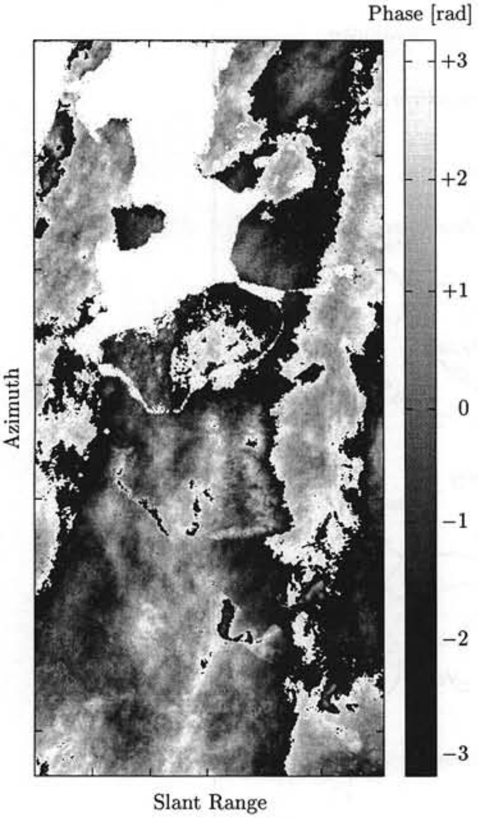

Figure 5.104 *Interferogram fa1*

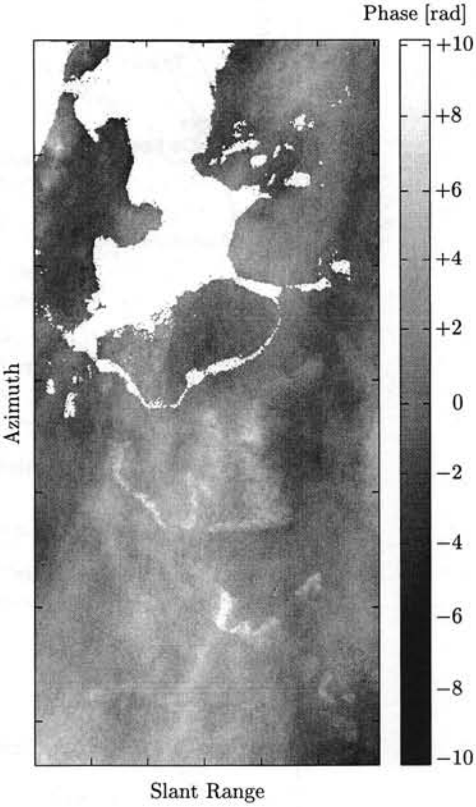

Figure 5.105 *Unwrapped interferogram fa1*

5.5.1.2 Interpretation

Possible atmospheric observations in this area include (1) the ridge in azimuth direction, (2) a localized anomaly in the north-western part of the interferogram, under the city of Den Helder, (3) a band of decreased coherence over Noord-Holland (not shown here), (4) footprints over water areas of active rain cells in the intensity image of day 2, and (5) some "humps" in the southern interferogram.

AVHRR imagery is not available for the times of the SAR acquisitions, which are acquired late in the evening. Images of 3–4 hours earlier show some broken cumulus clouds at day 1, and a warm front connected with a band of cloud cover approaching from the northwest at day 2.

At day 1, there is a northwesterly flow behind a cold front passage, in which showers are

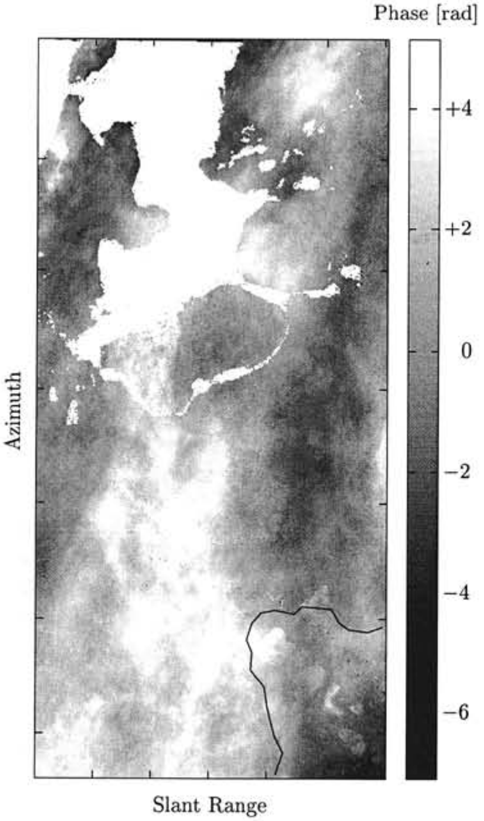

Figure 5.106 *Unwrapped differential interferogram fa1*

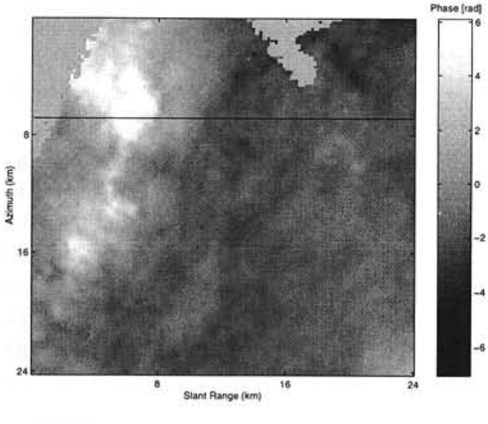

Figure 5.107 *Extraction of the selected part of interferogram fa1*

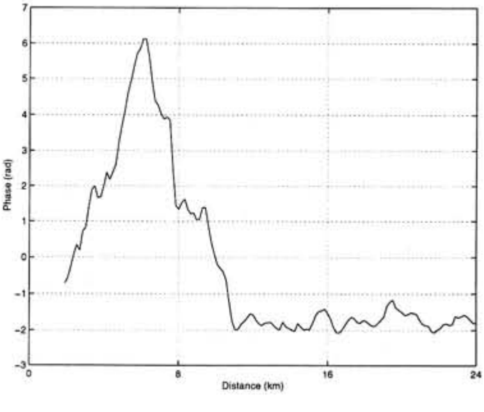

Figure 5.108 *Horizontal cross section of the anomaly in figure 5.107*

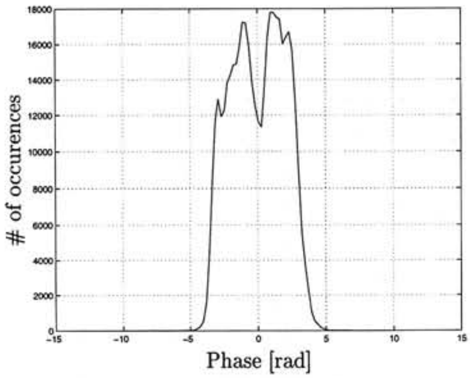

Figure 5.109 *Histogram of a major part of interferogram fa1*

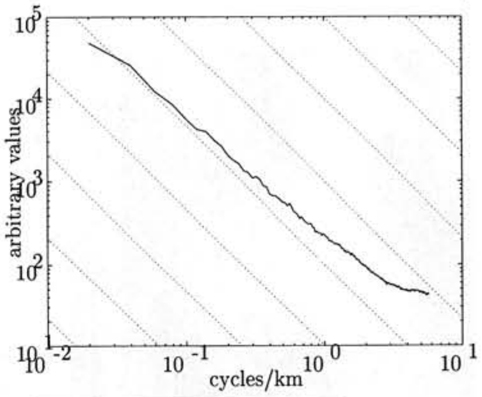

Figure 5.110 *Rotationally averaged spectrum of interferogram fa1*

likely, coming from the North-Sea. Behind the front, in the area of the interferogram, there is advection of unstable, polar air. It is the end of August, late in the evening: therefore the sea is still quite warm which may cause showers in the coastal areas in the evening. As a result, some cumulonimbus clouds are expected. The probability of showers is decreasing from the northwestern to the southeastern part of the image.

The weather radar for the first day, see figure 5.111, indicates isolated showers over Noord-Holland, over the Afsluitdijk, and over Zuid-Flevoland, with heights up to 4.5 km. These are also visible in the interferogram. A comparison of the weather radar with the southern interferogram is hard to perform, since only very small and localized rain signals are detected by the radar. At day 1, De Kooij reports a shower, northwestern winds, a relative humidity of 80% and a temperature of 10–14°C. Most of the synoptic stations report cumulus,stratocumulus, and altocumulus, see table 5.17. Note that the localized artifact under Den Helder is identified in shape as well as in magnitude as a rain cell by the weather radar.

Since the local artifact has the same phase sign as the "ridge" over the whole image, this is either a delay effect at day 1, or a relative advance in day 2. This last option is true when there is an area with, e.g., less moisture inside a relatively homogeneous area with more moisture. This seems not very likely in this case.

At day 2 there is still advection of cold air in the lower layers of the atmosphere. The extension of a ridge of high pressure over the Netherlands provides subsidence at higher levels.[5] There are a few showers, according to weather radar observations, only in the southwestern part of the country. The cloud cover varies quite strong, and there is good visibility (> 15 km). Some stations, such as Amsterdam and Gilze-Rijen, have had a shower. Stations in the northwest report cumulus clouds, in the center stratocumulus, and in the south stratocumulus and cumulonimbus, see table 5.17. It is likely that at the time of the SAR acquisition most of the area is dry; only Amsterdam could have had a light shower.

---

[5] Subsidence causes downward movements in which the air dries out and the temperature increases, which makes the atmosphere less unstable. In this case the subsidence inversion at day 2 is at 4500 m.

Station	#	UTC	Day	Level 1	Level 2	Level 3
De Kooij	235	2100	1	1/8, Cu, 800		
Schiphol	240	2100	1	1/8, Cu, 1100	4/8, Sc, 1600	
De Bilt	260	2100	1	1/8, Cu, 900		
Soesterberg	265	2100	1	3/8, Sc, 1600	3/8, Ac, 3000	
Leeuwarden	270	2100	1	1/8, Cu, 1300		
Deelen	275	2100	1	1/8, Ac, 3000		
Gilze-Rijen	350	2100	1	1/8, Cu, 1600	3/8, Ac, 3000	
Eindhoven	370	2100	1	2/8, Sc, 1600		
Volkel	375	2100	1	5/8, Ac, 3000		
De Kooij	235	2200	1	1/8, Cu, 900	3/8, Ac, 3000	
Schiphol	240	2200	1	1/8, Cb, 1000	4/8, Sc, 3000	
De Bilt	260	2200	1	1/8, Sc, 1400	3/8, Ac, 3000	
Soesterberg	265	2200	1	1/8, Sc, 1300	5/8, Ac, 3000	
Leeuwarden	270	2200	1	1/8, Cu, 1300		
Deelen	275	2200	1	1/8, Ac, 3000		
Gilze-Rijen	350	2200	1	1/8, Cb, 1100	3/8, Ac, 3000	
Eindhoven	370	2200	1	2/8, Cu, 1600	3/8, Ac, 3000	
Volkel	375	2200	1	4/8, Ac, 3000		
De Kooij	235	2100	2	1/8, Cu, 650	7/8, Sc, 1500	
Schiphol	240	2100	2	2/8, Cu, 1000	7/8, Sc, 1600	
De Bilt	260	2100	2	3/8, Sc, 1500		
Soesterberg	265	2100	2	1/8, Sc, 1600	3/8, Ci, 8300	
Leeuwarden	270	2100	2	1/8, Cu, 1000		
Deelen	275	2100	2	1/8, Ac, 3300		
Gilze-Rijen	350	2100	2	1/8, Sc, 1600	3/8, Sc, 3000	
Eindhoven	370	2100	2	1/8, Sc, 3000		
Volkel	375	2100	2	1/8, Cu, 1600		
De Kooij	235	2200	2	1/8, Cu, 800	3/8, Sc, 1100	6/8, Sc, 1600
Schiphol	240	2200	2	1/8, Cu, 800	7/8, Sc, 1300	
De Bilt	260	2200	2	1/8, Cu, 800	7/8, Sc, 1600	
Soesterberg	265	2200	2	4/8, Sc, 3000	5/8, Ci, 8300	
Leeuwarden	270	2200	2	1/8, Sc, 1600		
Deelen	275	2200	2	1/8, Ac, 3300		
Gilze-Rijen	350	2200	2	1/8, Cu, 800	1/8, Cb, 900	3/8, Sc, 1100 5/8, Ac,3000
Eindhoven	370	2200	2	1/8, Sc, 3000		
Volkel	375	2200	2	2/8, Cu, 1000		

Table 5.17 *Cloud observations fa1: 29-08/30-08-1995. The observations give the amount of cloud cover (okta), the type of cloud, and the cloud base at 3 or 4 levels. Height is given in meters.*

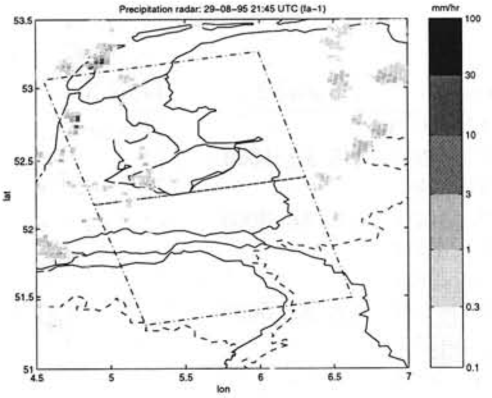

Figure 5.111 *Weather radar image for interferogram fa1*

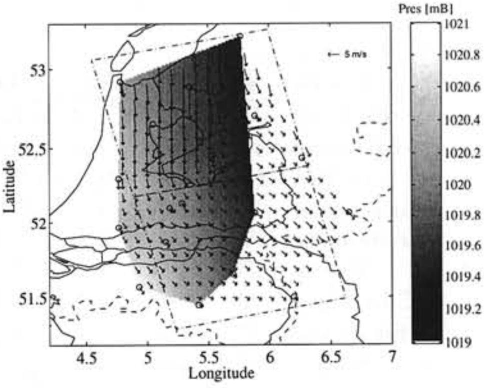

Figure 5.112 *Pressure and surface wind field fa1, day 1*

5.5.1.3 Conclusions

The local anomalies in the interferogram fit very well with showers at day 1. This also harmonizes with the derived meteorological situation. Based on its orientation, the ridge could be part of the warm front at day 2. However, in that case it should be a decrease in refractivity, which seems unlikely based on the relative homogeneity of the surrounding phase. The alignment of the ridge with the surface wind field at day 1, makes an explanation in terms of a field of increased humidity more likely. In this field, precipitation occurs at some parts.

5.5.2 Analysis of interferogram fa2

Interferogram fa2 was acquired at October 3 and 4, 1995, at 21:41:14 UTC (22:41:14 LT). SAR frame numbers are 1053 and 1035, for ERS-1 orbit 22061, and ERS-2 orbit 2388. The parallel baseline is 144 and 146 m, the perpendicular baseline 385 and 393 m, for the southern and the northern image respectively. The phase unwrapping is performed using the minimal cost flow algorithm (Costantini, 1996).

5.5.2.1 Observations

Interferogram fa2 in figure 5.113 is again a composition of two neighboring SLC scenes. The whole interferogram shows several fringes, not only at the expected topographic features. Particularly striking is the diagonal line or wave crest, which is crossing both original images. The unwrapped interferogram in figure 5.114 is somewhat easier to interpret. Due to the cut-off boundaries of the used color scale, topography is clearly visible in the center and lower left of the image. In the differential interferogram, figure 5.115, this topography has been removed using the reference DEM, up to the lower right corner, which was not covered by the elevation model.

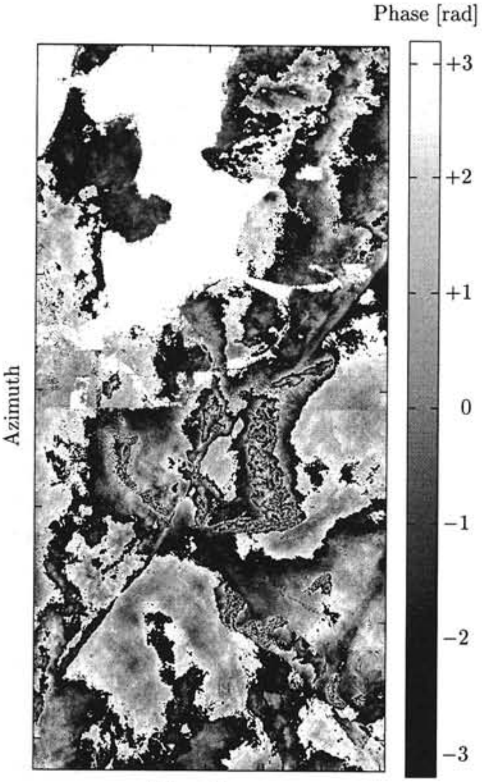

Figure 5.113 *Interferogram fa2*

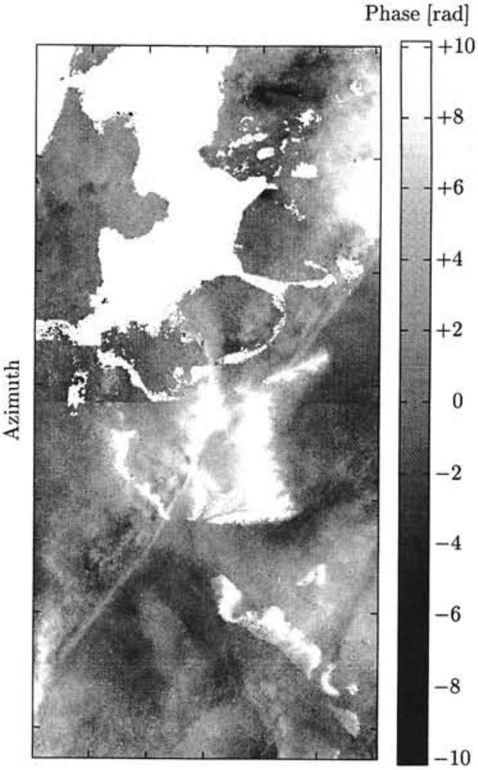

Figure 5.114 *Unwrapped interferogram fa2*

In the differential interferogram, the most prominent feature is the white diagonal crest, corresponding with a very local increase in absolute phase. In the lower part of this crest, the side left of the crest seems to have some stronger phase turbulence when compared to the right side. Two boxes, located at both side of the crest, indicated in figure 5.115 are analyzed using the rotationally averaged spectrum, see figure 5.116. Box 1 is at the left side of the crest, box 2 at the right side. It can be concluded that both lines have the same orientation, although the stronger amplitude differences in the left box result in a vertical shift of the line in the spectrum.

Some cross sections of the crest are shown in figures 5.117, 5.118, and 5.119. In profile 1, the lowest indicated in figure 5.115, the crest has an amplitude which is 3 rad higher than the average left side of the profile, and 5 rad higher than the right side. The wave crest itself is approximately 4 km wide. In the middle of the interferogram, the crest seems to split into two branches. The main branch deviates towards the left side of the image, and forms a curl. Profile 2 in figure 5.118 shows a cross section of this middle part of the crest, where it has the largest amplitude, and starts deviating towards the left side of the image. The maximum amplitude of the wave is here 13.1 rad. The difference with the left side the the profile is 9 rad, and with the right side of the profile even 14 rad! The width of the wave is 5 km. The second branch continues in the same direction as the lower part, accompanied at the left side by a parallel second wave crest. A third profile, in this area, is shown in figure 5.119. The maximum of the tops is 4.3 and 3.7 rad, while there is still the difference with the left side of the profile (1 rad) is smaller than the difference with the right side (4 rad). The width of both wave crests is approximately 2 km.

Apart from this wave crest phenomenon, still rather large phase deviations characterize the northern parts of the interferogram. A larger cross section over this area, profile 4, is shown in figure 5.120. In these parts, phase variations of 15 rad take place, where the anomalies have a typical diameter of 10 km.

The histogram of the total image, shown in figure 5.121, gives a wide spread curve, consisting of two main peaks. Most of the interferometric phase is located in a range of 18 rad. The rms value of this distribution is 3.6 rad, although it could be argued that the rms values of the two main Gaussians in the histogram would be less.

The rotational averaged spectral lines for two parts of the interferogram are shown in figure 5.122. The lower line is found for an area in the lower part of the interferogram, and includes the crest. This line deviates from the $-5/3$ slope, apart from a small range of long wavelengths. The upper line results from an area in the upper right corner of the interferogram, where the phase variation is quite strong. This line closely follows the $-5/3$ slope, for almost all wavelengths between 500 m and 30 km.

5.5.2.2 Interpretation

There are local anomalies in both images. A dominant wave crest crosses both images from the northeast to the southwest. It is only a couple of kilometers wide.In the upper right part of the interferogram there is also anomalous undulation.

The crest is related to the cold front which passes over the Netherlands. Since the average tangent of the angle of a cold front is 1/70, horizontal changes occur over relatively short distances when compared with a warm front, see figure 5.123. There can suddenly be less precipitation when the front passes over. This phenomenon is a Narrow Cold-Frontal Rainband (NCFR), or *line convection*, (Parsons, 1992).

The weather charts at day 1 show a curve in a polar front, which is moving over the area.

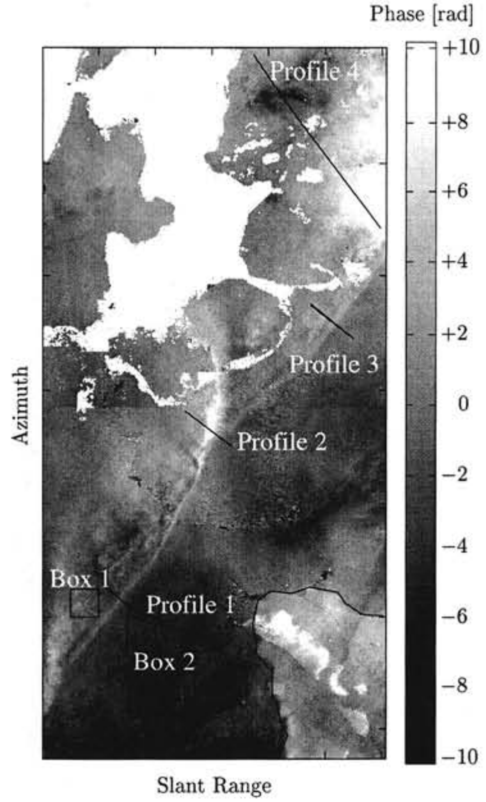

Figure 5.115 *Unwrapped differential interferogram fa2*

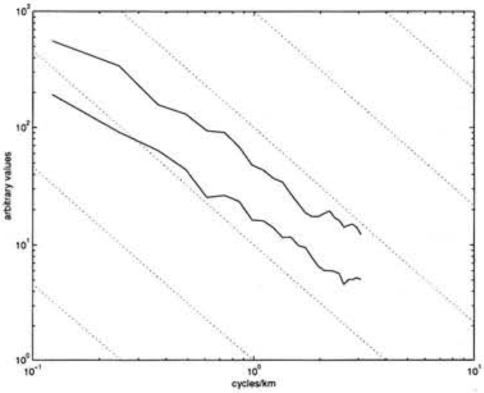

Figure 5.116 *Rotationally averaged spectrum for the two boxes, left and right of the wave crest in fa2. The upper line corresponds with the box left of the crest.*

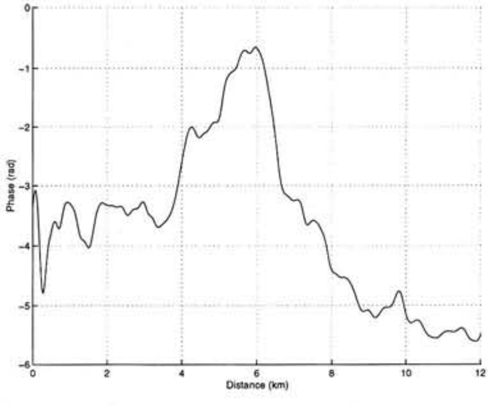

Figure 5.117 *Profile 1 of fa2*

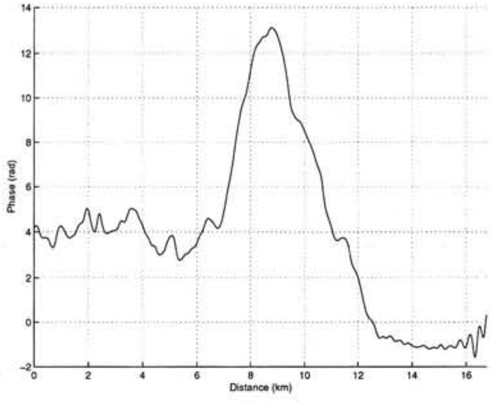

Figure 5.118 *Profile 2 of fa2*

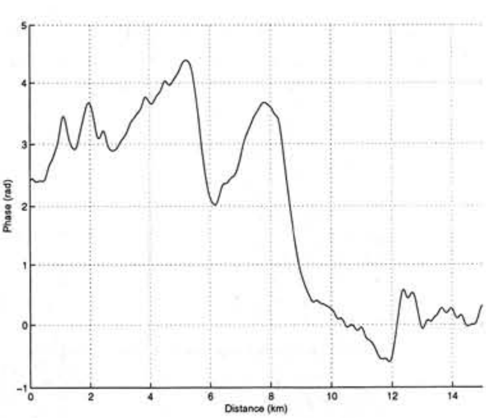

Figure 5.119 *Profile 3 of fa2*

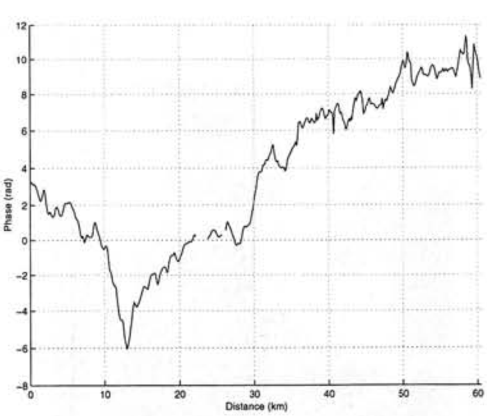

Figure 5.120 *Profile 4 of fa2*

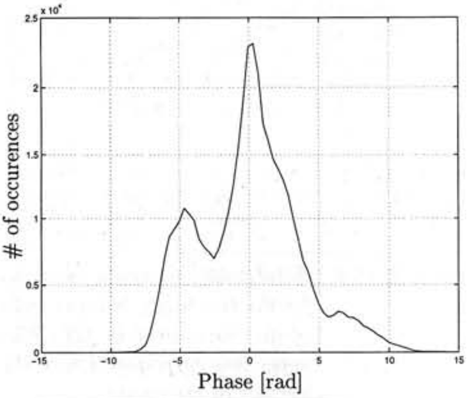

Figure 5.121 *Histogram of major part of interferogram fa2. The two Gaussians are the result of the average difference between the phase at the left side of the diagonal crest and at the right side.*

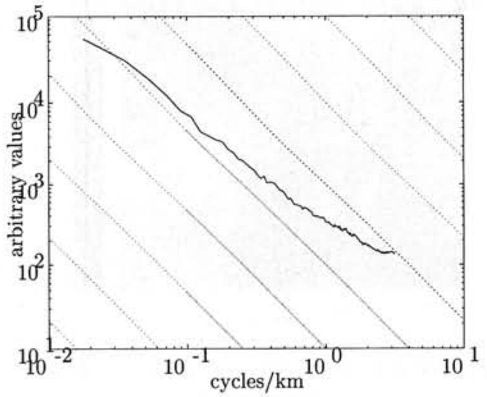

Figure 5.122 *Rotationally averaged spectrum of fa2. The upper line is found for an area around the crest, at the lower part of the interferogram. The lower line results from an analysis of the upper right part of the image.*

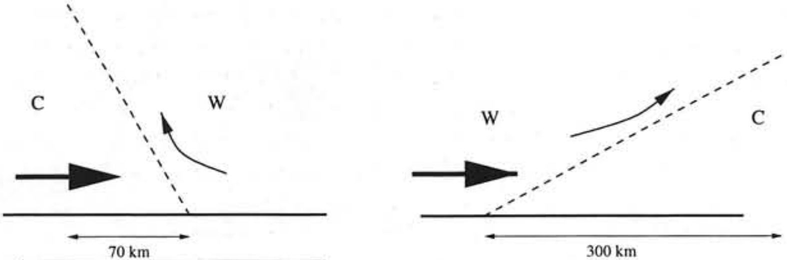

Figure 5.123 *The average gradient for a cold front is 1/70, which is much steeper compared to a warm front, with an average gradient of 1/300*

The wave top (position of the occlusion point) is just over Friesland. The cold front has a northeast-southwest orientation. The cold front could be a split-level cold front, see figure 5.130. The synoptic weather features are rain, showers and thunderstorms.

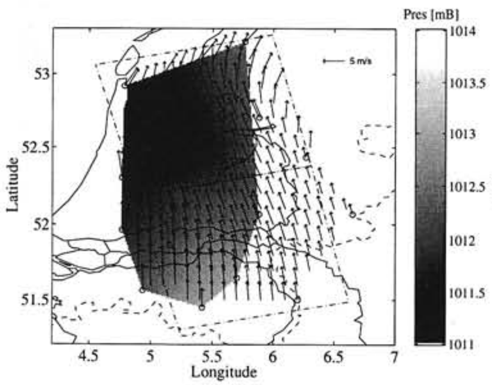

Figure 5.124 *Pressure and surface wind field fa2, day 1,21:00 UTC*

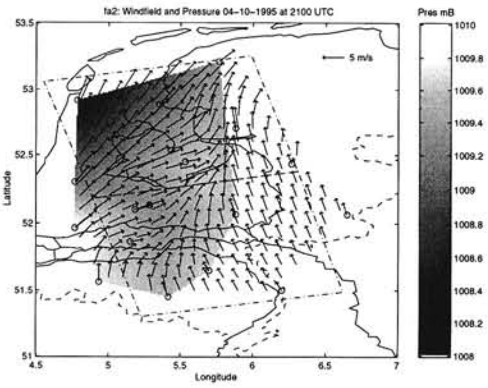

Figure 5.125 *Pressure and surface wind field fa2, day 2, 21:00 UTC*

At day 2, the weather charts of 12:00 UTC (daily overviews), indicate that the cold front is still situated over the southeastern part of the Netherlands. Northwest of the front, our research area , there still some showers and rain. A second cold front is approaching behind the first one. It is probably this second cold front which is located over the Netherlands at the time of the SAR acquisitions.

The weather radar image of the first day indicates a thunderstorm over Friesland with cloud tops at 8 km. The position of the showers at the first day, see figure 5.126, corresponds closely with the position of the negative phase anomaly in the interferogram. De Kooy also has a thunderstorm with tops on 8 km. The second day, figure 5.127 the weather radar shows a large sickle shaped form of rain over Flevoland. This sickle is also clearly visible in the interferogram. The cloud cover consists of layered clouds with embedded cumulonimbus.

At day 1, a large part of the synoptic stations is still situated at the warm side of the cold front. De Kooy and Leeuwarden are at the warm side of the front. At 10:00 UTC, De Kooy reports lightning, but no rain. It has rained, however, 4.4 mm in the last hour. Leeuwarden has a thunderstorm, with 5.3 mm precipitation and a visibility of 1800 m, which is very low. Lelystad has 0.1 mm precipitation. At 11:00 UTC, De Kooy reports a thunderstorm with rain and wind from the south-southeast. Also Schiphol reports rain. Leeuwarden reports a heavy thunderstorm, with 13.2 mm precipitation, and southwestern wind! Eindhoven observes rain in the distance. There is a changing cloud cover in the area, see table 5.18. Cloud cover observations at 21:00 UTC show cumulonimbus clouds over the middle and northern part of the area, with additional stratocumulus and altocumulus. The southern stations report altocumulus and cirrus. There is southwestern wind at higher altitudes, and southeastern wind at surface level, according to the radiosonde observations. At 22:00 UTC, cumulonimbus clouds are observed in the north. In the south of the Netherlands it looks like nothing is happening.

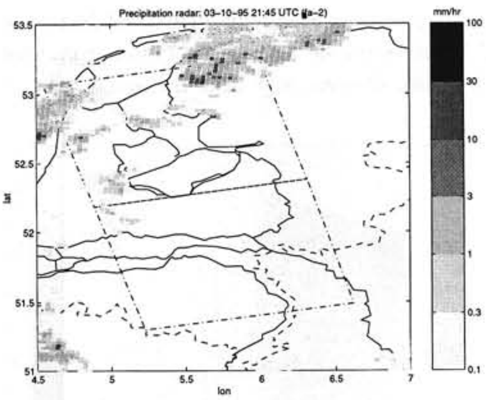

Figure 5.126 *Weather radar fa2, day 1*

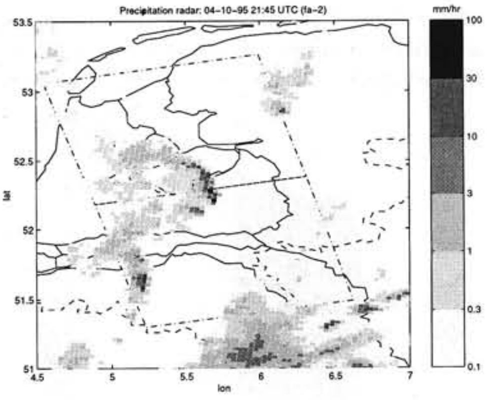

Figure 5.127 *Weather radar fa2, day 2*

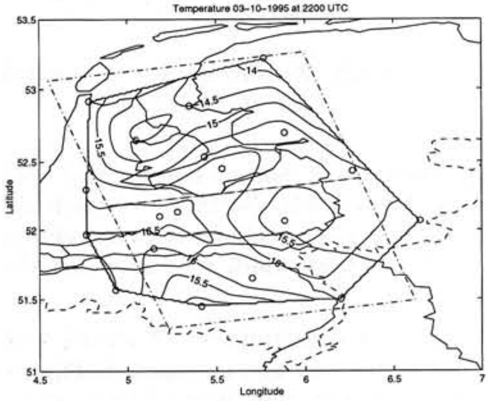

Figure 5.128 *Temperature contours fa2, day 1*

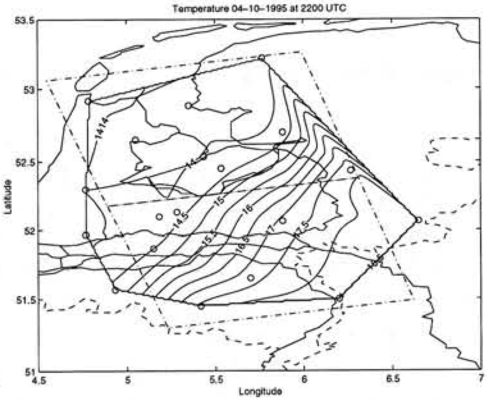

Figure 5.129 *Temperature contours fa2, day 2*

The synoptic data at day 2, 21:00 UTC, list for De Kooy light rain and southern winds and for Schiphol light rain. Houtrib has had a light shower in the last hour. Leeuwarden reports drizzle. In the south, the stations have seen lightning, but did not have precipitation. The front has moved now, over the south-east of the Netherlands. The wind in that area is south-east, between 230–260 degrees. The northwest part of the Netherlands indicate wind from the southwest!

Cloud observations at day 2, 21:00 UTC, indicate cumulonimbus over Amsterdam, stratocumulus over the center of the area, and altocumulus at the southeast. At 22:00 UTC, there was a thunderstorm in the southwest. The total cloud cover was 7/8–8/8. There are no more cumulonimbus clouds observed between 21:00 and 22:00.

5.5.2.3 Conclusions

The data indicate clearly that the wave crest in the interferogram is closely related with the cold front. Figure 5.130 describes this configuration. The left subfigure gives a side-view of the split-level cold front. At some altitude, there is a south-western wind, according to the radiosonde. At surface level up to 1800 m the wind is more south to south-east (synoptic data). The frontal plane (the diagonal line in the right subfigure) is splitting up, and the 'height-cold front' is moving towards the north-east. The 'surface cold front' is nearly stationary. Behind the height-cold front the air dries up: in the De Bilt radiosonde we observe the dry part of the profile between 2 and 5 km. The air below and above this region has a relative humidity of 100%. The right subfigure shows the two combined interferograms, with the front depicted as the fat dashed line. We divide the area in three parts: Part I is behind the front, part II is the warm sector, and part III is the frontal zone. At day 2, area II is warmer (17–18°C) , more humid, and has more low and layered clouds than area I, where it is colder (14°C) , and there are higher clouds. The temperature differences are clearly notable from the synoptic data. In area III, a higher pressure is expected just behind the frontal zone, where there is also a sudden drop of temperature.

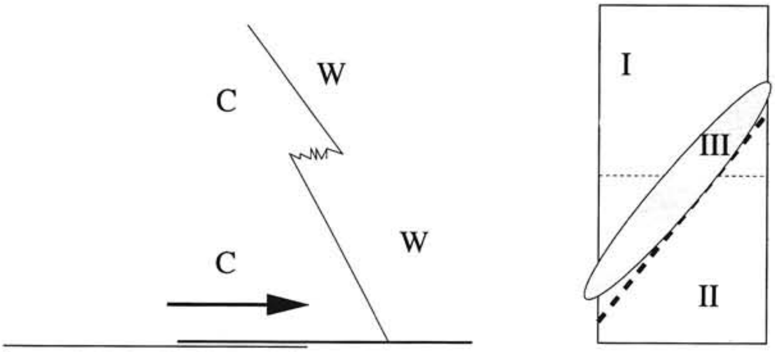

Figure 5.130 *A split-level front. The surface front is nearly stationary, the upper-level front is pushed forward by winds at this altitude. The right figure shows the location of the crest, see the text for the discussion on the three areas.*

The hypotheses of relating the features in the interferogram to a frontal system seems to be confirmed by the meteorological feature of the split-level front with a high intensity of precipitation (thunderstorms) and a remarkable drying out of a layer behind the upper level cold front.

Station	#	UTC	Day	Level 1	Level 2	Level 3
De Kooij	235	2100	1	1/8, St, 200	1/8, Cb, 500	7/8, Sc, 900 7/8, Ac, 3000
Schiphol	240	2100	1	1/8, Cb, 1300	3/8, Sc, 3000	7/8, Ci, 6600
De Bilt	260	2100	1	6/8, Sc, 1600		
Soesterberg	265	2100	1	3/8, Sc, 1000	6/8, Sc, 1600	7/8, Ac, 3300
Leeuwarden	270	2100	1	3/8, St, 200	2/8, Cb, 400	4/8, Sc, 650 6/8, Sc, 1500
Deelen	275	2100	1	3/8, Sc, 1600	5/8, Ci, 8300	
Gilze-Rijen	350	2100	1	1/8, Ac, 3300	3/8, Ci, 8300	
Eindhoven	370	2100	1	1/8, Cu, 1400	4/8, Ac, 3300	7/8, Ci, 8300
Volkel	375	2100	1	4/8, Sc, 1000	6/8, Ci, 8300	
De Kooij	235	2200	1	1/8, Cu, 1000	4/8, Ac, 3000	7/8, Ac, 3300
Schiphol	240	2200	1	1/8, Sc, 1300	3/8, Ac, 3000	7/8, Ci, 6600
De Bilt	260	2200	1	6/8, Sc, 1600		
Soesterberg	265	2200	1	3/8, Sc, 1600	4/8, Ac, 3000	6/8, Ac, 3300
Leeuwarden	270	2200	1	1/8, Cb, 500	5/8, Sc, 750	7/8, Sc, 1300
Deelen	275	2200	1	2/8, Sc, 1600		
Gilze-Rijen	350	2200	1	2/8, Ac, 3300		
Eindhoven	370	2200	1	2/8, Ac, 3300		
Volkel	375	2200	1	2/8, Ac, 3300		
De Kooij	235	2100	2	1/8, Cu, 1200	6/8, Ac, 3000	8/8, Ac, 3000
Schiphol	240	2100	2	2/8, Cb, 800	5/8, Sc, 1300	
De Bilt	260	2100	2	4/8, Sc, 1100	4/8, Ac, 3300	
Soesterberg	265	2100	2	3/8, Cu, 800		
Leeuwarden	270	2100	2	1/8, Cu, 900	4/8, Sc, 1100	6/8, Sc, 3000
Deelen	275	2100	2	1/8, Ac, 3000	3/8, Ac, 3300	7/8, Ci, 8300
Gilze-Rijen	350	2100	2	1/8, Cu, 300	5/8, Ac, 3000	7/8, Ci, 8300
Eindhoven	370	2100	2	2/8, Ac, 3000	6/8, Ci, 8300	
Volkel	375	2100	2	3/8, Ac, 3000	5/8, Ac, 3300	
De Kooij	235	2200	2	1/8, Cu, 1200	5/8, Ac, 3000	8/8, Ac, 3000
Schiphol	240	2200	2	1/8, Cu, 800	7/8, Ac, 3000	
De Bilt	260	2200	2	8/8, Sc, 1000		
Soesterberg	265	2200	2	1/8, Cu, 700	3/8, Sc, 3000	8/8, Ac, 3000
Leeuwarden	270	2200	2	1/8, Sc, 1200	5/8, Sc, 1600	7/8, Ac, 3300
Deelen	275	2200	2	3/8, Ac, 3000	5/8, Ac, 3300	7/8, Ci, 8300
Gilze-Rijen	350	2200	2	1/8, Sc, 1100	5/8, Ac, 3000	8/8, Ac, 3300
Eindhoven	370	2200	2	3/8, Ac, 3000	7/8, Ac, 3300	
Volkel	375	2200	2	4/8, Ac, 3000	7/8, Ac, 3300	

Table 5.18 *Cloud observations fa2: 03-10/04-10-1995. The observations give the amount of cloud cover (okta), the type of cloud, and the cloud base at 3 or 4 levels. Height is given in meters.*

5.5.3 Analysis of interferogram fa3

Interferogram fa3 was acquired at March 26 and 27, 1996, at 21:41:05 UTC (22:41:05 LT). SAR frame numbers 1053 and 1035 are used, for ERS-1 orbit 24566, and ERS-2 orbit 4893. The parallel baseline is −21 and −21 m, the perpendicular baseline −32 and −33 m, for the southern and northern image respectively. The method of Ghiglia and Romero (1994) is used for the phase unwrapping.

5.5.3.1 Observations

After correcting for possible orbit errors in interferogram fa3—mainly a first order tilt in slant range direction—an exceptionally strong phase ramp remains at the lower part of the southern interferogram, see figure 5.131 and figure 5.132. The ramp is covering 1.5 fringe. Since the effect is only covering the lower half of the interferogram, orbit errors seem unlikely to cause this, especially because the top interferogram does not show this effect at all. Tests with independently calculated precise orbits of DEOS-TUD and DLR-GFZ yielded identical results. On the other hand, the effect seems to be very systematic, and can be modeled well using a third degree polynomial over the lower parts of the lower image, see figure 5.133. Therefore the assumption that it is purely of atmospheric origin

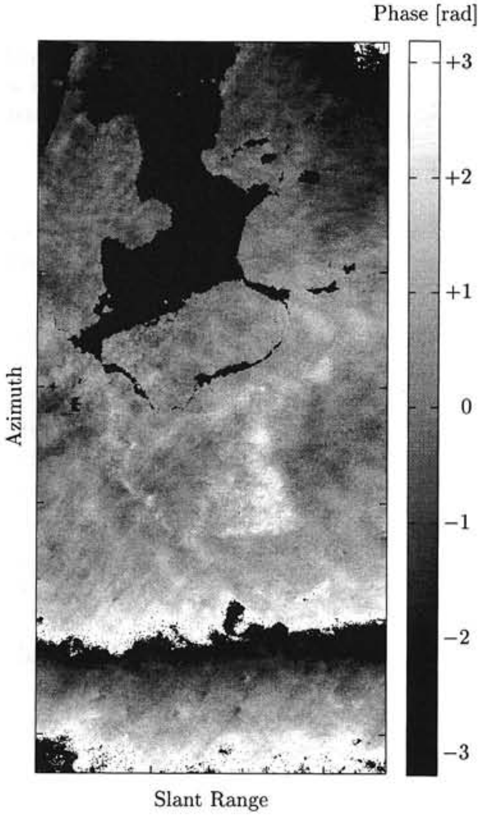

Figure 5.131 *Interferogram fa3*

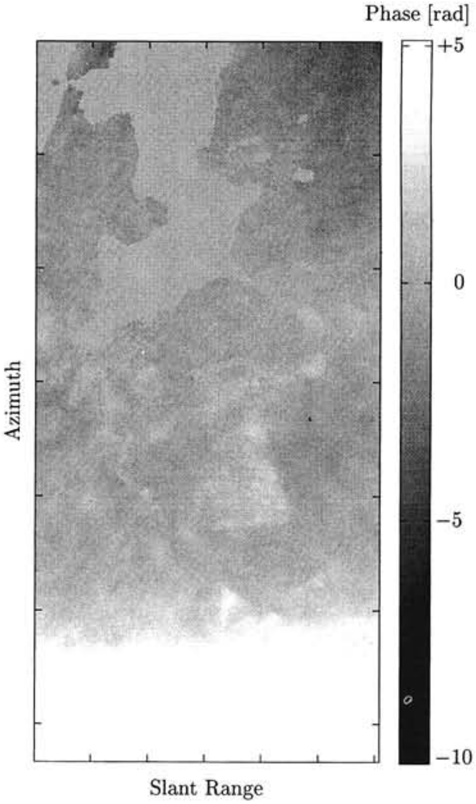

Figure 5.132 *Unwrapped interferogram fa3*

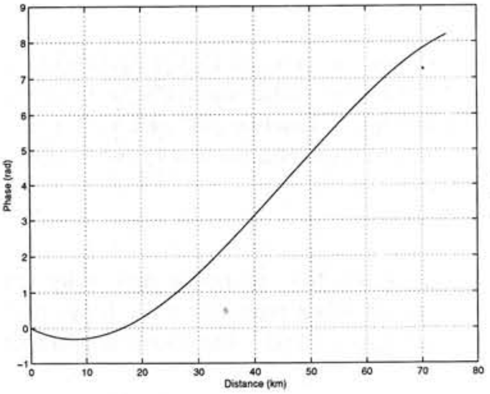

Figure 5.133 *The third degree polynomial ramp, which was extracted from the lower side of interferogram fa3*

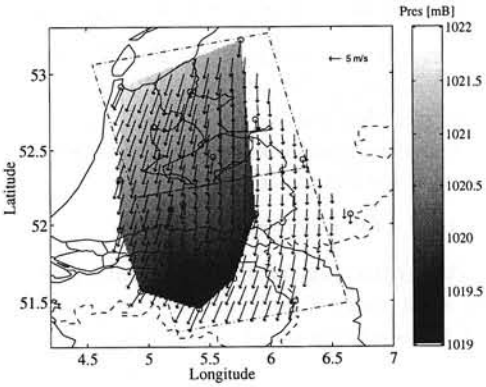

Figure 5.134 *Pressure and surface wind field fa3, day 1, 22:00, showing a change from north to northwest over the interferogram area.*

raises some questions as well. For this reason, both the original differential interferogram (figure 5.135) is shown, as well as a version in which the ramp is modeled by a third degree polynomial, and extracted from the interferogram, see figure 5.136.

Whereas in the uncorrected version the ramp dominates the behavior of the interferometric phase, the corrected version shows much more detail, and low amplitude phase effects. A histogram of combined parts of the interferogram, not including the ramp area, is shown in figure 5.137. A rotationally averaged spectrum is shown in figure 5.138. Note that this spectrum is calculated over a relatively large region, enabling longer wavelengths to be present in the plot. The curve deviates considerably from the $-5/3$ gradient, indicated by the dotted lines.

An overall rms value, including the ramp area, of 2.5 rad was found. More localized statistics were checked as well for this interferogram. An area of 24×24 km in Noord-Holland had only small phase deviations with Gaussian characteristics, and an rms of 0.36 rad. An area of the same size in the east of the Netherlands had an rms of 0.46 rad, in the north 0.68 rad, and in the west 0.46 rad.

5.5.3.2 Interpretation

Observed phase variations include slight humps, a strong third order gradient, and waves in the south-western part of the image. In the water of the IJsselmeer, wind strokes are visible. These wind strokes are probably connected with the waves in the southern image, wind rolls, causing moisture streets under the subsidence inversion, see Hanssen et al. (1998a) for a more elaborate discussion. The strong gradient in the southern image can be related with a frontal zone.

From the Meteosat WV channel, figure 5.140 it may be concluded that at day 1, 21:30 UTC, there is a jet stream flowing over the Netherlands, at about 10 km height. However, this is not confirmed by the radiosondes of De Bilt and Emden: at day 1 there are thick cirrus layers, cirrostratus, but the wind speed at higher levels is not very high. Still,

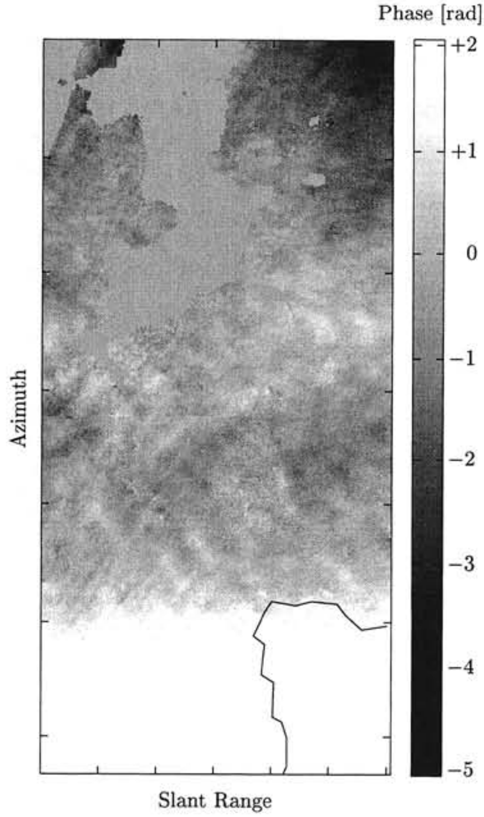

Figure 5.135 *Unwrapped differential interferogram fa3, topographic phase is eliminated*

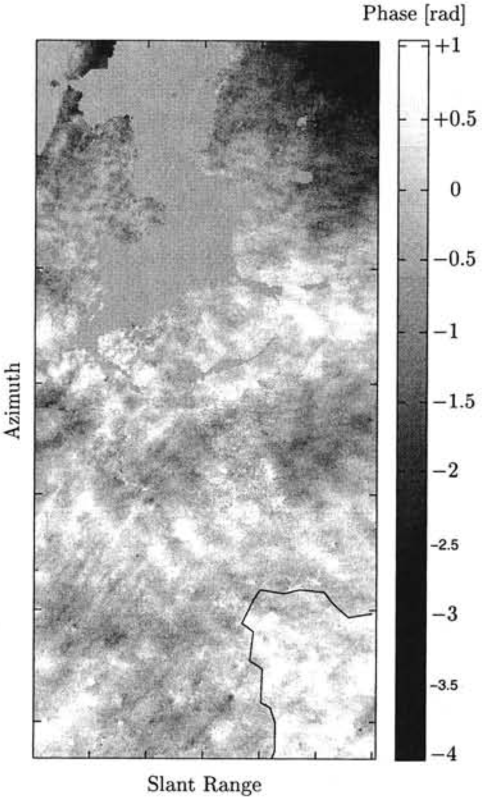

Figure 5.136 *Unwrapped differential interferogram fa3, after elimination of the ramp*

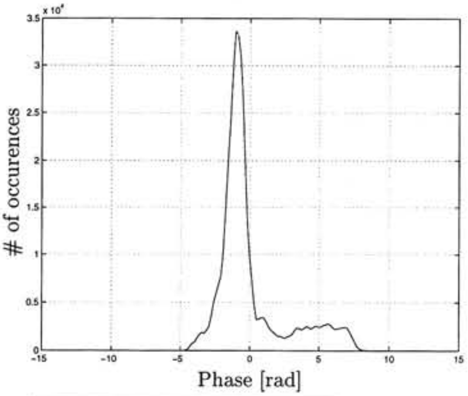

Figure 5.137 *Histogram of a major part of interferogram fa3*

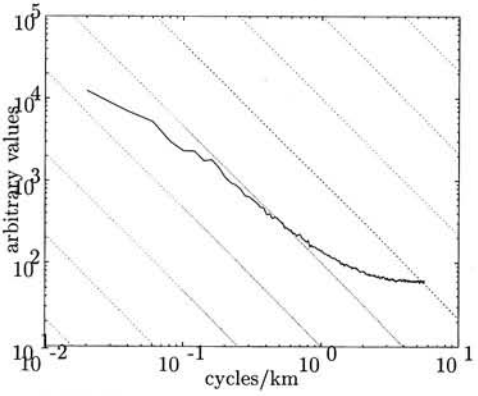

Figure 5.138 *Rotationally averaged spectrum of fa3*

there is a lot of water vapor available at higher levels. The extension of a ridge of high pressure provides subsidence and that's the reason why the WV-image of the Meteosat gives a dry stroke in the Netherlands. Note that the pixels in the water vapor image yield the integrated water vapor content of the troposphere at a certain position. This could be an explanation for the strong gradient in the southern interferogram. The water vapor instrument measures the absorption spectrum of water vapor from the top of the troposphere down to approximately 3 km.

At day 1, a cold front has recently passed from the north. During the passage of the front there are several cloud layers, middle to heigh clouds, but there is no precipitation. There is advection of cold air.

At day 2, the Meteosat IR channel indicates cold cirrus clouds over the North Sea. Cloud cover has moved towards the south.

The synoptic data at day 1, 21:00, show there is a north-northeastern wind: 7.7–10 m/s, see figure 5.134. There is only few cloud cover, only Volkel (375) and Eindhoven (370) report more than 2/8 octa. In Leeuwarden the temperature is below zero, in all other stations it is 2–3°C. The most observed cloud type is stratocumulus, with a coverage of 2/8–3/8 octa. Note that there is more cloud cover reported over the southern part of the image, just as expected from the interferogram. There is no precipitation. At 22:00 UTC, the cloud conditions are similar, with no precipitation.

At day 2, the situation is almost similar: The rain radar shows no true precipitation signal, only some erroneous scattering. This was a very 'nice' day, regarding the time of the year. The wind direction was west in De Kooy and north in Schiphol. There was, however, not much wind. The visibility was very good. Cloud cover at 21:00 UTC was 7/8 in total, see table 5.19: with stratocumulus in the northeast and cirrus in the northern part of the area. The higher clouds that are visible in the Meteosat IR image are already observed as the first signs of a warm front, which is invading the northwest of the Netherlands the next day.

5.5.3.3 Conclusions

The strong gradient of more than a full cycle in the south of the interferogram seems to be very systematic, which raises some doubt if it is caused by atmosphere or if it is, e.g., a processing error. However, based on the Meteosat observations of integrated water vapor, combined with synoptic cloud observations and the direction of the cold front at day 1, the gradient can be explained sufficiently as a gradient in integrated water vapor.

Observed wind strokes over the IJsselmeer, the synoptic wind direction observations, and the direction of the waves in the southern part of the interferogram reveal the same direction. The interferometric effects are probably caused by the distribution of moisture in boundary layer rolls.

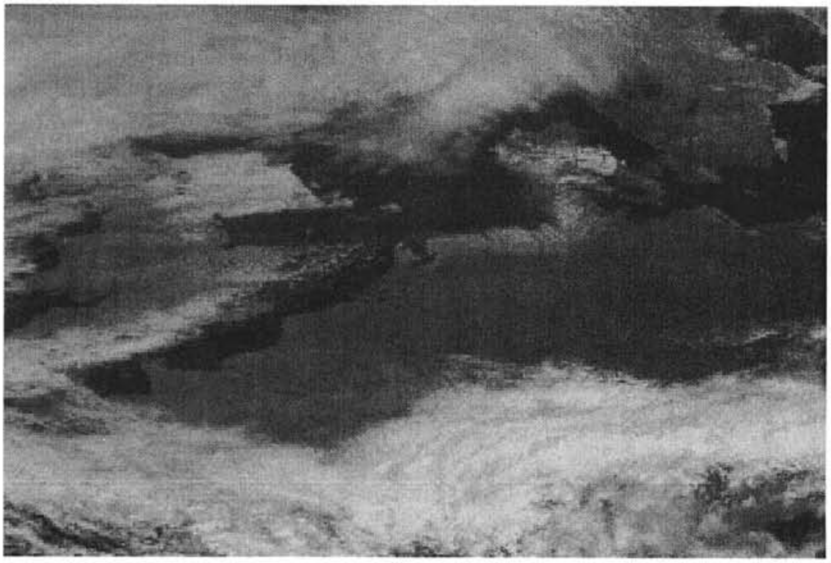

Figure 5.139 *Meteosat visual channel fa3, day 2. This image serves as an orientation tool for the water vapor gradient in figure 5.140*

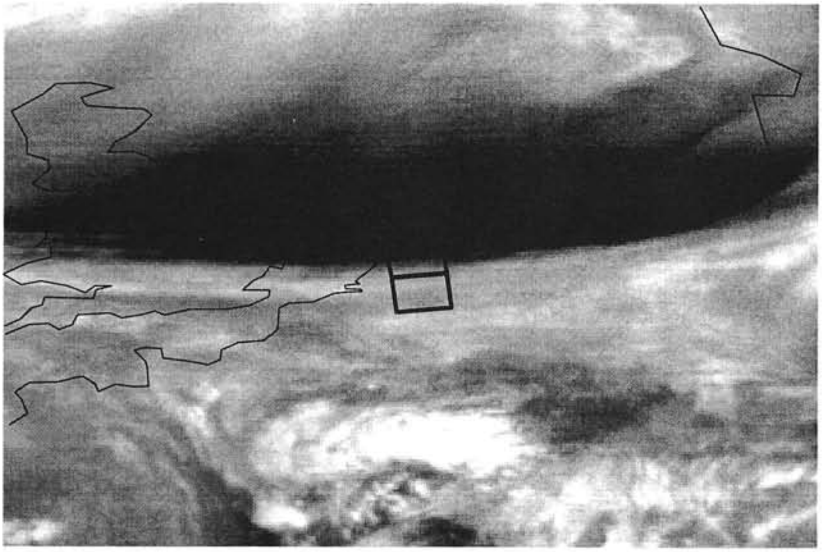

Figure 5.140 *Meteosat water vapor channel fa3, day 1, 21:30 UTC. A strong increase in integrated water vapor can be observed over the south of the Netherlands. Refer to figure 5.139 for orientation. The two rectangles indicate the position of the interferogram.*

Station	#	UTC	Day	Level 1	Level 2	Level 3
De Kooij	235	2100	1	2/8, Sc, 700		
Schiphol	240	2100	1	1/8, Sc, 1000	3/8, Sc, 1200	
De Bilt	260	2100	1	5/8, Sc, 1500		
Soesterberg	265	2100	1	1/8, Sc, 1100	3/8, Sc, 1300	
Leeuwarden	270	2100	1	1/8, Sc, 1100		
Deelen	275	2100	1			
Gilze-Rijen	350	2100	1	1/8, Cu, 500	3/8, Sc, 900	7/8, Sc, 1100
Eindhoven	370	2100	1	8/8, Sc, 1100		
Volkel	375	2100	1	3/8, Sc, 1300	6/8, Sc, 3000	
De Kooij	235	2200	1	2/8, Sc, 800		
Schiphol	240	2200	1	2/8, Sc, 1000	6/8, Sc, 1200	
De Bilt	260	2200	1	1/8, Cu, 650	4/8, Sc, 1500	
Soesterberg	265	2200	1	1/8, Sc, 1000	3/8, Sc, 1200	
Leeuwarden	270	2200	1	1/8, Sc, 1100		
Deelen	275	2200	1			
Gilze-Rijen	350	2200	1	3/8, Sc, 1000	7/8, Sc, 1400	
Eindhoven	370	2200	1	8/8, Sc, 1100		
Volkel	375	2200	1	4/8, Cu, 1300		
De Kooij	235	2100	2	5/8, Ci, 8300		
Schiphol	240	2100	2	2/8, Ci, 8300		
De Bilt	260	2100	2	1/8, Ci, 8300		
Soesterberg	265	2100	2	1/8, Ci, 8300		
Leeuwarden	270	2100	2	4/8, Sc, 1300	7/8, Ci, 8300	
Deelen	275	2100	2			
Gilze-Rijen	350	2100	2	1/8, Ci, 8300		
Eindhoven	370	2100	2	2/8, Ci, 8300		
Volkel	375	2100	2			
De Kooij	235	2200	2	5/8, Cs, 6600	7/8, Ci, 8300	
Schiphol	240	2200	2	7/8, Cs, 8300		
De Bilt	260	2200	2	6/8, Ci, 8300		
Soesterberg	265	2200	2	3/8, Ci, 8300		
Leeuwarden	270	2200	2	1/8, Sc, 1300	5/8, Ac, 3300	8/8, Ci, 8300
Deelen	275	2200	2			
Gilze-Rijen	350	2200	2	1/8, Ci, 8300		
Eindhoven	370	2200	2	1/8, Ci, 8300		
Volkel	375	2200	2			

Table 5.19 *Cloud observations fa3: 26-03/27-03-1996. The observations give the amount of cloud cover (okta), the type of cloud, and the cloud base at 3 levels. Height is given in meters.*

5.5.4 Analysis of interferogram fa4

Interferogram fa4 was acquired at April 30 and May 1, 1996, at 21:41:04 UTC, or 23:41:04 LT. SAR frame number 1053 and 1035, for ERS-1 orbit 25067, ERS-2 orbit 5394. The parallel baseline is −30 and −31 m, the perpendicular baseline −57 and −59 m, for the southern and the northern image respectively. Phase unwrapping was performed using the method of Ghiglia and Romero (1994).

5.5.4.1 Observations

In interferogram fa4, shown in figure 5.141, two fringes can be observed. Phase unwrapping produces the unwrapped interferogram, as shown in figure 5.142. The main topography is removed using the reference DEM, and after correcting for the main linear phase ramps in slant range and azimuth direction, the differential interferogram is obtained, as shown in figure 5.143. It is clear that the main disturbance in this interferogram consists of a large anomaly which extends from the south of the lower image to well into the upper image, half way in Flevoland. Furthermore, there is a negative disturbance in the upper left of the image, and a positive one in the middle of the left side.

The histogram over the major part of the differential interferogram is shown in figure 5.145. The overall rms value is 1.3 rad. Figure 5.146 shows the rotationally averaged spectrum, which follows the −5/3 gradient for wavelengths between 8 and 25 km.

5.5.4.2 Interpretation

There are disturbances along the coast, and there is an extended anomaly over Flevoland, starting at the southern image. In the coherence image (not shown here), loss of coherence is observed along the coast and in Friesland.

Day 1 is an extension of a ridge of high pressure, which should not yield much weather activity. However, at day 2 a weak cold front located over the eastern part of the Netherlands, is moving to the west. Precipitation associated with this cold front may have influence on the interferogram.

At day 1 the weather radar does not give any signal in our test area. At day 2, however, it is clearly visible how a large band with precipitation correlates with the "intrusion" over Utrecht and Flevoland, cf. figure 5.144. This rain band can be described as *showery precipitation*, associated with a weak cold front with not very large cumulonimbus clouds, cloud tops are observed up to 5 km. Note that even the curvature in the southern interferogram correlates very well with the curvature in the image of the weather radar of day 2.

The synoptic observations day 1 indicate that there is a considerable amount of cloud cover and good visibility. At 21:00 there is mostly stratocumulus and high altocumulus, see table 5.20. In the center of the area, altocumulus and cirrus are observed. The southern stations observe stratocumulus and altocumulus.

At day 2, 21:00 UTC, some precipitation is reported in Leeuwarden. The other stations did not have much precipitation. At 22:00 UTC, Leeuwarden had light rain and Volkel had a small shower.

There seems to be a contradiction here between the weather radar at day 2, and the synoptic observations at that day. It is, however, likely that the precipitation that is seen by the radar does not reach the surface. Volkel, e.g., does not have much rain. Thus,

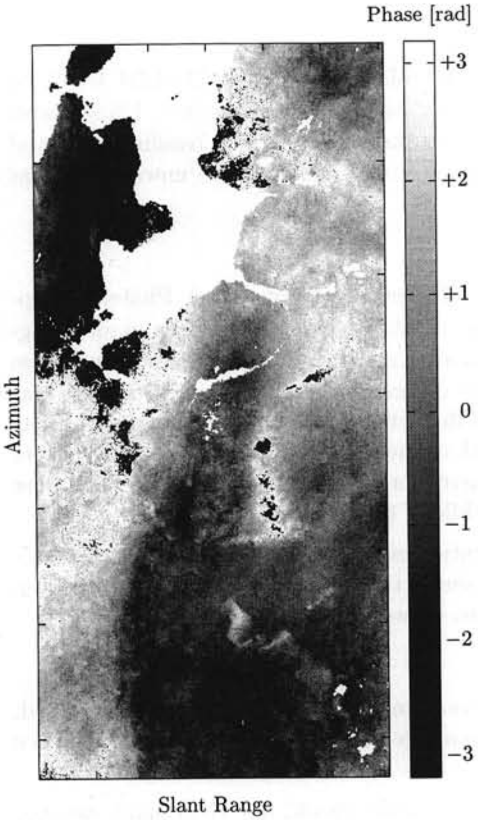

Figure 5.141 *Interferogram fa4*

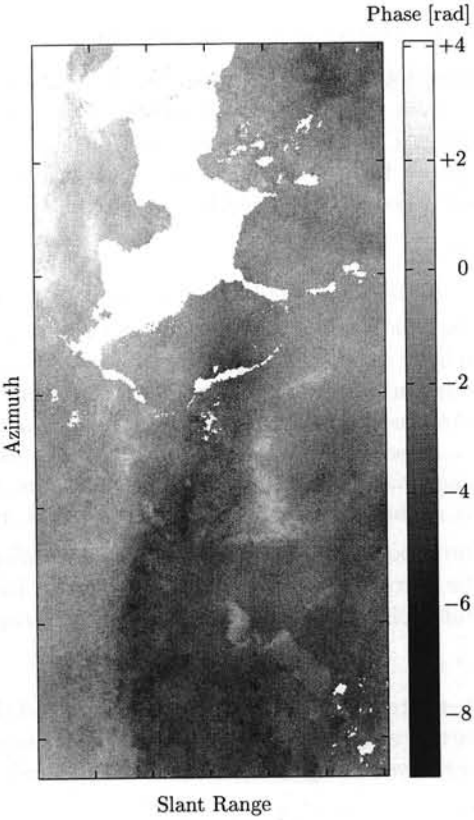

Figure 5.142 *Unwrapped interferogram fa4*

the precipitation evaporates before it reaches the surface. The layer between 3000 meter height and just above surface is dry according to the radiosondes. Above this dry layer there is a layer of about 2 km thickness which is very wet. The precipitation is falling from this layer through the dry layer beneath. This causes the relative humidities at the stations "under" the precipitation to be very high: between 85 and 100%.

Reported cloud cover at day 2, 21:00 UTC, included an almost complete (8/8) cloud cover over the whole area, mainly stratocumulus.

5.5.4.3 Conclusions

The strong correlation between the distribution of precipitation (possibly evaporating rain) and phase delay in the interferogram identifies the origin of the atmospheric artifacts. Note that also the loss of coherence over Friesland corresponds clearly with the areas of precipitation. Although outside the scope of this study, it can therefore be concluded that atmospheric artifacts can also increase increase the noise level of interferograms.

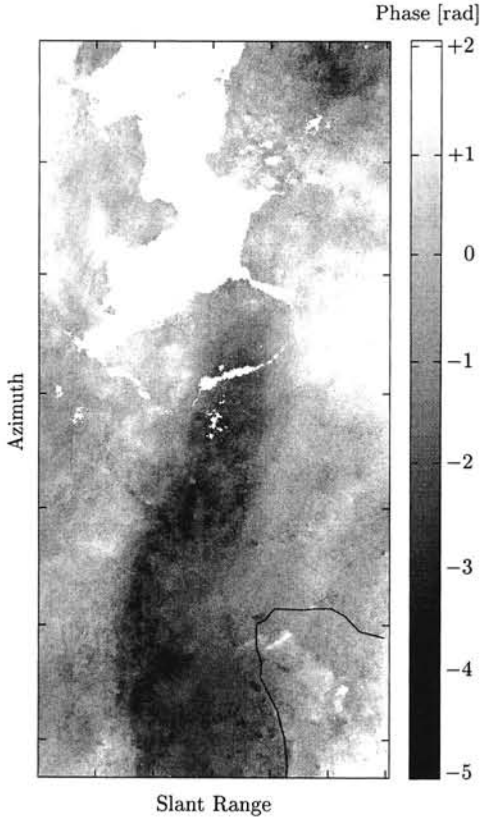

Figure 5.143 *Unwrapped differential interferogram fa4*

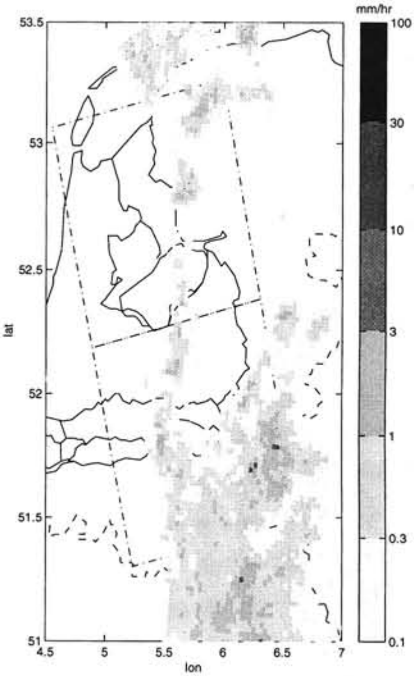

Figure 5.144 *Weather radar for interferogram fa4, day 2, 21:45 UTC*

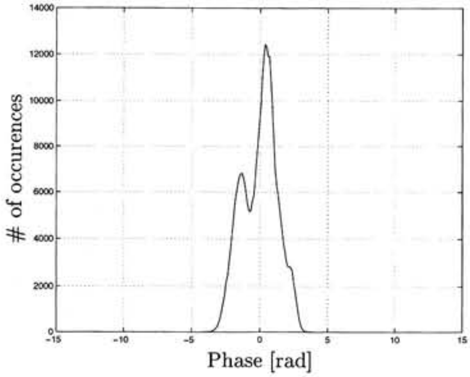

Figure 5.145 *Histogram of a major part of interferogram fa4*

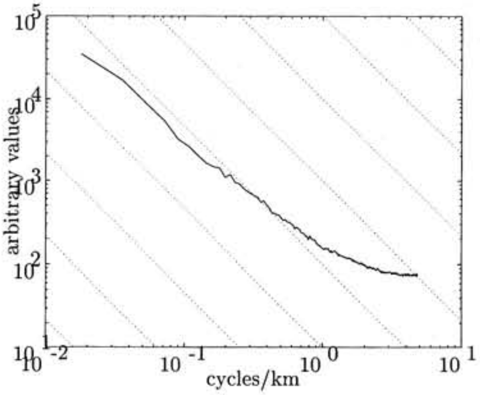

Figure 5.146 *Rotationally averaged spectrum of interferogram fa4*

Station	#	UTC	Day	Level 1	Level 2	Level 3
De Kooij	235	2100	1	3/8, Sc, 3000	6/8, Ac, 3000	
Schiphol	240	2100	1	4/8, Ac, 3000	6/8, Ci, 8300	
De Bilt	260	2100	1	6/8, Ac, 3000	8/8, Ac, 3300	
Soesterberg	265	2100	1	7/8, Ac, 3000		
Leeuwarden	270	2100	1	2/8, Sc, 3000	7/8, Ac, 3000	
Deelen	275	2100	1			
Gilze-Rijen	350	2100	1	7/8, Ac, 3000		
Eindhoven	370	2100	1	7/8, Sc, 3000		
Volkel	375	2100	1	7/8, Ac, 3000		
De Kooij	235	2200	1	2/8, Sc, 3000	3/8, Ac, 3000	6/8, Ac, 3300
Schiphol	240	2200	1	2/8, Ac, 3000	3/8, Ci, 8300	
De Bilt	260	2200	1	3/8, Ac, 3000		
Soesterberg	265	2200	1	6/8, Ac, 3000		
Leeuwarden	270	2200	1	4/8, Sc, 3000	6/8, Sc, 3000	8/8, Ac, 3000
Deelen	275	2200	1			
Gilze-Rijen	350	2200	1	6/8, Ac, 3000		
Eindhoven	370	2200	1	7/8, Sc, 3000		
Volkel	375	2200	1	4/8, Ac, 3000	7/8, Ac, 3000	
De Kooij	235	2100	2	1/8, Ac, 3000	7/8, As, 3300	8/8, Ci, 8300
Schiphol	240	2100	2	1/8, Ac, 3000	6/8, Ci, 8300	
De Bilt	260	2100	2	3/8, Ac, 3000	7/8, Ci, 8300	
Soesterberg	265	2100	2	1/8, Ac, 3000	7/8, Ac, 3300	
Leeuwarden	270	2100	2	8/8, Sc, 3000		
Deelen	275	2100	2			
Gilze-Rijen	350	2100	2	3/8, Ac, 3000	6/8, Ci, 8300	
Eindhoven	370	2100	2	4/8, Ac, 3300	7/8, Ci, 8300	
Volkel	375	2100	2	2/8, Sc, 1600	8/8, Sc, 3000	
De Kooij	235	2200	2	2/8, Ac, 3000	4/8, As, 3300	8/8, Ci, 8300
Schiphol	240	2200	2	1/8, Ac, 3000	6/8, Ac, 3300	7/8, Ci, 8300
De Bilt	260	2200	2	2/8, Sc, 3000	5/8, Ac, 3000	7/8, Ci, 8300
Soesterberg	265	2200	2	1/8, Ac, 3000	3/8, Ac, 3300	7/8, Ci, 6600
Leeuwarden	270	2200	2	8/8, Sc, 1600		
Deelen	275	2200	2			
Gilze-Rijen	350	2200	2	1/8, Sc, 1600	6/8, Ac, 3000	
Eindhoven	370	2200	2	4/8, Sc, 1600	7/8, Ac, 3300	
Volkel	375	2200	2	2/8, Cb, 1300	6/8, Sc, 1600	

Table 5.20 *Cloud observations fa4: 30-04/01-05-1996. The observations give the amount of cloud cover (okta), the type of cloud, and the cloud base at 3 levels. Height is given in meters.*

5.5.5 Analysis of interferogram fa5

Interferogram fa5 was acquired at June 4 and 5, 1996, at 21:41:00 UTC (23:41:00 LT). SAR frame numbers 1053 and 1035 are used, for ERS-1 orbit 25568, and ERS-2 orbit 5895. The parallel baseline is −34 and −35 m, the perpendicular baseline −88 and −89 m, for the southern and the northern image respectively. The phase unwrapping is performed using the algorithm of Ghiglia and Romero (1994).

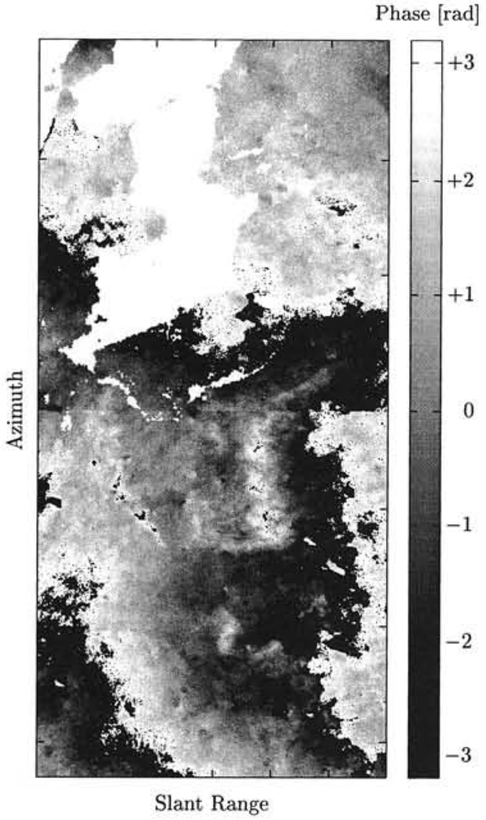

Figure 5.147 *Interferogram fa5*

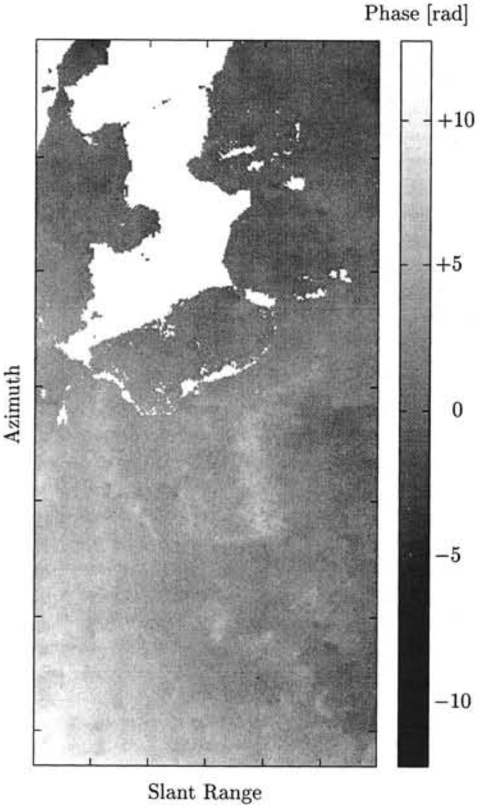

Figure 5.148 *Unwrapped interferogram fa5*

5.5.5.1 Observations

In figure 5.147 and 5.148, the relative phase and the absolute phase of interferogram fa5 are shown respectively. There is still a strong phase ramp of 2 fringes over the interferogram. Remaining phase unwrapping residues cause localized errors over especially the lower image. The differential interferogram is shown in figure 5.149. Both the topographic phase, and the linear phase ramp in azimuth and range direction are corrected for. Phase fluctuations in the differential interferogram vary between −4 and 3 rad over the whole image. Anomalies are observed over the island Texel in the upper left part of the image, just right of Flevoland, and in the lower left part of the image. Small waves can be found in parts of the upper right quadrant of the image, see figure 5.150. The wavelength is typically 1 km, with an amplitude of 0.8 rad. The waves are aligned with an angle of

−22 degrees with respect to the azimuth direction, which is 232 degrees with respect to the north. The histogram of the differential interferogram is shown in figure 5.151. The overall rms value is 1.2 rad. Figure 5.152 shows the rotationally averaged spectrum. The overall curve does not follow the −5/3 gradient.

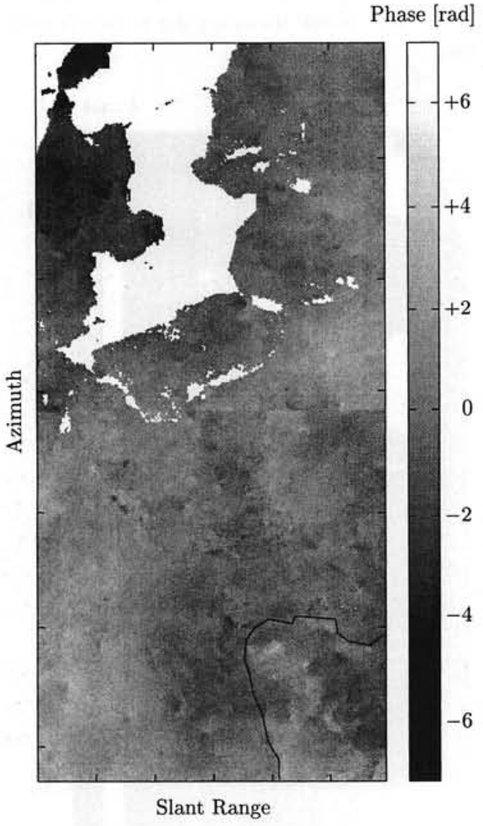

Figure 5.149 *Unwrapped differential interferogram fa5*

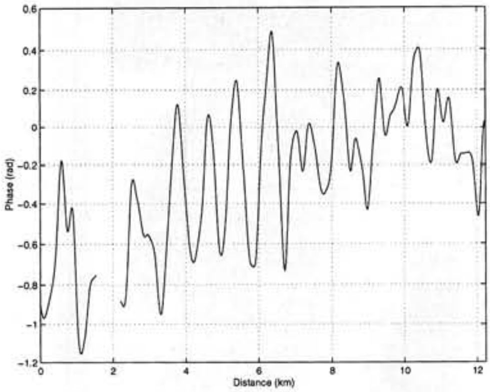

Figure 5.150 *A cross section in the upper right part of the image*

5.5.5.2 Interpretation

The observations include wave effects over Friesland nearly perpendicular to the wind direction, anomalous areas over Noord-Holland, humps and spots in both images, and wave effects (rolls) parallel to the wind direction over the Noord-oostpolder and Overijssel.

The days during which the SAR images were acquired were characterized by the passage of a cold front in a high pressure zone. The cold front, however, did not have strong effects: there was no precipitation and there were very few clouds. Cloud cover varied from 1–4 octa cirrus.

The weather radar did not indicate anything at both days (the second days there was some scatter noise). From the Meteosat infrared channel not much cloud cover is found. From the radiosondes we find and inversion at 1200 m at day 1 and at 1000 m at day 2. This could explain the wave effects.

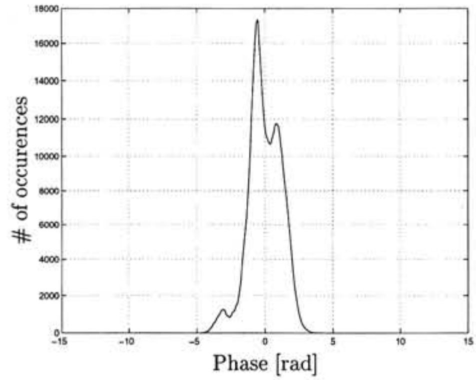

Figure 5.151 *Histogram of a major part of interferogram fa5*

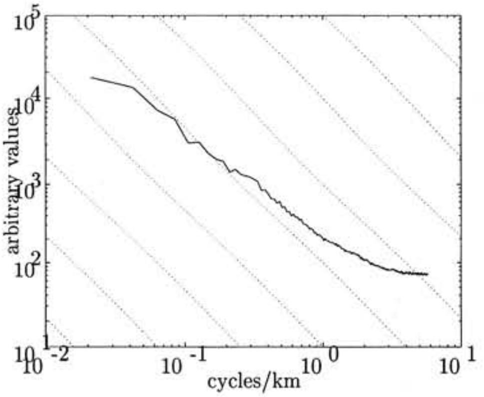

Figure 5.152 *Rotationally averaged spectrum of interferogram fa5*

In the northern image area, gravity waves are observed over Friesland, especially at the first day. In the southern image gravity waves can be found west of the Veluwe, especially the second day. The waves are perpendicular to the wind direction.

At day 1, 21:00 UTC there was shallow fog (radiation fog) at De Kooy. Therefore there is at that time only very few cloud cover. Note that the wind direction in De Kooy is 330 degrees, and in Schiphol 50 degrees. This indicates that the axis of the high pressure zone is in between! There is, however, not much wind. At 22:00 UTC it is almost calm and nearly cloudless. Leeuwarden indicates haze, with a visibility of 8 km. Almost all stations report 1/8–2/8 cirrus. De Kooy has some altocumulus.

At day 2, all stations report 1/8–4/8 cirrus, therefore there is also almost no real cloud cover. Both De Kooy and Leeuwarden indicate haze, with a visibility of 7 km. There is almost no wind, from eastern direction (90–110 degrees). Meteosat infrared observations indicate almost no clouds at both days.

5.5.5.3 Conclusions

The features in interferogram may find there origin in the presents of an subsidence inversion, below which some moisture can be trapped. The observed waves with a wavelength of around 1 km are presumably gravity waves at the inversion altitude.

Station	#	UTC	Day	Level 1
De Kooij	235	2100	1	1/8, Ac, 3300 m
Schiphol	240	2100	1	3/8, Ci, 8300 m
De Bilt	260	2100	1	1/8, Ci, 8300 m
Soesterberg	265	2100	1	1/8, Cc, 8300 m
Leeuwarden	270	2100	1	1/8, Ci, 8300 m
Deelen	275	2100	1	
Gilze-Rijen	350	2100	1	2/8, Ci, 8300 m
Eindhoven	370	2100	1	1/8, Ci, 8300 m
Volkel	375	2100	1	1/8, Ci, 8300 m
De Kooij	235	2200	1	1/8, Ac, 3300 m
Schiphol	240	2200	1	1/8, Ci, 8300 m
De Bilt	260	2200	1	
Soesterberg	265	2200	1	1/8, Ci, 8300 m
Leeuwarden	270	2200	1	1/8, Ci, 8300 m
Deelen	275	2200	1	
Gilze-Rijen	350	2200	1	1/8, Ci, 8300 m
Eindhoven	370	2200	1	1/8, Ci, 8300 m
Volkel	375	2200	1	
De Kooij	235	2100	2	4/8, Ci, 8300 m
Schiphol	240	2100	2	1/8, Ci, 8300 m
De Bilt	260	2100	2	3/8, Ci, 8300 m
Soesterberg	265	2100	2	3/8, Ci, 8300 m
Leeuwarden	270	2100	2	5/8, Ci, 8300 m
Deelen	275	2100	2	
Gilze-Rijen	350	2100	2	3/8, Ci, 8300 m
Eindhoven	370	2100	2	1/8, Ci, 8300 m
Volkel	375	2100	2	1/8, Ci, 10000 m
De Kooij	235	2200	2	3/8, Ci, 8300 m
Schiphol	240	2200	2	1/8, Ci, 8300 m
De Bilt	260	2200	2	2/8, Ci, 8300 m
Soesterberg	265	2200	2	3/8, Ci, 8300 m
Leeuwarden	270	2200	2	4/8, Ci, 8300 m
Deelen	275	2200	2	
Gilze-Rijen	350	2200	2	2/8, Ci, 8300 m
Eindhoven	370	2200	2	1/8, Ci, 8300 m
Volkel	375	2200	2	1/8, Ci, 10000 m

Table 5.21 *Cloud observations fa5: 04-06/05-06-1996. The observations give the amount of cloud cover (okta), the type of cloud, and the cloud base at 1 level.*

5.6 Discussion

Although the number of 52 SAR images, corresponding with 26 analyzed interferograms, is certainly not enough to provide sufficient information for a thorough statistical analysis, it may be useful to summarize the observed effects in a more systematic way. The database of SAR images covers nearly every month of the year, see the histogram in figure 5.153, except January. Therefore, all seasons have been sampled. Unfortunately, the limited duration of the ERS tandem mission does not permit a longer series of interferograms over one particular area. A consequence of the orbit configuration is that the diurnal cycle of the weather is only sampled at one nearly discrete time instant for every image. Therefore, the imaging times are always approximately 21:40 UTC for the *Flevoland ascending* interferograms, and about 10:30 UTC for all other interferograms. Variations between daytime and nighttime acquisitions could therefore not be studied.

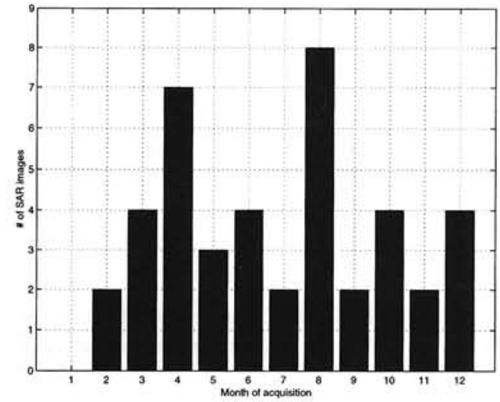

Figure 5.153 *Histogram showing the number of analyzed SAR images, ordered by the month of acquisition.*

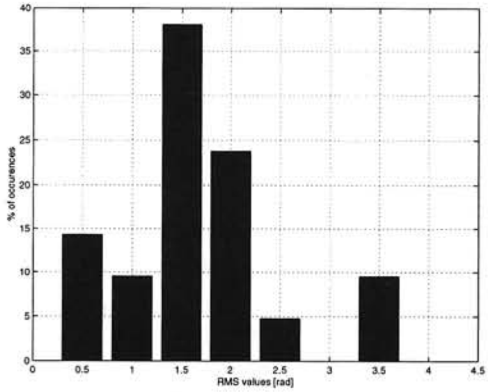

Figure 5.154 *Histogram showing the rms values of the interferograms in the database and the frequencies of occurrence*

A review of the observed rms phase values is shown in table 5.22. The rms values vary between 0.6 rad for interferogram gd4, and 3.6 rad for interferogram fa2. Note that the interpretation of the rms values is dependent on the area used for its calculation. For each of the 5 interferogram locations studied, the decorrelated areas (mainly water) varied in spatial coverage, and the combination of two interferograms in the *Flevoland ascending* series enabled a much larger surface for evaluation.

Figure 5.154 shows the percentages of occurrence for the rms values, in eight categories. Root mean square values around 1.5 rad occur the most frequently in this series. Ordering the observed rms values based on the month of acquisition produces the histogram in figure 5.155. The months May and July have in this database phase variations with an rms which is double of the values observed in all other interferograms. Naturally, this is a consequence of only one or two interferograms, and it can therefore not be used for the derivation of general rules. However, it can be expected that 'summer'-thunderstorms, which occur often in this region, will produce strong phase artifacts in corresponding interferograms.

ID	rms (rad)	class	cloud	waves	striation	localized anomalies	keyword
gd1	3.4	D	Cb		yes	yes	cells
gd2	1.5	B			yes	yes	pearls
gd3	1.6	C					dog ear
gd4	0.6	A		yes	yes		x-waves
gd5	1.4	B		yes	yes	yes	
gd6	1.8	C	Cu		yes	yes	cells
gd7	1.8	C	Cu		yes	yes	cells
gdex2	1.9	C		yes		yes	corner
cd1	1.0	B	Cb		yes	yes	cells
fd1	1.7	C	Cu		yes	yes	bean,cells
fd2	1.3	B	Cu	yes		yes	cells
fd3	1.3	B				yes	gradient
fd4	1.8	C	Cb			yes	cells
fd5	0.7	A				yes	
fd6	0.5	A		yes	yes		
fd7	1.7	B	Cu	yes	yes	yes	cells
fa1	2.0	C	Cu			yes	cells,intrusion
fa2	3.6	D	Cb			yes	sickle,line,cells
fa3	2.5	C		yes		yes	ramp
fa4	1.3	B				yes	intrusion
fa5	1.2	B		yes		yes	cells

Table 5.22 *Statistics and observations in the interferograms. The rms values are listed, as well as the magnitude class, see table 5.23. Only cumulus or cumulonimbus clouds are indicated in the cloud category. Waves are observed mostly at small parts of the image. Striation indicates clear anisotropic behavior of the observed patterns. Localized anomalies are defined as artifacts with a spatial extent of 20 km or less, and a phase disturbance of 2 rad or more. The keyword column describes special features of the interferogram.*

5.6.1 Classification of the observed effects

A classification of the observed effects can be based on the magnitude and the type and scale of the disturbance. Based on the *magnitude*, four classes are defined based on the observed rms values. The rms values are regarded to be representative for a Gaussian distribution, and can be used to find the 95% range of the distribution. The classes, labeled A, B, C, and D, are listed in table 5.23, together with the percentage of the analyzed interferograms which fall in this range. Table 5.22 indicates for each interferogram to what category it belongs.

Based on the *type* of disturbance, *localized anomalies* are defined as those disturbances which occur on a spatial scale of less than 20 km, and have a magnitude of more than 2 radians. Within this definition, 17 of the 21 (combined) interferograms displayed this type of artifacts. These interferograms are listed in table 5.22. Furthermore, in the table it is shown if wave effects are observed. Waves have been observed perpendicular as well as parallel to the wind direction at some heights. These effects are mostly localized, and

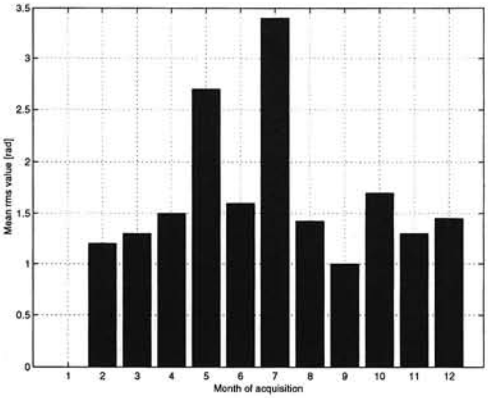

Figure 5.155 *Histogram showing the mean rms values, ordered by the month of acquisition*

Class	rms (rad)	95% range (rad)	Percentage
A	$< \pi/4$	$[0, \pi]$	14%
B	$[\pi/4, \pi/2]$	$[\pi, 2\pi]$	38%
C	$[\pi/2, \pi]$	$[2\pi, 4\pi]$	38%
D	$\pi <$	$[4\pi, \infty]$	10%

Table 5.23 *Classification of the magnitude of atmospheric disturbance.*

relatively small. Wave effects are observed in 8 of the 21 interferograms. Another effect is *striation*—where almost the whole interferogram is covered by a pattern with a clear orientation. Sometimes these effects could be defined as moisture transport in a more or less laminar flow. The possibility to find an orientation in the effects occurred in 10 of the 21 interferograms. Finally, one or two *keywords* have been chosen, which reflect the peculiarities of a specific interferogram. *Cells* occur most often, and indicate localized phase artifacts, which are quite discernible from the background. *Pearls* is a keyword for the 'string of pearls' effect, where a pattern is formed by many small circular anomalies, often aligned in a certain direction. The *dog ear* is specific for gd3, and shows a peculiar anomaly in the corner of the interferogram. The effect labeled *x-waves* shows wave-like effects in more than on direction. All other keywords refer to the shape of the observed anomalies.

An interesting relation is found by listing all the observations of cumulus or cumulonimbus clouds in table 5.22. It appears that in all cases in which these cloud types were observed, *cells* were observed in the interferogram. From this observation, it may be concluded that this type of cloud cover indicates strong local variations in relative humidity, which has a considerable influence on the SAR interferograms.

Chapter 6

Conclusions and recommendations

6.1 Conclusions

In this study, a series of 26 SAR interferograms is analyzed in order to assess the influence of atmospheric heterogeneities on the interferometric phase observations from the ERS tandem mission. This report gives a brief summary of the current understanding of signal delay induced by the Earth's atmosphere, and its effect on repeat pass SAR interferometry. It describes the characteristics of the used interferometric and meteorologic database, and systematically covers the analyses of all interferograms. Based on this work, the following conclusions can be drawn.

6.1.1 The scale and magnitude of the observed effects

Atmospheric influences have been observed in each of the 26 interferograms. The observed spatial scales reach from hundreds of meters to 100–200 km. For scales reaching the full image size, it is, however, difficult to discern them from errors in the satellite orbits.

The magnitude of the effects can be expressed in an rms value, or in the extreme values observed in the interferogram. Observed rms values, taken over a significant part of the image, reach from 0.5–3.6 radians. Assuming a Gaussian distribution, this implies that 95% of the observed phase values varies over a minimal range of 0.3 phase cycles up to a maximal range of 2.3 phase cycles. Extreme ranges of 4 phase cycles are found during thunderstorms at the two SAR acquisitions.

Note that the degree of coherence was found to be sufficient (> 0.7) for all land areas in the interferograms.

6.1.2 A classification of effects

Analyzing the series of interferograms, it became apparent that every interferogram displayed a totally different atmospheric behavior. Nevertheless, it is tried to sort the observed atmospheric disturbance in different categories. First, *isolated anomalies* are found in 18 of the 21 (combined) interferograms. Isolated anomalies are defined here as anomalies with a spatial extent of 20 km or less, and a phase disturbance of 2 radians or more. Secondly, *striation* is observed in 10 interferograms. Striation refers to a pattern of linear features over a significant portion of the interferogram, often connected with transport of moisture. The effect may be equal over the whole interferogram, or change gradually from a more laminar to a turbulent flow. A third category is formed by *wave effects*. The waves are mostly observed in only a part of the interferogram, and can be often identified as gravity waves or cloud/moisture streets. The amplitude is mostly less than 1 phase cycle. *Frontal zones* form a fourth category. Different effects have been observed, from smooth gradients in the phase, to a very distinct 'wave crest' with a wavelength of just some 5 kilometers. Finally, *overall atmospheric variation* is observed in many of the interferograms. This is phase variation of a limited magnitude, and with varying wavelengths, perhaps best described as a 'bumpy' surface. This effect might be closely connected with turbulent behavior of air and its constituents.

6.1.3 The driving mechanisms

Atmospheric signal in SAR interferograms is due to localized changes in the refractive index of the medium. Changes in the refractive index can be caused by more parameters than only pressure, temperature and water vapor. Using the weather radar, it seems that also rain fall can influence the refractive index, resulting in severe phase shifts in the interferogram. In most of the cases the spatial variation of pressure and temperature is not large enough to cause strong localized phase gradients in the 100 × 100 km interferograms. Their effects will cause gradients over the whole interferogram, which are difficult to discern from, e.g., orbit uncertainties. The localized spatial behavior of humidity is believed to be dominant in causing atmospheric signal in the interferograms.

No identifiable ionospheric effects have been found in this series of interferograms. For all interferograms, reasonable explanations for the observed effects could be provided using only variation in tropospheric parameters.

6.1.4 The use of meteorological information

In general, two types of meteorological data can be distinguished in this context. First, near-instantaneous observations (weather radar, cloud observations, weather observations, coinciding high resolution satellite imagery) at the time of the SAR acquisitions can give an indication for the type, size and magnitude of the disturbances to be expected. Secondly, more general meteorological information, such as daily weather charts, weather model data, and some satellite imagery can be used to express the likelihood of some types of atmospheric disturbance in SAR interferograms.[1]

Weather radar observations of precipitation correlate in most cases closely with observed anomalies in the interferograms. This fact, and the nearly continuous operation of the weather radar over this area yield possibilities for at least an identification tool for strong localized artifacts. Further study is needed to assess the relationship between the observations of both instruments, which might lead to algorithms to suppress the interferometric artifacts using weather radar information.

Meteorological information from current *satellite imagery* can be useful for the detection of storm fronts, or regions of strong atmospheric instability. However, the temporal and spatial sampling rates pose the main limitations for this type of observations. Much of the strong disturbance in interferograms can be observed within small spatial ranges, e.g., less than 10 km. The resolution of Meteosat and AVHRR is too coarse to observe this, although AVHRR gives already some better quality when combining the different

---

[1] A short overview on the use of meteorological information is given in Hanssen et al. (1998b)

channels. Temporal sampling is the second limitation. Whereas a geostationary satellite such as Meteosat provides an image every half hour, AVHRR resamples every six hours. This implies that the time difference between the SAR acquisition and the nearest AVHRR acquisition varies between 1 and 3 hours, which is often too long to interpret the state of the atmosphere. If, however, spaceborne meteo-observations are available, the most important features to look for are strong convective clouds (cumulonimbus), strong and short water vapor gradients, and wave patterns.

Synoptic observations can be used to get an overview of the meteorological situation during a SAR acquisition. An advantage of this type of observations is that they are regularly acquired (every hour) over a large number of observation stations, and that the observations are coded in an internationally consistent way. Apart from the automatic observations, especially the manual observations can be of great significance. Manual observations include cloud type, cloud cover, cloud heights, and weather category. It has been shown that often the most disturbing *localized anomalies* in the interferometric phase can be connected to convective cloud development, i.e. clouds of the *cumulus* and *cumulonimbus* genus.

Daily national or regional *weather charts* give a first impression of the dynamics of the weather during the day in which a SAR image was acquired. Naturally, this is only of very limited use to assess the amount of disturbance in an interferogram. It may, however, be useful if one needs to select from a series of acquisitions over a specific area. Especially precipitation or cloud cover measures can be routinely used to either select or reject a specific image from a series.

Apart from the information obtained from additional meteorological data sources, information on the atmospheric status can sometimes be obtained from the *backscatter* over water areas, see Hanssen et al. (1998a). Especially information on the wind direction and velocity, footprints of rain cells, or boundary layer vortices can be available from single SAR images, and be used as a priori information on the expected atmospheric signal in the interferogram.

Table 6.1 shows a generalized overview of the characteristics and estimated availability of different meteorological observations.

Method	Spatial res.	Temp. res.	Type of effect	Availability
Synoptic	[30 × 30]	[0.5–1]	clouds fronts	medium
Weather radar	[0.5 × 0.5]	[0.25]	precip	hard
Radio sondes	[100 × 100]	[6–12]	waves	medium
Spaceborne:				
geostat:	[5 × 5]	[0.5]	fronts convection	good
orbiting:	[1 × 1]	[6]	clouds	good
Weather charts	[50 × 50]	[24]	fronts	good

Table 6.1 *The use of historical meteorological data: average spatial and temporal resolution, type of effect, and estimate of availability.*

6.1.5 Some rules of thumb

Although the amount of investigated situations is certainly not sufficient to give statistical estimates, some general rules of thumb can be given based on the experience obtained here and the knowledge of general atmospheric dynamics.

- Winter acquisitions are expected to be more stable in terms of atmospheric disturbance than summer and especially autumn acquisitions. This is due to the fact that cold air cannot hold that much water vapor, and that convection is usually less extreme.
- The convective layer is usually more active during daytime. During nighttime there is a residual layer and a stable boundary layer. Therefore, it can be expected that nighttime SAR acquisitions show less atmospheric disturbance due to convection than daytime acquisitions. For the ERS orbits, this implies that ascending orbits are prefered over descending orbits.

On the handling of atmospheric signal

Generally, there are two ways for treating atmospheric disturbance in SAR interferograms: *selection* or *statistical suppression*. This study has been focussed on selection, assuming that either only two SAR images are available[2] and it is necessary to get estimates of the amount and characteristics of the atmospheric artifacts, or that the tandem interferogram is not processed yet, and an a priori statement on the amount of disturbance to be expected is desired.

Convective processes are most likely to be detected in interferograms, especially when more than one interferometric pair is evaluated. Therefore, a procedure of averaging interferograms (*statistical suppression*) is cumbersome for these effects, since many interferograms are necessary for eliminating these strong and isolated effects. For the interferometric characteristics of *overall atmospheric variation*, stacking and averaging interferograms is more likely to have good results, since the spectral characteristics are comparable in more interferograms. The same holds for the wave effects.

6.1.6 Meteorological relevance

Interferometric signal delay maps can be useful for further study and for the understanding of atmospheric water vapor distribution and the relative amounts of precipitable water in clouds. Especially the combination of the high resolutions, starting from 20×20 m, the nearly instantaneous data acquisitions, and the accuracies, can help provide new insights in atmospheric dynamics. The large database of tandem SAR images acquired over the world contains a wealth of information for scientific research in this field.

6.2 Recommendations

6.2.1 On the assimilation of meteorological observation with SAR interferometry

The relationship between coded manual synoptic observations and the interferometric phase anomalies suggests a potential for an automatic evaluation system. Possibilities to

---

[2] This is often the case for ERS tandem interferograms, since temporal decorrelation over longer times hampers an evaluation of a series of interferograms

obtain these synoptic observations for a specific region in the world using the Internet need to be studied. Global or regional meteorologic organizations could be of assistance in this respect.

6.2.2 The elimination of the effects

Temporally coincident quantitative observations by weather radar could be further analyzed and compared with observed phase delays in the interferograms. Establishing a functional relation between both types of observations is a first step towards elimination of localized anomalies in the SAR interferograms.

6.2.3 The quantification of the effects

Since rms values can be determined using areas of different spatial extent, the effect of localized but strong anomalies will differ depending on the area used for evaluation. Especially since errors in distinguishing topographic from atmospheric signal will be significant for localized strong anomalies in combination with relatively short baselines, more specialized error measures need to be used to describe the observed atmospheric disturbance signal.

6.2.4 The use of meteorological data

Since atmospheric phenomena as rain, cold fronts and water vapor distribution have been found the main sources of interferometric disturbance, climatological/meteorological statistical information on a specific area can be valuable to assess the possibilities and type of atmospheric disturbance to be expected. Information on cloud types and frequencies of occurrence are often available as a function of the time of year, which can give some a priori information on a specific area. The same holds for rain statistics and general atmospheric activity.

6.2.5 The ERS SAR tandem archive

As described in paragraph 6.1.6, the archive of potential ERS tandem interferograms, in combination with reference elevation models, contains a wealth of information for the atmospheric sciences. An active promotion of this new application of SAR interferometry is needed to inform the scientific community of these possibilities.

6.2.6 Münchhausens bootstrap

Baron von Münchhausen pulled himself and his horse out of a swamp by pulling his own bootstrap. The story shows the inherent connection—and paradox—of one action (to pull) with another (to be pulled). An equivalent reasoning holds in my opinion for the different effects in repeat pass SAR interferograms, there is an inherent connection between the different types of signals which are merged in the interferometric phase. In recent studies on atmospheric effects in SAR interferometry, mostly terms as atmospheric *disturbance* or *artifacts* were used. Based on the experience from this work, I propose to regard the influence of the atmosphere on SAR interferometry as a mature signal, and to refer to it in future publications as atmospheric *signal*.

Bibliography

Afraimovich, E. L., Terekhov, A. I., Udodov, M. Y. and Fridman, S. V. (1992), Refraction distortions of transionospheric radio signals caused by changes in a regular ionosphere and by travelling ionospheric disturbances, *Journal of Atmospheric and Terrestrial Physics*, **54**(7/8):1013–1020.

Alber, C., Ware, R., Rocken, C. and Solheim, F. (1997), GPS surveying with 1 mm presision using corrections for atmospheric slant path delay, *GRL*, **24**(15):1859–1862.

Askne, J. and Nordius, H. (1987), Estimation of tropospheric delay for microwaves from surface weather data, *Radio Science*, **22**:379–386.

Bean, B. R. and Dutton, E. J. (1986), *Radio Meteorology*, Dover, New York.

Bevis, M., Businger, S., Herring, T. A., Anthes, R. A., Rocken, C. and Ware, R. H. (1994), GPS meteorology: mapping zenith wet delays onto precipitable water, *Journal of Applied Meteorology*, **33**(3).

Bevis, M., Businger, S., Herring, T. A., Rocken, C., Anthes, R. A. and Ware, R. H. (1992), GPS Meteorology: Remote sensing of atmospheric water vapor using the Global Positioning System, *Journal of Geophysical Research*, **97**:15,787–15,801.

Bevis, M., Chiswell, S., Businger, S., Herring, T. A. and Bock, Y. (1996), Estimating wet delays using numerical weather analysis and predictions, *Radio Science*, **31**(3):477–487.

Born, M. and Wolf, E. (1980), *Electromagnetic Theory of Propagation Interference and Diffraction of Light*, Permagon Press, New York.

Campen, C. F., Cole, A. E., Condron, T. P., Ripley, W. S., Sissenwine, N. and Solomon, I., eds. (1960), *Handbook of Geophysics*, MacMillan, New York.

Cheng, K. and Huang, Y.-N. (1992), Ionospheric disturbances observed during the period of Mount Pinatubo eruptions in June 1991, *Journal of Geophysical Research*, **97**(A11):16,995–17,004.

Costantini, M. (1996), A Phase Unwrapping Method Based on Network Programming, in: *Fringe 96, Zürich, Switzerland.*

Crane, R. K. (1996), *Electromagnetic wave propagation through rain*, John Wiley & Sons, Inc., New York.

Darling, A. and Mongeon, A. (1996), Meteorological Codes, National Weather Service, http://www.nws.noaa.gov/code.shtml.

Davis, J., Elgered, G., Niell, A. and Kuehn, C. (1991), Ground-based measurement of gradients in the "wet" radio refractivity of air, *Radio Science*, **28**:1003–1018.

Davis, J. L., Herring, T. A., Shapiro, I. I., Rogers, A. E. E. and Elgered, G. (1985), Geodesy by radio interferometry: Effects of atmospheric modelling errors on estimates of baseline length, *Radio Science*, **20**(6):1593–1607.

Delacourt, C., Briole, P., Achache, J., Fruneau, B. and Carnec, C. (1997), Correction of the tropospheric delay in SAR interferometry and application to 1991-93 eruption of Etna volcano, Italy, in: *AGU Fall meeting, December 8-12, San Francisco, USA,*.

Duchossois, G., Kohlhammer, G. and Martin, P. (1996), Completion of the ERS Tandem Mission, *Earth Observation Quarterly*, **55**.

Dupont, S., Nonin, P., Renouard, L., Pichon, G. and Bignone, F. (1997), Atmospheric artifacts in ERS DTM. ISTAR's experience over multiple sites and large areas, in: *Proc. of the third ERS symposium, Florence, Italy, 17-20 March 1997*.

ECMWF (1994), ECMWF, *Meteorological Bulletin*, **M3.2**.

Edgar, A. K., Dodsworth, E. J. and Warden, M. P. (1973), The design of a modern surveillance radar, in: *Int. Conf. Radar–Present and Future, IEE Conf.Pub.,no. 105, 23–25 Oct. 1973*, pp. 8–13.

Eineder, M. and Adam, N. (1997), A Flexible System for the Generation of Interferometric SAR Products, in: *International Geoscience and Remote Sensing Symposium, Singapore,3–8 August 1997*.

Elliot, W. P. and Gaffen, D. J. (1991), On the utility of radiosonde humidity archives for climate studies, *Bulletin of the American Meteorological Society*, **72**:1507–1520.

Frisch, U. (1995), *Turbulence: the legacy of A.N. Kolmogorov*, University Press, Cambridge.

Ghiglia, D. C. and Romero, L. A. (1994), Robust two-dimensional weighted and unweighted phase unwrapping that uses fast transforms and iterative methods, *J. Opt.Soc.Am.A*, **11**(1):107–117.

Goldhirsch, J. and Rowland, J. R. (1982), A Tutorial Assessment of Atmospheric Height Uncertainties for High-Precision Satellite Altimeter Missions to Monitor Ocean Currents, *IEEE Trans. on Geoscience and Remote Sensing*, **GE-20**(4):418–434.

Goldstein, R. (1995), Atmospheric limitations to repeat-track radar interferometry, *Geophysical Research Letters*, **22**(18):2517–2520.

Hall, M. P. M., Barclay, L. W. and Hewitt, M. T., eds. (1996), *Propagation of Radiowaves*, The Institution of Electrical Engineers, London.

Hanssen, R. (1996), GISARE: GPS metingen voor de schatting van atmosferische parameters, *GPS Nieuwsbrief*, **11**(1):17–21.

Hanssen, R. and Feijt, A. (1996), A first quantitative evaluation of atmospheric effects on SAR interferometry, in: *'Fringe 96' workshop on ERS SAR Interferometry, 30 Sep – 2 Oct, Zürich, Switzerland*, pp. 277–282, ESA SP-406.

Hanssen, R., Lehner, S. and Weinreich, I. (1998a), Atmospheric Heterogeneities from - ERS tandem SAR Interferometry and Sea Surface Images, in: *CEOS SAR Workshop, ESTEC, Noordwijk, The Netherlands, 3-6 February 1998*, pp. 33–39.

Hanssen, R. and Usai, S. (1997), Interferometric phase analysis for monitoring slow deformation processes, in: *3rd ERS Symp. on Space at the service of our Environment, Florence, Italy, 17–21 March 1997*, ESA SP-414, pp. 487–491.

Hanssen, R., Zebker, H., Klees, R. and Barlag, S. (1998b), On the use of meteorological observations in SAR interferometry, in: *International Geoscience and Remote Sensing Symposium, Seattle,6–10 July 1998*, pp. 1644–1646.

Ho, C. M., Mannucci, A. J., Lindqwister, U. J., Pi, X., Tsurutani, B. T., Sparks, L., Iijima, B. A., Wilson, B. D., Harris, I. and Reyes, M. J. (1998), Global ionospheric TEC variations during January 10, 1997 storm, *GRL*, **25**(14):2589–2592.

Hopkins, E. J. (1996), Weather and Climate: RADIOSONDES - An Upper Air Probe, http://www.meteor.wisc.edu/~hopkins/aos100/wxi-raob.htm, University of Wisconsin.

Jakowski, N., Bettac, H. D. and Jungstand, A. (1992), Ionospheric corrections for Radar Altimetry and Geodetic Positioning Techniques, in: *Proc. of the Symp. Refraction of Transatmospheric Signals in Geodesy, the Hague, 19–22 may 1992*, pp. 151–154.

Kooij, M., van Halsema, D., Groenewoud, W., Mets, G. J., Overgaauw, B. and Visser, P. (1995), *SAR Land Subsidence Monitoring*, BCRS.

van Lammeren, A., Russchenberg, H., Apituley, A. and Feijt, A. (1997), CLARA: a data set to study sensor synergy, in: *Proc. of the workshop on Synergy of Active Instruments of the Earth Radiation Mission, November 12-14, GKSS Research Center, Geesthacht, Germany.*

Li, F. K. and Goldstein, R. M. (1990), Studies of Multibaseline Spaceborne Interferometric Synthetic Aperture Radars, *IEEE Trans. on Geoscience and Remote Sensing*, **28**(1):88–97.

Mason, B. J. (1971), *The Physics of Clouds*, University Press, Oxford, 2nd edn.

Massonnet, D., Briole, P. and Arnaud, A. (1995), Deflation of Mount Etna monitored by spaceborne radar interferometry, *Nature*, **375**:567–570.

Massonnet, D. and Feigl, K. L. (1995), Discrimination of geophysical phenomena in satellite radar interferograms, *Geophysical Research Letters*, **22**(12):1537–1540.

Massonnet, D., Rossi, M., Carmona, C., Adagna, F., Peltzer, G., Feigl, K. and Rabaute, T. (1993), The displacement field of the Landers earthquake mapped by radar interferometry, *Nature*, **364**(8):138–142.

McIlveen, R. (1995), *Fundamentals of Weather and Climate*, Chapman and Hall, London, 2nd edn.

Nathanson, F. E. (1969), *Radar design principles*, McGraw-Hill.

Niell, A. E. (1996), Global mapping functions for the atmosphere delay at radio wavelengths, *Journal of Geophysical Research*, **101**(B2):3227–3246.

Parsons, D. B. (1992), An Explanation for Intense Frontal Updrafts and Narrow Cold-Frontal Rainbands, *Journal of the Atmospheric Sciences*, **49**(19):1810–1825.

Reber, E. E. and Swope, J. R. (1972), On the correlation of the total precipitable water in a vertical column and the absolute humidity at the surface, *Journal of Applied Meteorology*, **11**:1322–1325.

Rogers, D. V. and Olsen, R. L. (1975), Delay and its relation to attenuation in microwave propagation through rain, in: *USNC/URSI Annual Meeting, Boulder CO, 20–23 Oct 1975.*

Ruf, C. S. and Beus, S. E. (1997), Retrieval of Tropospheric Water Vapor Scale Height from Horizontal Turbulence Structure, *IEEE Trans. on Geoscience and Remote Sensing*, **35**(2):203–211.

Saastamoinen, J. (1972), Introduction to Practical Computation of Astronomical Refraction, *Bulletin Geodesique*, **106**:383–397.

Schättler, B. (1997), Personal communication,.

Schwäbisch, M. (1995), Die SAR-Interferometrie zur Erzeugung digitaler Geländemodelle, Forschungsbericht 95-25, Deutsche Forschungsanstalt für Luft- un Raumfahrt, Oberpfaffenhofen.

Schwäbisch, M. and Geudtner, D. (1995), Improvement of Phase and Coherence Map Quality Using Azimuth Prefiltering: Examples from ERS-1 and X-SAR, in: *International Geoscience and Remote Sensing Symposium, Florence, Italy, 10–14 July 1995*, pp. 205–207.

Smith, Jr., E. K. and Weintraub, S. (1953), The Constants in the Equation for Atmospheric Refractive Index at Radio Frequencies, *Proceedings of the I.R.E*, **41**:1035–1037.

Solheim, F. S., Vivekanandan, J., Ware, R. H. and Rocken, C. (1997), Propagation Delays Induced in GPS Signals by Dry Air, Water Vapor, Hydrometeors and Other Particulates, *draft for J. of Geoph. Res.*

Spoelstra, T. A. T. (1997), Personal communication.

Stolk, R., Hanssen, R., van der Marel, H. and Ambrosius, B. (1997), Troposferische signaalvertraging; een vergelijking tussen GPS en SAR interferometrie, *GPS Nieuwsbrief*, **2**:3–7.

Stull, R. B. (1988), *An Introduction to Boundary Layer Meteorology*, Kluwer, Dordrecht.

Stull, R. B. (1995), *Meteorology Today For Scientists and Engineers*, West Publishing, St. Paul, Minneapolis.

Tarayre, H. (1996), *Extraction de Modeles Numeriques de Terrain par Interferometrie Radar Satellitaire: Algorithmie et Artefacts Atmospheriques*, Ph.D. thesis, Institut National Polytechnique de Toulouse, Toulouse.

Tarayre, H. and Massonnet, D. (1996), Atmospheric propagation heterogeneities revealed by ERS-1 interferometry, *Geophysical Research Letters*, **23**(9):989–992.

Tatarski, V. I. (1961), *Wave propagation in a turbulent medium*, McGraw-Hill, New York.

Tatarskii, V. I. (1971), *The Effects of the Turbulent Atmosphere on Wave Propagation*, Israel Program for Scientific Translations, Jerusalem, translated from Russian.

Topografische Dienst Nederland and Meetkundige Dienst Rijkswaterstaat (1997), TopHoogteMD Digital Elevation Model.

Treuhaft, R. N. and Lanyi, G. E. (1987), The effect of the dynamic wet troposphere on radio interferometric measurements, *Radio Science*, **22**(2):251–265.

Wessels, H. R. A. (1997), Personal communication,.

Zebker, H. A., Rosen, P. A. and Hensley, S. (1997), Atmospheric effects in interferometric synthetic aperture radar surface deformation and topographic maps, *Journal of Geophysical Research*, **102**(B4):7547–7563.

Zebker, H. A., Werner, C. L., Rosen, P. A. and Hensley, S. (1994), Accuracy of Topographic Maps Derived from ERS-1 Interferometric Data, *IEEE Trans. on Geoscience and Remote Sensing*, **32**(4):823–836.

Publications of the Delft Institute for Earth-Oriented Space Research:

97.1	Bouman, J.	A survey of global gravity models.
97.2	Bruijne, A. de	Wavelet and Radon analysis for detection of elongated structures in profile measurements.
97.3	Onselen, K. van	Quality investigation of vertical datum connection.

Request additional copies: Ms. W.G. Coops-Luijten, Delft University of Technology, Faculty of Civil Engineering and Geosciences, Thijsseweg 11, 2629 JA, Delft, The Netherlands, e-mail: deos@geo.tudelft.nl, costs: NLG 15,– (excl. postal charges).

ISBN 90-407-1774-5

Delft University Press